Study of conformational analysis, internal dynamics and non-covalent interactions of chalcogen-bridged compounds (*oxygen vs sulfur*) by rotational spectroscopy and computational chemistry

by

Tamanna Poonia

A thesis submitted to the Faculty of Graduate Studies of the University of Manitoba in partial fulfillment of the requirements of the degree of

Doctor of Philosophy

Department of Chemistry

University of Manitoba

Winnipeg, Canada

Abstract

Conformational analysis is a fundamental tool for assessing the three-dimensional spatial arrangements, energies, and stability of conformers influenced by intermolecular and intramolecular interactions. Rotational spectroscopy plays a crucial role in determining spectroscopic parameters by identifying their spectral fingerprints, while high-level quantum chemical calculations aid in the assignment of spectra and provide insights into conformational preferences and internal dynamics. In this thesis, we investigated the effect of different organic fragments on the conformational landscape of chalcogen-bridged compounds (oxygen *vs* sulfur). As previous microwave spectroscopic studies predominantly centered around small molecules containing O and S, our objective is to bridge this research void by analyzing relatively large and flexible molecules. We observed drastic differences in the conformational equilibria when transitioning from O to S bridged compounds, involving diallyl ether, diallyl sulfide, allyl ethyl ether, allyl ethyl sulfide, ethyl vinyl ether, ethyl vinyl sulfide, propyl vinyl ether, propyl vinyl sulfide, butyl vinyl ether, butyl vinyl sulfide. Additionally, we explored the effects of microsolvation through diallyl ether-water and diallyl sulfide-water complexes. A general trend emerged, indicating that the O-bridged compounds exhibit a competitive and rich conformational landscape in the presence of partially unsaturated side chains. However, the inclusion of saturated side chains with an increase in their length led to conformers being more close in terms of relative energies and to a greater number of conformers in S-bridged compounds compared to oxygen ones. Non-covalent interaction, natural bond orbital, quantum theory of atoms in molecules, and symmetry-adapted perturbation theory calculations, revealed the pivotal role of interactions involving the lone pairs of the central chalcogen atom (oxygen or sulfur) and the organic fragment

in governing conformational preference and energy ordering. We also observed complex splitting patterns attributed to methyl internal rotations in molecules featuring a methyl group. The results presented here lay a solid foundation for future studies aimed at advancing the development and modeling of chemical bonds, dynamics, and reactivity of organochalogens and main group compounds.

Acknowledgment

I would like to express my gratitude to the people and institutions that have significantly contributed to the successful completion of this thesis.

I want to thank my Ph.D. supervisor, Dr. Jennifer van Wijngaarden, for her consistent supervision, invaluable perspectives, and support throughout the course of my research. Her extensive knowledge, tremendous enthusiasm, and valuable feedback helped me in finishing my thesis.

My advisory committee members Dr. Mario Bieringer, Dr. Georg Schreckenbach and Dr. Derek Oliver, for their great support and assistance.

A special acknowledgment goes to my former labmate and dear friend, Dr. Weslley Guilherme Dias de Paiva Silva, for his constant support, advice, assistance, and collaboration during my Ph.D. program.

Members of the van Wijngaarden group, both present and past, including Dr. Weslley Guilherme Dias de Paiva Silva, Carolyn Gregory, Joseph Stitsky, and Rebecca Huard.

My friends and family for always being there for me and cheering me on during this journey. Without them, this would not have been possible.

Finally, I am grateful to the Department of Chemistry, Faculty of Graduate Studies, the GETS program, and the University of Manitoba Graduate Fellowship, for their financial assistance.

Dedication

To my parents, brother and my beloved cat, Usha Devi, RamMehar Poonia, Gourav and Leo.

Table of Content

List of Figures

List of Tables

List of Abbreviations

AEE	Allyl Ethyl Ether
AES	Allyl Ethyl Sulfide
AIMALL	Atoms In Molecules All Program
AMA	N-Allylmethylamine
AMA-w	N-Allylmethylamine-water
aug-cc-PVTZ	Augmented Correlation-Consistent Polarized Valence Triple Zeta Basis Set
AWG	Arbitrary Waveform Generator
B3LYP	Becke, 3-Parameter, Lee–Yang–Parr
BCP	Bond Critical Point
BF-FYMW	Balle-Flygare Fourier Transform Microwave
BP	Bond Path
BSSE	Basis Set Superposition Error
BVE	Butyl Vinyl Ether
BVS	Butyl Vinyl Sulfide
CAM	Combined Axis Method
CP-FTMW	Chirped-Pulse Fourier Transform Microwave
CREST	Conformer-Rotamer Ensemble Sampling Tool
D3BJ	Dispersion Correction with Becke-Johnson Damping
DAA	Diallyl Amine
DADS	Diallyl Disulfide
DAE	Diallyl Ether
DAS	Diallyl Sulfide
DAE-w	Diallyl Ether-water
DAS-w	Diallyl Sulfide-water
DFT	Density Functional Theory
ESI	Electronic Supplementary Information
EVAL	Evaluation of internal coordinates from Cartesians program

EVE	Ethyl Vinyl Ether
EVS	Ethyl Vinyl Sulfide
FF	Force Field
FFT	Fast Fourier Transformation
FID	Free Induction Decay
FTIR	Fourier Transform Infrared
FTMW	Fourier Transform Microwave
FWHM	Full Width at Half Maximum
GFN2-xTB	Geometry, Frequency, Non-covalent, 2, Extended Tight Binding
HB	Hydrogen Bond
iMTD-GC	Iterative Metadynamic Sampling and Genetic Crossover
KRA	Kraitchman Program
LAM	Large Amplitude Motion
LP	Lone Pair
MVE	Methyl Vinyl Ether
MVS	Methyl Vinyl Sulfide
NBO	Natural Bond Orbital
NCI	Non-Covalent Interaction
NCIPLOT	Non-Covalent Interaction Plotting Program
NMR	Nuclear Magnetic Resonance
PES	Potential Energy Surface
PGOPHER	Program for Rotational, Vibrational and Electronic Spectra
PMIFST	Principal Moments of Inertia From Structure
PVE	Propyl Vinyl ether
PVS	Propyl Vinyl Sulfide
QTAIM	Quantum Theory of Atoms in Molecules
RDG	Reduced Density Gradient
SAPT	Symmetry-Adapted Perturbation Theory
SI	Supporting Information
SNR	Signal-to-Noise Ratio
SPDT	Single Pole Double Throw

TA	Thenyl Alcohol
TM	Thenyl Mercaptan
TS	Transition State
UV-vis	Ultraviolet-Visible
XIAM	Holger Hartwig's Internal Axis Method Program
xTB	Extended Tight Binding
ZPE	Zero-Point Energy

Contribution of Authors

Chapter 4. Dramatic differences in the conformational equilibria of chalcogen-bridged compounds: The case of diallyl ether versus diallyl sulfide

1) Tamanna Poonia: Conceptualization, collection, and assignment of experimental spectrum, performed theoretical calculations, writing-original draft, review and editing.
2) Weslley G.D.P. Silvia: Analyzing theoretical calculations, writing-original draft, review and editing.
3) Jennifer van Wijngaarden: Funding acquisition, resources, supervision, writing - review and editing.

Chapter 5. Exploring the distinct conformational equilibria of allyl ethyl ether and allyl ethyl sulfide using rotational spectroscopy and computational chemistry

1) Tamanna Poonia: Conceptualization, collection, and assignment of experimental spectrum, performed theoretical calculations, writing-original draft, review and editing.
2) Jennifer van Wijngaarden: Funding acquisition, resources, supervision, writing - review and editing.

Chapter 7. Exploring the conformational landscape, hydrogen bonding and internal dynamics in the diallyl ether and diallyl sulfide monohydrates

1) Tamanna Poonia: Conceptualization, collection, and assignment of experimental spectrum, performed theoretical calculations, writing-original draft, review and editing.
1) Weslley G.D.P. Silvia: Conceptualization, collection, and assignment of experimental spectrum, performed theoretical calculations, writing-original draft, review and editing.
2) Jennifer van Wijngaarden: Funding acquisition, resources, supervision, writing - review and editing.

Chapter 1. Introduction

1.1 Overview of Conformational Analysis

Molecules can adopt different shapes and functions in response to their chemical environment. These spatial variations arise from rotations around their single bonds, leading to conformational isomers or conformers. These conformers represent the energetically preferred geometries due to stabilizing interactions present between different molecular components or with the surrounding solvent molecules. These interactions can be classified as intramolecular (within the molecule) or intermolecular (between different binding partners). Conformational analysis is the study of conformers in a molecular system, analyzing their energies, and investigating factors influencing their stabilities.[1–5]

In the mid-20th century, the concept of a molecular conformation was introduced by Barton[6] to describe hindered rotation about a single bond, which leads to distinguishable stereoisomers. Later, Kuhn[7] coined the term atropisomerism from a Greek word meaning 'does not turn', to refer to such stereoisomerism. This terminology has been periodically updated and refined over the decades. Fundamental studies by Kemp and Pitzer[8,9] highlighted the significance of restricted rotation in ethane and established the preference for the staggered conformation over eclipsed, while Hassel *et al.*[10–12] extended this to cyclic systems, and in doing so, solidified the importance of the chair conformation in cyclohexane. The impact of this work on the field of chemistry was solidified further when Barton[6] and Hassel[12] were awarded the Nobel Prize in chemistry in 1969 for their groundbreaking work on molecular conformation. These discoveries emphasized the connections between the molecular geometries, spectroscopic behavior and reactivity, and consequently, understanding the underlying reasons for preferred molecular

structures became essential across various scientific disciplines such as material design, spectroscopy, synthesis of organic molecules and biochemistry.[5,13–16]

Usually, the detection of all possible geometries of organic molecules depends on the timescale of the conformational interconversion (which is sensitively governed by an energy barrier) and requires a technique with sufficient temporal resolution. Therefore, a variety of spectroscopic methods have been employed for conformational analysis. These techniques encompass ultraviolet-visible (UV-vis), infrared, rotational, Raman, and nuclear magnetic resonance (NMR) spectroscopy and have provided insightful information about molecular conformations in many cases.[5,17] However, microwave (or rotational) spectroscopy has emerged as a powerful tool for accurately determining molecular geometries in the gas phase. The collision-free environment used in most modern instruments eliminates the influence of other molecules, solvent, and crystal packing effects. Also, high-resolution microwave spectroscopy can reveal unique geometries due to the separation of individual lines, linked to each conformer's unique geometry, analogous to different fingerprints in humans. By utilizing the concept of rotational moments of inertia, this spectroscopic technique establishes a direct connection between rotational frequency measurements and the molecular structure. Analyzing the patterns of rotational transitions based on their corresponding intensities and frequencies allows for the identification and differentiation of different conformers of a molecule.[18–21] For instance, the conformational analysis of the citronellal[22] monomer revealed the existence of 15 distinct conformations, representing one of the highest number of conformers detected for a species using microwave spectroscopy. Furthermore, this technique is used to study a wide range of molecular systems, including biomolecules like tryptamine[23] and tryptophol,[24] monomers such as 1,3,5-trisilapentane[25] and diallyl amine,[26] molecular complexes such as tetrahydro-2-furoic

acid···propylene oxide[27] and 2-chloro-1,1-difluoroethylene–acetylene,[28] and monohydrated complexes of furfuryl mercaptan and furfuryl alcohol,[29] among others.

Conformational analysis can indeed be explored using experimental methods, however, it is high-level quantum chemical calculations that truly enable the rapid identification of possible stable conformers and understanding of the conformational preferences of increasingly complex molecules. One illustrative example is the study of n-allylmethylamine (AMA),[30] where a potential energy scan (shown in Figure 1.1) obtained at B3LYP-D3(BJ)/cc-pVTZ level of theory, shows nine distinct energy minima, highlighting the rich conformational landscape obtained by considering the internal rotations around the δ and θ dihedral angles of the organic backbone. These calculations play a vital role in understanding the intricate aspects of predicting and assigning experimental rotational spectra based on the number of minima, each representing a conformer geometry, and the barriers between them, which governs whether interconversion is possible under the experimental conditions. They also offer valuable insights into the underlying reasons for a particular molecular geometry and the dynamic properties of molecules by allowing for the identification of non-covalent interactions and their impact.[4,5,31] Therefore, the combination of experimental investigations and computational calculations is crucial for the success of modern conformational analysis studies. While experimental methods offer direct observations and measurements, quantum chemical calculations provide a theoretical framework to interpret and explain the observed conformational behavior. By integrating these approaches, one can gain a comprehensive understanding of the conformational landscape and its implications.

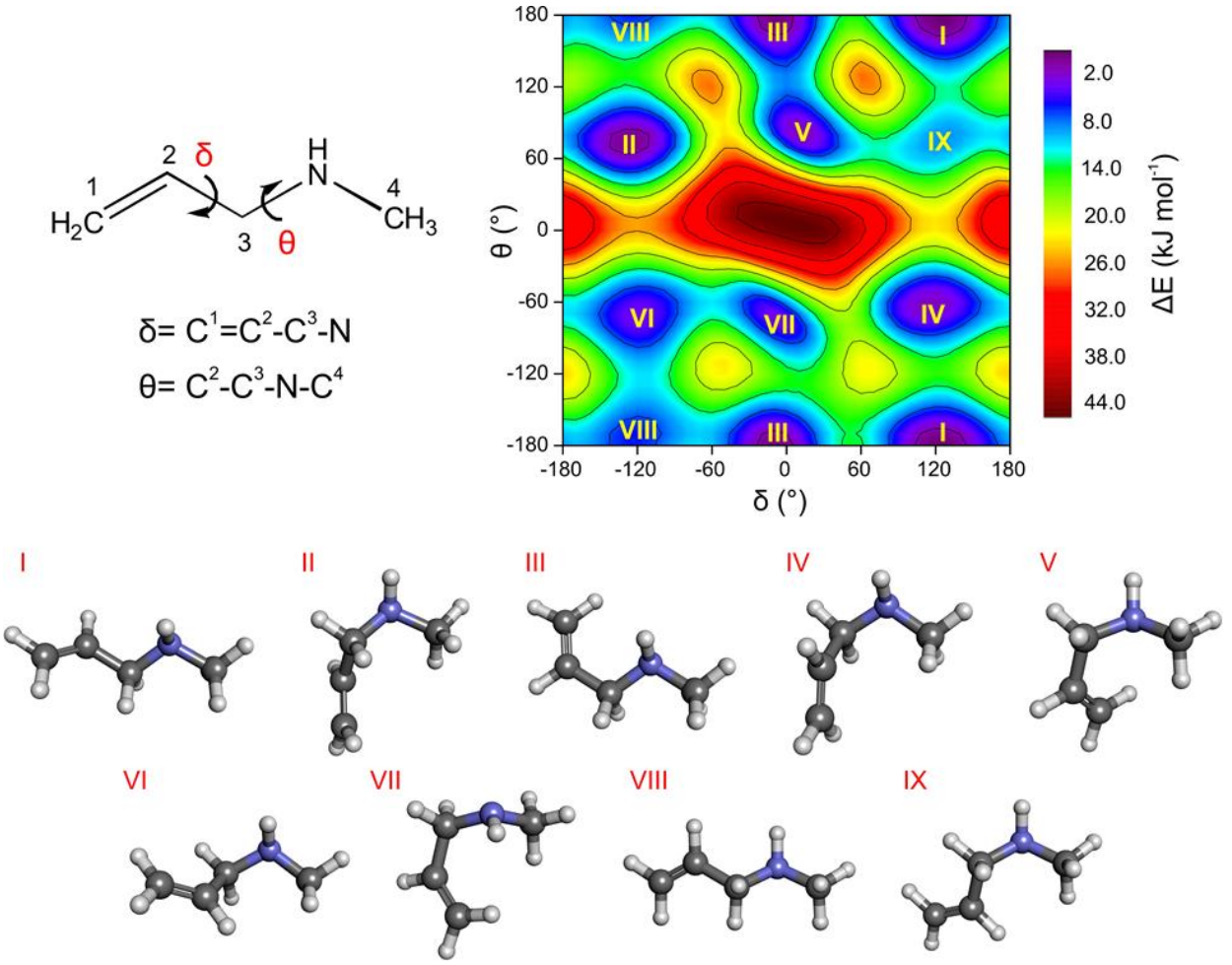

Figure 1.1 Potential energy surface (B3LYP-D3(BJ)/cc-pVTZ) and nine optimized conformers of AMA (B2PLYP-D3(BJ)/aug-cc-pVTZ) which arise through rotations around its δ and θ dihedral angles. Roman numerals from I–IX indicate conformer stability ordering with I being the most stable conformer.[30](Permission obtained from *ChemPhysChem* Journal)

To delve deeper, the upcoming sections will provide a brief overview of specific aspects of conformations in organic compounds, especially focusing on characteristics of large amplitude motions and non-covalent interactions, that influence their rotational spectra. This comprehensive exploration aims to add relevant background information for subsequent chapters of this thesis.

1.2 Large Amplitude Motion (LAM)

Before the groundbreaking research of Kemp and Pitzer in 1936,[8] it was widely accepted that "internal" rotation, which refers to the rotation of one group relative to another within a molecule connected by a single bond, occurred without any restrictions (i.e. unhindered). However, their pioneering analysis of ethane using thermodynamic data, revealed that the rotation of a methyl group with respect to the other methyl group is restricted by a potential energy barrier of approximately 1000 cm^{-1}. Over the past six decades, rotational spectroscopy has emerged as a valuable tool for investigating hindered large-amplitude internal rotations, particularly methyl internal rotations (or methyl torsion).[19,32] This is because the effect of methyl internal rotation becomes apparent in the rotational spectrum of molecules containing a methyl group, as it causes the rotational energy levels to split into two sublevels, namely nondegenerate A and degenerate E torsional levels. This separation leads to a splitting in the rotational transitions (given sufficient instrument resolution), referred to as the A/E splitting, which is dependent on the potential barrier height associated with methyl torsion.

During the early stages of applying quantum theory, researchers recognized the fundamental quantum mechanical nature of hindered rotations in molecules.[33] Since then, significant efforts have been devoted to investigating the origin of the potential barrier associated with methyl group rotation.[34–38] With rapid advancements in high-level quantum chemical calculations, that routinely enable accurate predictions of both molecular geometry as well as the torsional potential, it is well-established that the height and shape of this barrier depend on the conformation of the molecule and the associated intramolecular interactions. Fitting A/E splitting patterns obtained from a rotational spectrum[39] offers a precise method for experimentally determining the height of the potential barrier. Therefore, the combination of theoretical and

experimental studies has a significant influence on understanding the nature of the torsional barrier.[40–43]. By studying methyl torsion in various molecular systems, valuable insights can be gained into potential functions, barrier heights, and how these are influenced by the underlying forces that dictate conformational preferences.

To comprehend how different stabilizing and destabilizing effects influences the conformational preferences of molecules, the following section will explore non-covalent interactions. These include a wide range of attributes, each with its own unique strength and properties. Understanding the diverse nature of these connections is key to comprehending their influence on molecular geometries.

1.3 Non-covalent Interactions

These are crucial in chemistry and biology and are central to understanding both molecular level and bulk phase properties of matter. These interactions play essential roles in various aspects, including transmitting stereochemical information,[44] determining properties and structure of molecules,[45] shaping protein structures,[46] facilitating enzyme-ligand binding and enabling nucleic acid base-pairing[47] to name just a few examples. These interactions are classified based on their strength, origin, and characteristics. Among them, hydrogen bonding emerges as a highly versatile and extensively researched interaction.[48–53] Furthermore, interactions involving π-systems, including π-hydrogen bonding, π-stacking, and cation-π interactions, have also received significant attention.[54–58] In recent times, the scientific community has confirmed the existence of two additional non-covalent interactions involving π-electrons, namely anion-π and n-π* (or lone pair-π*) interactions.[53,56,59–65] Within these diverse classes of interactions, a wide array of contacts exist, characterized by unique structural and energetic parameters. For example, halogen bonding

combines charge transfer and electrostatic attraction, with the extent varying depending on the participating atoms and groups.[66,67] Similar analyses have been conducted for chalcogen bonds,[68,69] pnictogen bonds,[70–72] tetrel and triel bonds.[72,73] An overview of some interactions found to be important in the species explored in this thesis is given below.

Hydrogen bonds (HBs) involve interactions between a hydrogen atom and usually an electronegative atom (HB donor and HB acceptor). Basically, the HB interaction can be represented as X–H...Y where X is the HB donor and Y is the HB acceptor. This type of interaction is characterized by a donor-acceptor orbital interaction, where the lone pair of electrons on atom Y donates to the antibonding σ* orbital of the X–H bond. The strength of a hydrogen bond, which can play a critical role in establishing the lowest energy conformers of a compound, is influenced by various factors, including the intrinsic properties of the donor and acceptor orbitals. While electronegativity does play a role in determining HB strength, it is not the sole determining factor. It is important to note that HBs can involve atoms with less electronegativity as long as attractive interactions can be established between the positive partially-charged hydrogen atom (δ+) and the negative partially-charged acceptor atom (δ-). This expanded understanding allows for the inclusion of non-classical HBs involving atoms that are traditionally considered less electronegative, such as chalcogens like S and Se, as HB donors or acceptors.[74–76]

Charge transfer interaction refers to the more general case of transfer of electron density from an electron donor to an electron acceptor in atoms or molecules. This process is accompanied by resonance, where the electrons are delocalized between donor (D) and acceptor (A) orbitals, facilitating the transfer of charge from D to A. The D species is typically characterized by an excess of electron density as found in a molecule possessing a lone pair of electrons or a π-electron system. On the other hand, the A species has a deficit of electron density, often associated with electron-

deficient regions.[77–79] This type of interaction has been observed to be important in defining the conformational landscape in various systems, including molecule like diallyl amine,[26] where the lone pair electron density on nitrogen interacts with the antibonding orbitals of the C–H, C–C, and C=C bonds in the allyl side chain, leading to the stabilization of conformers. Charge transfer interactions are also found to be crucial in stabilizing conformers of the formaldehyde adduct,[80] in nopinone,[81] in cyclohexanol···SO_2 cluster[82] and many more. Therefore, these interactions play a significant role in determining the stability and conformational properties of molecules.

1.4 Interest in the role of heteroatoms in conformational analysis

An intriguing aspect of understanding the importance of these interactions lies in studying the R-X-R type of alkane substitution, where the nature of the bridging X heteroatom influences the distinct conformational preferences of the R-groups and overall molecules through unique non-covalent interactions. Microwave studies of compounds like allylmethylamine (AMA)[30] and diallyl amine (DAA),[26] have previously demonstrated interesting behavior with different R groups. In the present thesis, the substitution of X with a chalcogen atom (oxygen *vs* sulfur) is also considered, where the replacement of a lighter chalcogen atom (O) with a heavier one (S) significantly affects the electronic structure due to differences in electronegativity, polarizability and atomic size, further adding complexity to the conformational studies.[83–88] These systems also offer a prospective case study to understand the role of different R-groups in shaping the molecular conformational landscapes and to explore the interactions (especially those involving the central atom) responsible for the conformer stabilities. Additionally, detailed explorations of the underlying potential energy profiles of such species can reveal the influence of conformer geometry on methyl internal rotation barriers which can be studied through splitting patterns,

similar to observations in the literature for R-X-R type molecules like allyl methyl ether and allyl methyl sulfide.[89,90]

Although most previous microwave spectroscopic research on O *vs* S-containing species has concentrated on small, flexible molecules,[89–92] there is significant interest in studying relatively large flexible molecules as detailed explorations of their conformational landscapes can reveal valuable insights into their dynamics and stability. By conducting a suite of comprehensive investigations, we can uncover the complexities and general trends of organochalcogens and enhance our understanding of their properties and behavior at the molecular level.

1.5 Outline

This thesis examines the conformational landscape of chalcogen-bridged monomers and molecular complexes by employing a combination of rotational spectroscopy and quantum chemical calculations. The primary goal is to determine the most stable geometries of these systems and gain insights into the underlying non-covalent interactions that influence their conformational preferences at the molecular level. The study specifically focuses on examining the trend (similarities and differences) in such preferences when moving from oxygen to sulfur as the chalcogen-bridged atom. Furthermore, it explores the impact of using different organic fragments in the chalcogen-bridged compounds and investigates the effect of solvation in the monomer-water complexes. Thus, through these investigations, a deeper understanding of the conformational equilibria, molecular geometries, and internal dynamics can be achieved.

Chapter 2 provides an overview of the theoretical principles of rotational spectroscopy and methyl internal rotation. In Chapter 3, the description of two custom-built microwave spectrometers and computational methods are given, which are essential for collecting the

rotational spectrum, and guiding the spectral assignments, investigating non-covalent interactions, and understanding the stability of observed conformers. Chapter 4 explores the conformational equilibria of diallyl ether (DAE) and diallyl sulfide (DAS). The study explores remarkable differences between these two compounds, with DAE exhibiting a highly competitive landscape characterized by the observation of nine conformers experimentally in contrast to one conformer of DAS although the lowest energy arrangement of the allyl fragments is similar in both.

In chapter 5, the impact of different organic fragments is investigated by replacing one allyl fragment from the previous diallyl study with a saturated ethyl side chain, resulting in allyl ethyl sulfide (AES) and allyl ethyl ether (AEE). The introduction of an ethyl side chain introduces a methyl rotor with associated splitting and significantly alters the conformational equilibria of the two species in that similar numbers of conformers are predicted but the geometries of the lowest energy forms are surprisingly different for the S-bridged versus O-bridged compounds.

To expand these studies and better deduce the importance of interactions with saturated groups, Chapter 6 describes computational studies of ethyl vinyl ether (EVE), ethyl vinyl sulfide (EVS), propyl vinyl sulfide (PVS), propyl vinyl ether (PVE), butyl vinyl sulfide (BVS), and butyl vinyl ether (BVE), alongside experimental investigations of PVE and BVE compounds and their methyl internal rotation effects. Surprisingly, the sulfur compounds are predicted to exhibit richer conformational landscape than the ethers, which differs significantly from the studies of DAE, DAS, AEE, and AES.

Chapter 7 focuses on the study of the diallyl ether-water (DAE-w) and diallyl sulfide-water (DAS-w) complexes to evaluate the effect of solvation on these prototypical organochalcogen compounds. The aim is to understand how the presence of a water molecule affects the conformational landscape compared to that of the monomer study in Chapter 4. Chapter 8 provides

a concise summary of the key findings of the thesis and offers insights into potential avenues for further research.

1.6 References

1 E. L. Eliel, Conformational analysis in mobile systems, *J. Chem. Educ.*, 1960, **37**, 126.

2 D. H. Wertz and N. L. Allinger, Conformational analysis—CI, *Tetrahedron*, 1974, **30**, 1579–1586.

3 E. L. Eliel and S. H. Wilen, *Stereochemistry of Organic Compounds*, John Wiley & Sons: New York; 1994.

4 J. Uthuppan and K. Soni, Conformational Analysis: a Review, *Int. J. Pharm. Sci.*, 2013, **4**, 34–41.

5 C. F. Tormena, Conformational analysis of small molecules: NMR and quantum mechanics calculations, *Prog. Nucl. Magn. Reson. Spectrosc.*, 2016, **96**, 73–88.

6 B. DHR, *Principles of Conformational Analysis. Nobel Lectures, Chemistry 1963–1970*, Amsterdam: Elsevier Publishing Company; 1972.

7 K. R, *Molekulare asymmetrie. In: Freuberg H, ed. Stereochemie*, Leipzig-Wien: FranzDeutike; 1933, 803–824.

8 J. D. Kemp and K. S. Pitzer, Hindered Rotation of the Methyl Groups in Ethane, *J. Chem. Phys.*, 1936, **4**, 749.

9 J. D. Kemp and K. S. Pitzer, The entropy of ethane and the third law of thermodynamics. Hindered rotation of methyl groups, *J Am Chem Soc*, 1937, **59**, 276–279.

10 O. Hassel, H. Viervoll, L. G. Sillén, A. Linnasalmi and P. Laukkanen, *Acta Chem. Scand.*,

1947, 1, 149–168.

11 O. Hassel, B. Ottar, B. Roald, A. Linnasalmi and P. Laukkanen, *Acta Chem. Scand.*, 1947, 1, 929–943.

12 O. Hassel, *Structural Aspects of Interatomic Charge- Transfer Bonding. Nobel Lectures, Chemistry 1963– 1970*, Amsterdam: Elsevier Publishing Company; 1972.

13 E. R. Johnson, S. Keinan, P. Mori-Sánchez, J. Contreras-García, A. J. Cohen and W. Yang, Revealing noncovalent interactions, *J. Am. Chem. Soc.*, 2010, **132**, 6498–6506.

14 M. Juanes, R. T. Saragi, W. Caminati and A. Lesarri, The Hydrogen Bond and Beyond: Perspectives for Rotational Investigations of Non-Covalent Interactions, *Chem. - A Eur. J.*, 2019, **25**, 11402–11411.

15 J. Stitsky, W. G. D. P. Silva, W. Sun and J. Van Wijngaarden, Conformers of Allyl Isothiocyanate: A Combined Microwave Spectroscopy and Computational Study, *J. Phys. Chem. A*, 2020, **124**, 3876–3885.

16 G. Bifulco, P. Dambruoso, L. Gomez-Paloma and R. Riccio, Determination of relative configuration in organic compounds by NMR spectroscopy and computational methods, *Chem. Rev.*, 2007, **107**, 3744–3779.

17 A. Mazzanti and D. Casarini, Recent trends in conformational analysis, *Wiley Interdiscip. Rev. Comput. Mol. Sci.*, 2012, **2**, 613–641.

18 C. H. Townes and A. L. Schawlow, *Microwave Spectroscopy*, Dover: New York; 1975.

19 W. Gordy and R. L. Cook, *Microwave Molecular Spectra*, John Wiley & Sons: New York; 1984.

20 F. Xie, S. Mahendiran, N. A. Seifert and Y. Xu, Modifying conformational distribution of chiral tetrahydro-2-furoic acid through its interaction with water: a rotational spectroscopic

and theoretical investigation, *Phys. Chem. Chem. Phys.*, 2021, **23**, 3820–3825.

21 S. I. Murugachandran, J. Tang, I. Peña, D. Loru and M. E. Sanz, New Insights into Secondary Organic Aerosol Formation: Water Binding to Limonene, *J. Phys. Chem. Lett.*, 2021, **12**, 1081–1086.

22 S. R. Domingos, C. Pérez, C. Medcraft, P. Pinacho and M. Schnell, Flexibility unleashed in acyclic monoterpenes: Conformational space of citronellal revealed by broadband rotational spectroscopy, *Phys. Chem. Chem. Phys.*, 2016, **18**, 16682–16689.

23 J. L. Alonso, V. Cortijo, S. Mata, C. Pérez, C. Cabezas, J. C. López and W. Caminati, Nuclear quadrupole coupling interactions in the rotational spectrum of tryptamine, *J. Mol. Spectrosc.*, 2011, **269**, 41–48.

24 R. Sanchez, W. Caminati, J. C. López and J. L. Alonso, The rotational spectra of conformers of biomolecules: Tryptophol, *Chem. Phys. Lett.*, 2005, **414**, 226–229.

25 A. Jabri, F. E. Marshall, W. R. N. Tonks, R. E. Brenner, D. J. Gillcrist, C. J. Wurrey, I. Kleiner, G. A. Guirgis and G. S. Grubbs, The Conformational Landscape, Internal Rotation, and Structure of 1,3,5-Trisilapentane using Broadband Rotational Spectroscopy and Quantum Chemical Calculations, *J. Phys. Chem. A*, 2020, **124**, 3825–3835.

26 W. G. D. P. Silva, G. Daudet, S. Perez, S. Thorwirth and J. van Wijngaarden, Conformational preferences of diallylamine: A rotational spectroscopic and theoretical study, *J. Chem. Phys.*, 2021, **154**, 1–25.

27 F. Xie, N. A. Seifert, A. S. Hazrah, W. Jäger and Y. Xu, Conformational landscape, chirality recognition and chiral analyses: rotational spectroscopy of tetrahydro-2-furoic acid···propylene oxide conformers, *ChemPhysChem*, 2021, **22**, 455–460.

28 H. O. Leung and M. D. Marshall, The Importance of How the Pieces Fit Together: The

Microwave Spectrum and Molecular Structure of 2-Chloro-1,1-Difluoroethylene-Acetylene, *J. Phys. Chem. A*, 2020, **124**, 1382–1389.

29 M. Juanes, A. Lesarri, R. Pinacho, E. Charro, J. E. Rubio, L. Enríquez and M. Jaraíz, Sulfur Hydrogen Bonding in Isolated Monohydrates: Furfuryl Mercaptan versus Furfuryl Alcohol, *Chem. - A Eur. J.*, 2018, **24**, 6564–6571.

30 W. G. D. P. Silva, T. Poonia and J. van Wijngaarden, Targeting the Rich Conformational Landscape of N-Allylmethylamine Using Rotational Spectroscopy and Quantum Mechanical Calculations, *ChemPhysChem*, 2020, **21**, 2515–2522.

31 I. V. Alabugin, K. M. Gilmore and P. W. Peterson, Hyperconjugation, *Wiley Interdiscip. Rev. Comput. Mol. Sci.*, 2011, **1**, 109–141.

32 C. C. Lin and J. D. Swalen, Internal rotation and microwave spectroscopy, *Rev. Mod. Phys.*, 1959, **31**, 841–891.

33 H. H. Nielsen, The torsion oscillator-rotator in the quantum mechanics, *Phys. Rev.*, 1932, **40**, 445–456.

34 L. Goodman and V. Pophristic, Where does the dimethyl ether internal rotation barrier come from?, *Chem. Phys. Lett.*, 1996, **259**, 287–295.

35 R. K. Sinha, B. P. Singh and T. Kundu, Origin of threefold methyl torsional potential in methylindoles, *Theor. Chem. Acc.*, 2008, **121**, 59–70.

36 T. Kundu, B. Pradhan and B. P. Singh, Origin of methyl torsional potential barrier - An overview, *Proc. Indian Acad. Sci. Chem. Sci.*, 2002, **114**, 623–638.

37 S. Liu, N. Govind and L. G. Pedersen, Exploring the origin of the internal rotational barrier for molecules with one rotatable dihedral angle, *J. Chem. Phys.*, 2008, **129**, 094104.

38 R. F. W. Bader, J. R. Cheeseman, K. E. Laidig, K. B. Wiberg and C. Breneman, Origin of

Rotation and Inversion Barriers, *J. Am. Chem. Soc.*, 1990, **112**, 6530–6536.

39 W. Gordy, N. Carolina, R. L. Cook and J. Wiley, Microwave molecular spectra, *J. Mol. Struct.*, 1972, **11**, 332–333.

40 C. Dindić and H. V. L. Nguyen, Benchmarking acetylthiophene derivatives: methyl internal rotations in the microwave spectrum of 2-acetyl-5-methylthiophene, *Phys. Chem. Chem. Phys.*, 2022, **25**, 509–519.

41 L. Ferres, W. Stahl, I. Kleiner and H. V. L. Nguyen, The effect of internal rotation in p-methyl anisole studied by microwave spectroscopy, *J. Mol. Spectrosc.*, 2018, **343**, 44–49.

42 H. V. L. Nguyen, W. Caminati and J. U. Grabow, The LAM of the Rings: Large Amplitude Motions in Aromatic Molecules Studied by Microwave Spectroscopy, *Molecules*, 2022, **27**, 3948.

43 M. Andresen, I. Kleiner, M. Schwell, W. Stahl and H. V. L. Nguyen, Acetyl Methyl Torsion in Pentan-2-one As Observed by Microwave Spectroscopy, *J. Phys. Chem. A*, 2018, **122**, 7071–7078.

44 J. Clayden, Transmission of stereochemical information over nanometre distances in chemical reactions, *Chem. Soc. Rev.*, 2009, **38**, 817–829.

45 J. M. Lehn, Toward self-organization and complex matter, *Science (80-.).*, 2002, **295**, 2400–2403.

46 S. Deechongkit, H. Nguyen, E. T. Powers, P. E. Dawson, M. Gruebele and J. W. Kelly, Context-dependent contributions of backbone hydrogen bonding to β-sheet folding energetics, *Nature*, 2004, **430**, 101–105.

47 A. T. Krueger and E. T. Kool, Model systems for understanding DNA base pairing, *Curr. Opin. Chem. Biol.*, 2007, **11**, 588–594.

48 G. R. Desiraju and T. Steiner, *The Weak Hydrogen Bond in Structural Chemistry and Biology*, Oxford University Press: New York; 1999.

49 J.-M.Lehn, *Supramolecular Chemistry: Concepts and Perspectives*, JohnWiley & Sons: New York; 1996.

50 J. W. Steed and J. L. Atwood, *Supramolecular Chemistry: A Concise Introduction*, John Wiley & Sons Inc: New York; 2000.

51 G. A. Jeffrey and W. Saenger, *Hydrogen Bonding in Biological Structures*, Springer-Verlag: Berlin; 1991.

52 E. Arunan, G. R. Desiraju, R. A. Klein, J. Sadlej, S. Scheiner, I. Alkorta, D. C. Clary, R. H. Crabtree, J. J. Dannenber, P. Hobza, H. G. Kjaergaard, A. C. Legon, B. Mennucci and D. J. Nesbitt, Definition of the hydrogen bond (IUPAC Recommendations 2011), *Pure Appl. Chem.*, 2011, **83**, 1637–1641.

53 S. K. Singh and A. Das, The n → π∗ interaction: A rapidly emerging non-covalent interaction, *Phys. Chem. Chem. Phys.*, 2015, **17**, 9596–9612.

54 E. A. Meyer, R. K. Castellano and F. Diederich, *Interactions with aromatic rings in chemical and biological recognition*, 2003, vol. 42.

55 L. M. Salonen, M. Ellermann and F. Diederich, Aromatic rings in chemical and biological recognition: Energetics and structures, *Angew. Chemie - Int. Ed.*, 2011, **50**, 4808–4842.

56 L. Serrano, M. Bycroft and A. R. Fersht, Aromatic-aromatic interactions and protein stability. Investigation by double-mutant cycles, *J. Mol. Biol.*, 1991, **218**, 465–475.

57 G. R. Desiraju, Supramolecular Synthons in Crystal Engineering—A New Organic Synthesis, *Angew. Chemie Int. Ed. English*, 1995, **34**, 2311–2327.

58 E. M. Cabaleiro-Lago, J. Rodrgíuez-Otero and Á. Peña-Gallego, Effect of microhydration

on the guanidiniumbenzene interaction, *J. Chem. Phys.*, 2011, **135**, 214301.

59 J. C. Amicangelo, B. W. Gung, D. G. Irwin and N. C. Romano, Ab initio study of substituent effects in the interactions of dimethyl ether with aromatic rings, *Phys. Chem. Chem. Phys.*, 2008, **10**, 2695–2705.

60 A. Frontera, P. Gamez, M. Mascal, T. J. Mooibroek and J. Reedijk, Putting anion-π interactions into perspective, *Angew. Chemie - Int. Ed.*, 2011, **50**, 9564–9583.

61 Z. Lu, P. Gamez, I. Mutikainen, U. Turpeinen and J. Reedijk, Supramolecular Assemblies Generated from Both Lone-Pair---π and C-H---π Binding Interactions, *Cryst. Growth Des.*, 2007, **7**, 1669–1671.

62 H. T. Chifotides and K. R. Dunbar, Anion-π Interactions in Supramolecular Architectures, 2013, **46**, 894–906.

63 B. W. Gung, Y. Zou, Z. Xu, J. C. Amicangelo, D. G. Irwin, S. Ma and H. C. Zhou, Quantitative study of interactions between oxygen lone pair and aromatic rings: Substituent effect and the importance of closeness of contact, *J. Org. Chem.*, 2008, **73**, 689–693.

64 A. Choudhary, D. Gandla, G. R. Krow and R. T. Raines, Nature of amide carbonyl-carbonyl interactions in proteins, *J. Am. Chem. Soc.*, 2009, **131**, 7244–7246.

65 D. Quiêonero, C. Garau, C. Rotger, A. Frontera, P. Ballester, A. Costa and P. M. Dey, Anion-π Interactions : Do They Exist ?, *Angew. Chem.*, 2002, **114**, 3539–3542.

66 G. Cavallo, P. Metrangolo, R. Milani, T. Pilati, A. Priimagi, G. Resnati and G. Terraneo, The halogen bond, *Chem. Rev.*, 2016, **116**, 2478–2601.

67 L. P. Wolters, N. W. G. Smits and C. F. Guerra, Covalency in resonance-assisted halogen bonds demonstrated with cooperativity in N-halo-guanine quartets, *Phys. Chem. Chem. Phys.*, 2015, **17**, 1585–1592.

68 L. Vogel, P. Wonner and S. M. Huber, Chalcogen Bonding: An Overview, *Angew. Chemie - Int. Ed.*, 2019, **58**, 1880–1891.

69 M. Bortoli, S. M. Ahmad, T. A. Hamlin, F. M. Bickelhaupt and L. Orian, Nature and strength of chalcogen-π bonds, *Phys. Chem. Chem. Phys.*, 2018, **20**, 27592–27599.

70 S. Scheiner and J. Lu, Halogen, Chalcogen, and Pnicogen Bonding Involving Hypervalent Atoms, *Chem. - A Eur. J.*, 2018, **24**, 8167–8177.

71 S. Scheiner, The pnicogen bond: Its relation to hydrogen, halogen, and other noncovalent bonds, *Acc. Chem. Res.*, 2013, **46**, 280–288.

72 S. J. Grabowski, Pnicogen and tetrel bonds—tetrahedral Lewis acid centres, *Struct. Chem.*, 2019, **30**, 1141–1152.

73 A. Franconetti and A. Frontera, 'Like-like' tetrel bonding interactions between Sn centres: A combined: Ab initio and CSD study, *Dalt. Trans.*, 2019, **48**, 11208–11216.

74 S. Scheiner, *Noncovalent Forces*, 1st ed.; Scheiner, S., Ed.; Springer International Publishing: Switzerland, 2015.

75 W. G. D. P. Silva and J. Van Wijngaarden, Characterization of Large-Amplitude Motions and Hydrogen Bonding Interactions in the Thiophene-Water Complex by Rotational Spectroscopy, *J. Phys. Chem. A*, 2021, **125**, 3425–3431.

76 P. Zhou, F. Tian, F. Lv and Z. Shang, Geometric characteristics of hydrogen bonds involving sulfur atoms in proteins, *Proteins Struct. Funct. Bioinforma.*, 2009, **76**, 151–163.

77 B. C. J. Bender, Theoretical Models of Charge-transfer Complexes, *Chem. Soc. Rev.*, 1986, **15**, 475–502.

78 H. A. Bent, Structural chemistry of donor-acceptor interactions, *Chem. Rev.*, 1968, **68**, 587.

79 G. Briegleb, Electron Affinity of Organic Molecules, *Angew. Chemie Int. Ed. English*, 1964,

3, 617–632.

80 J. C. López, A. Macario, A. Maris, I. Alkorta and S. Blanco, How Aromatic Fluorination Exchanges the Interaction Role of Pyridine with Carbonyl Compounds: The Formaldehyde Adduct, *Chem. - A Eur. J.*, 2021, **27**, 13870–13878.

81 E. M. Neeman, J. R. Aviles Moreno and T. R. Huet, Gas-phase hydration of nopinone: The interplay between theoretical methods and experiments unveils the conformational landscape, *Phys. Chem. Chem. Phys.*, 2021, **23**, 18137–18144.

82 Y. Jin, R. T. Saragi, M. Juanes, G. Feng and A. Lesarri, Interaction topologies of the S⋯O chalcogen bond: The conformational equilibrium of the cyclohexanol⋯SO_2 cluster, *Phys. Chem. Chem. Phys.*, 2021, **23**, 10799–10806.

83 G. C. Hoover and D. S. Seferos, Photoactivity and optical applications of organic materials containing selenium and tellurium, *Chem. Sci.*, 2019, **10**, 9182–9188.

84 M. Jeffries-El, B. M. Kobilka and B. J. Hale, Optimizing the performance of conjugated polymers in organic photovoltaic cells by traversing group 16, *Macromolecules*, 2014, **47**, 7253–7271.

85 E. L. Kynaston, K. J. Winchell, P. Y. Yee, J. G. Manion, A. D. Hendsbee, Y. Li, S. Huettner, S. H. Tolbert and D. S. Seferos, Poly(3-alkylthiophene)- block-poly(3-alkylselenophene)s: Conjugated Diblock Co-polymers with Atypical Self-Assembly Behavior, *ACS Appl. Mater. Interfaces*, 2019, **11**, 7174–7183.

86 S. Ye, L. Janasz, W. Zajaczkowski, J. G. Manion, A. Mondal, T. Marszalek, D. Andrienko, K. Müllen, W. Pisula and D. S. Seferos, Self-Organization and Charge Transport Properties of Selenium and Tellurium Analogues of Polythiophene, *Macromol. Rapid Commun.*, 2019, **40**, 1–8.

87 B. E. Arango Hoyos and R. M. Romano, Experimental and theoretical conformational studies on diallyl sulfide, *J. Mol. Struct.*, 2019, **1182**, 54–62.

88 J. Demaison, N. Vogt, R. T. Saragi, M. Juanes, H. D. Rudolph and A. Lesarri, How flexible is the disulfide linker? A combined rotational-computational investigation of diallyl disulfide, *Phys. Chem. Chem. Phys.*, 2019, **21**, 19732–19736.

89 W. Caminati, A. C. Fantoni, C. Paolucci and B. Velino, Conformational equilibrium in methyl allyl ether, *J. Mol. Spectrosc.*, 1991, **145**, 362–370.

90 A. C. Fantoni, Microwave spectrum, confromation rotation in allyl methyl sulphide, *J. Mol. Struct.*, 1991, **243**, 131–139.

91 R. E. PENN and R. F. CURL, Microwave spectrum of methyl vinyl sulfide, *J. Mol. Spectrosc.*, 1967, **24**, 235–243.

92 P. Cahill, L. Peter Gold and N. L. Owen, Microwave spectrum, conformation, dipole moment, and barrier to internal rotation in methyl vinyl ether, *J. Chem. Phys.*, 1968, **48**, 1620–1626.

Chapter 2. Microwave Rotational Spectroscopy

2.1 Microwave Spectroscopy

Microwave spectroscopy (MW) is a powerful technique to measure the rotational transitions of gaseous molecules in the microwave region of the electromagnetic spectrum. Only molecules with a permanent electric dipole moment possess a microwave spectrum, which is comprised of a series of lines representing transition frequencies related to the energy difference between two rotational states. By thoroughly examining the rotational fingerprints, highly accurate rotational constants and centrifugal distortion constants can be determined, providing key insights into the molecular systems under investigation. Since rotational constants are inversely proportional to the molecular moments of inertia, MW spectroscopy is an effective method for determining molecular structures and distinguishing different conformers and isotopologues of a variety of chemical systems. As molecules are not rigid, centrifugal distortion constants which account for changing molecular shapes during rotation also provide information about the topology of the molecular potential energy surface. Occasionally, the observed rotational transitions may show characteristic splitting patterns caused by intrinsic molecular dynamics or interactions within the molecules. Examining these splitting patterns provides further information about energy barriers to internal motions and the local electronic environment within the studied molecules.

The molecules presented in this thesis were studied in the microwave frequency range of 4-26 GHz using two custom-built Fourier transform microwave (FTMW) spectrometers. The rest of this chapter provides a concise summary of the general theory of rotational spectroscopy,[1–3] including the principles of large amplitude motion (specifically, the case of methyl internal rotation),[4–10] which has been observed in some of the investigated molecules.

2.2 Linear Molecules

The rotational Hamiltonian operator can formulated by employing the classical mechanics rigid rotor approximation model as:

$$\hat{H} = \frac{\hat{J}_a^2}{2\mathrm{I_a}} + \frac{\hat{J}_b^2}{2\mathrm{I_b}} + \frac{\hat{J}_c^2}{2\mathrm{I_c}} \tag{2.1}$$

$$\hat{H} = \frac{\hat{J}^2}{2\mathrm{I}} \tag{2.2}$$

where, $\hat{\mathrm{J}}$ stands for the total rotational angular momentum, I represents the moment of inertia for rotation about the a, b, and c inertial axes which are mutually perpendicular. One can determine the moment of inertia associated with each axis of rotation I_a, I_b, and I_c as:

$$I = \sum_i m_i r_i^2 \tag{2.3}$$

where, m is the atomic mass and r is the distance of each atom to the i^{th} principal axis of rotation. For the simplest case of a linear top (I_a = 0 and I_b = I_c), applying the rotational Hamiltonian (equation 2.2) to the Schrödinger equation below (equation 2.4):

$$\hat{H}\Psi = E\Psi \tag{2.4}$$

the rotational energy levels for the linear top are obtained and can be represented by the term value F(J) as:

$$\mathrm{F\ (J)} = \frac{h}{8\pi^2 I_b}\mathrm{J(J+1)} = \mathrm{BJ\ (J+1)} \tag{2.5}$$

in which the rotational constant (B, in Hz) is given by $\frac{h}{8\pi^2 I_b}$ and J is the rotational quantum number which assumes integer values from 0, 1, 2, 3, 4... and so on. Usually, the units used for rotational constants (B) are:

$$\mathrm{B\ (MHz)} = \frac{\mathrm{h}}{8\pi^2 I_b} \times 10^{-6} \tag{2.6}$$

$$\mathrm{B}\ (cm^{-1}) = \frac{\mathrm{h}}{8\pi^2 I_b c} \times 10^{-2} \quad (2.7)$$

where h is the Planck's constant (6.626×10^{-34} J.s) and c is the speed of light (2.998×10^{10} cm s^{-1}). The line position in a rotational spectrum indicates the electromagnetic radiation frequency that corresponds to the energy difference between two rotational levels (lower state, J" or J, and upper state, J' or J+1) of a linear molecule that satisfy the selection rule $\Delta J = \pm 1$. Therefore, the rotational transition frequency (ν) can be estimated by the following equation:

$$\nu_{J\rightarrow J+1} = F\ (J') - F(J'') = 2B(J+1) \quad (2.8)$$

The inversely proportional relationship between the rotational constant (B) and the moment of inertia (I), demonstrated by equation (2.5), indicates that the rotational energy levels and, by extension, the rotational transition frequencies (2.8) are highly sensitive to the geometry, or more precisely the distribution of atomic masses, of the molecule. Therefore, each molecule, isotope, and conformer will have a unique moment of inertia and rotational spectrum fingerprint. The intensity of rotational transitions, which applies to molecular systems beyond just rigid linear molecules, is determined by the magnitude of the electric dipole moment components and the population of rotational energy levels. This is specifically important when dealing with molecules with multiple conformers, in which the most dominant spectral features are typically due to either the most populated conformer or to the one with the largest dipole moment components along any of the principal inertial axes a, b, and c.

2.3 Non-Linear Molecules

Non-linear molecules, such as the systems studied in this thesis, are those with three or more atoms not aligned along a single axis and their spectral patterns are more complex compared

to those of linear molecules. In linear molecules, there is only one unique, non-zero moment of inertia, which corresponds to rotation around the two equivalent axes perpendicular to the molecule's bond axis. In non-linear molecules, there are three non-zero moments of inertia (I_a, I_b, and I_c), which correlate to rotations around the three principal axes of the molecule (the a, b, and c axes). Based on the moment of inertia values, the molecules can be classified as:

1) Spherical Top, for example, CCl_4, $I_a = I_b = I_c$.
2) Symmetric Top, for example, $CHCl_3$ (prolate, $I_a < I_b = I_c$) and C_4H_4 (oblate, $I_a = I_b < I_c$).
3) Asymmetric Top, for example, NO_2, ($I_a < I_b < I_c$).

In the case of a rigid spherical top, the presence of an inversion center results in a zero permanent dipole moment, preventing it from displaying rotational transitions. In a rigid symmetric top, the Schrödinger equation solutions describing the allowable quantum states of a molecule depend on both the total rotational angular momentum, J and its projection (a new quantum number K is used) along the highest axis of symmetry. In term value equations used to explain the energy levels of symmetric top molecules, prolate and oblate tops are distinguished by using subscripts on the quantum number K where "a" is used for prolate tops, whereas "c" is used for oblate tops. The term value equations are:

$$F(J,K) = BJ(J+1) + (A-B)K_a^2 \tag{2.9}$$

$$F(J,K) = BJ(J+1) + (C-B)K_c^2 \tag{2.10}$$

where A, B and C are vibrational dependence of the rotational constants and are related to I_a ($\frac{h}{8\pi^2 I_a}$), I_b ($\frac{h}{8\pi^2 I_b}$) and I_c ($\frac{h}{8\pi^2 I_c}$), respectively, when expressed in frequency dimensions. The quantum number K can adopt values between 0 and J. The K value cannot be greater than J as the magnitude of the projection of the total angular momentum vector along the principal axis cannot

exceed the total angular momentum itself. If K > 0, the energy associated with clockwise and anticlockwise rotations about the principal axis is identical, resulting in a twofold degeneracy in the energy levels. There is no degeneracy, however, when K = 0, since there is no rotational angular momentum about the principal axis. In addition to the presence of a permanent dipole moment, the selection rule J = ±1 also applies to symmetric tops. Moreover, an additional selection rule ΔK = 0 must also be satisfied and the transition frequency is given as:

$$\upsilon_{J,K\rightarrow J+1,K} = F(J',K) - F(J'',K) = 2B(J+1) \tag{2.11}$$

While the equations for symmetric top molecules can be derived as shown above, for asymmetric molecules, the situation is more complicated, as there are no exact solutions for the Schrödinger equation. As a result, their spectra are analyzed by the relation between the prolate and oblate symmetric top limits, as shown in Figure 2.1. Three quantum labels, J, K_a, and K_c, which stand for the total rotational quantum number and the labels for the levels in the prolate and oblate limits, respectively, define the energy levels of asymmetric top molecules. Despite the fact that asymmetric molecules follow the selection rule ΔJ = 0, ±1, these molecules have three non-equivalent rotation axes (a, b, and c) and three dipole moment components (μ_a, μ_b, and μ_c), which leads to additional selection rules for transitions corresponding to each axis. These transitions are referred to as a-, b-, and c-type transitions and are guided by the selection criteria corresponding to the K_a and K_c quantum labels, presented below:

1) a-type transition: $\mu_a \neq 0$, $\Delta K_a = 0\ (\pm 2, \pm 4, \pm 6, \dots)$ and $\Delta K_c = \pm 1\ (\pm 3, \pm 5, \pm 7, \dots)$
2) b-type transition: $\mu_b \neq 0$, $\Delta K_a = \pm 1\ (\pm 3, \pm 5, \pm 7, \dots)$ and $\Delta K_c = \pm 1\ (\pm 3, \pm 5, \pm 7, \dots)$
3) c-type transition: $\mu_c \neq 0$, $\Delta K_a = \pm 1\ (\pm 3, \pm 5, \pm 7, \dots)$ and $\Delta K_c = 0\ (\pm 2, \pm 4, \pm 6, \dots)$

For instance, Figure 2.2 illustrates a-type (101 → 000), b-type (111 → 000), and c-type (110 →000) transitions (as emission), which can be distinguished by purple, dark blue and red arrows, respectively.

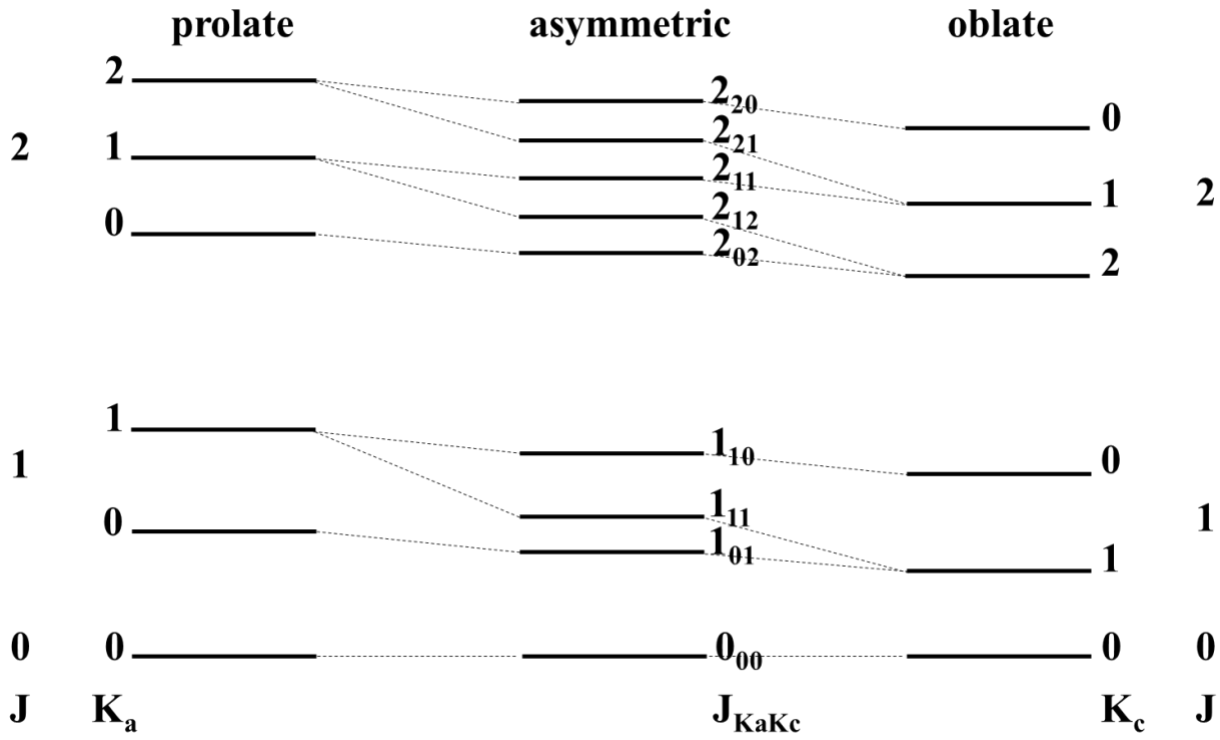

Figure 2.1 Rotational energy level correlation diagram for an asymmetric top considering the prolate and oblate symmetric top limit.

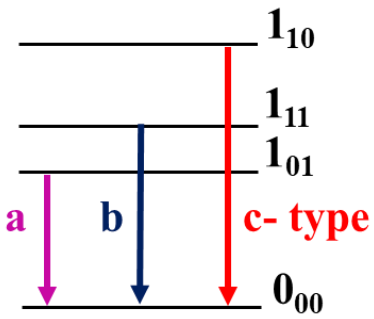

Figure 2.2 Rotational transitions of the a-, b-, and c-type (shown as emission).

2.4 Centrifugal Distortion

The energy equations for the rotational energy levels that were derived in previous sections follows the rigid rotor approximation, however, in reality, molecules are not completely rigid, and their geometry changes as they rotate due to centrifugal forces acting on their internuclear atomic distances. These distortions become more apparent at higher rotational energies, causing the energy difference between the rotational levels to decrease as J increases. Therefore, to account for these centrifugal distortions, additional terms must be added to the expressions describing the rotational energy levels. In the case of a diatomic molecule, for instance, the rigid rotor energy expression must be changed to incorporate a centrifugal distortion term, such as:

$$F(J) = BJ(J+1) - DJ^2(J+1)^2 \tag{2.12}$$

where D is the centrifugal distortion constant to account for the levels getting closer as J increases. The frequency equation becomes:

$$\nu_{J\rightarrow J+1} = F\,(J') - F(J'') = 2B(J+1) - 4D(J+1)^3$$

For example, for prolate symmetric tops, three distortion constants (D_J, D_{JK}, and D_K) are used, and the energy level and frequency equations are defined as:

$$F(J,K) = BJ(J+1) - D_J\big(J(J+1)\big)^2 + (A-B)K^2 - D_K K^4 - D_{JK}J(J+1)K^2 \tag{2.13}$$

$$\upsilon_{J,K\rightarrow J+1,K} = F(J',K) - F(J'',K) = 2B(J+1) - 4D_J(J+1)^3 - 2D_{JK}(J+1)K^2 \tag{2.14}$$

For asymmetric top molecules, five quartic centrifugal distortion constants (D_J, D_{JK}, D_K, d_1 and d_2, Watson S-reduced Hamiltonian or D_J, D_{JK}, D_K, d_j and d_k, Watson A-reduced Hamiltonian) are usually adequate to explain the distortions, however, for the high energy transitions, higher order terms like sextic or octic centrifugal distortion constants may be required.

2.5 Methyl internal rotation motion

The interconversion between equivalent configurations of a molecule can result in spectral rotational transitions exhibiting fine structure, also known as splitting patterns, if the barrier is low enough for tunnelling to occur. This effect, classified as a large amplitude motion, is often seen in molecules that have a methyl group that can spin about its C_3 internal axis to convert between three equivalent energy minima described by a 3-fold potential (V_3). The end-over-end rotational transitions of a molecule having a methyl rotor can prompt the rotational energy levels (and consequently, the spectral lines) to be perturbed by the internal motion which causes the levels to split into two states, labeled as A and E (referring to the degeneracy of the states). The magnitude of the A and E splitting depends on the energy barrier height for the methyl rotation, which can be influenced by electronic and steric effects in the molecule. Consequently, rotational spectroscopy is ideal to provide insights into the structure, barrier height, and dynamics of molecules that undergo large amplitude motions.

The potential energy function (V) that governs the internal motion of the methyl group periodically repeats itself with respect to the torsional angle (α) and is expressed as follows:

$$V(\alpha) = \frac{V_N}{2}(1 - cosN\alpha) + \frac{V_{2N}}{2}(1 - cos2N\alpha) + \cdots \quad (2.15)$$

where N is for a general N-fold barrier. Considering a three-fold methyl internal rotation (N = 3), equation 2.15 can be written as:

$$V(\alpha) = \frac{V_3}{2}(1 - cos3\alpha) + \frac{V_6}{2}(1 - cos6\alpha) + \cdots \quad (2.16)$$

and as $V_3 >> V_6$, the V_3 term alone gives a relatively accurate depiction of the true potential function for the molecules in this work and can be represented as:

$$V(\alpha) = \frac{V_3}{2}(1 - cos3\alpha) \tag{2.17}$$

where V_3 is the internal rotation barrier. Also, the internal rotational and the torsional energy levels can be expressed by the equation:

$$\frac{\hbar^2}{2I_r}\frac{d^2U(\alpha)}{d\alpha^2} + \left[\frac{V_3}{2}(1 - cos3\alpha) - E\right]U(\alpha) = 0 \tag{2.18}$$

where I_r is the reduced moment of inertia, E is the total energy, and U(α) stands for the methyl rotor wave function. Figure 2.3 depicts the potential barrier and torsional energy levels, with ν representing the torsional quantum number.

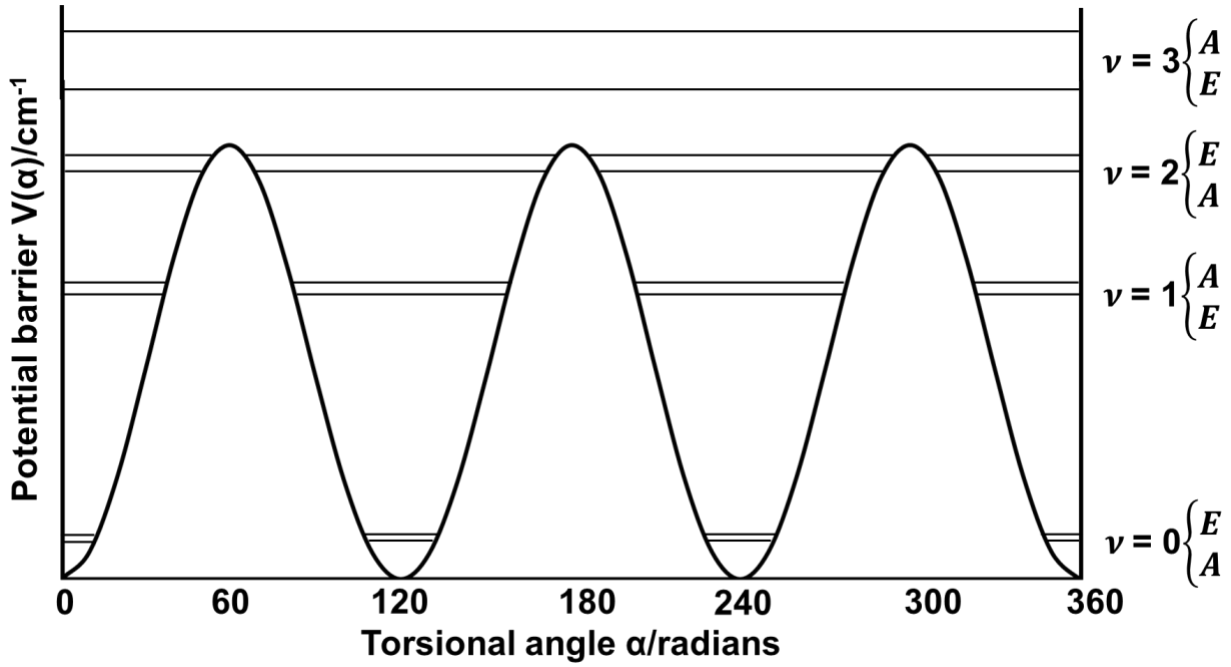

Figure 2.3 A potential barrier V_3 and its corresponding internal rotational levels.

In this dissertation, the splitting of the A and E states as a result of the methyl internal rotor has been detected and will be explained in greater detail in the later chapters. The next chapter will focus on the instrumentation of the microwave spectrometers designed specifically for this research as well as the computational methods used to facilitate the interpretation of the collected

spectra. By combining these approaches, a deeper understanding of the molecules under investigation can be achieved.

2.6 References

1 P. F. Bernath, *Spectra of atoms and molecules*, Oxford University Press: Oxford, 1st ed., 2015.

2 W. Gordy and R. L. Cook, *Microwave molecular spectra*, John Wiley & Sons Inc.: New York, 3rd ed., 1984.

3 J. M. Hollas, *Modern spectroscopy*, John Wiley & Sons Ltd: Chichester, 4th ed., 2004.

4 J. D. Kemp and K. S. Pitzer, Hindered rotation of the methyl groups in ethane, *J. Chem. Phys.*, 1936, **4**, 749.

5 C. C. Lin and J. D. Swalen, Internal rotation and microwave spectroscopy, *Rev. Mod. Phys.*, 1959, **31**, 841–891.

6 L. Goodman and V. Pophristic, Where does the dimethyl ether internal rotation barrier come from?, *Chem. Phys. Lett.*, 1996, **259**, 287–295.

7 R. K. Sinha, B. P. Singh and T. Kundu, Origin of threefold methyl torsional potential in methylindoles, *Theor. Chem. Acc.*, 2008, **121**, 59–70.

8 I. Kleiner, Asymmetric-top molecules containing one methyl-like internal rotor: Methods and codes for fitting and predicting spectra, *J. Mol. Spectrosc.*, 2010, **260**, 1–18.

9 I. Kleiner, Spectroscopy of interstellar internal rotors: An important tool for investigating interstellar chemistry, *ACS Earth Sp. Chem.*, 2019, **3**, 1812–1842.

10 H. V. L. Nguyen and I. Kleiner, Understanding (coupled) large amplitude motions: The interplay of microwave spectroscopy, spectral modeling, and quantum chemistry, *Theor.*

Comput. Chem. Appl. Ind. Pharma, Mater. Sci., 2021, 41–92.

Chapter 3. Microwave Spectroscopy Instrumentation and Computational Chemistry

3.1 Fourier Transform Microwave (FTMW) Spectroscopy Instrumentation

After introducing the theoretical principles of rotational spectroscopy, the next step involves venturing into the intricate laboratory processes of collecting the rotational spectra. In this thesis, two custom built Fourier transform microwave (FTMW) spectrometers, the cavity-based or Balle-Flygare FTMW spectrometer (BF-FTMW) and the chirped pulse FTMW (cp-FTMW) spectrometer, were used to record pure rotational transitions in the microwave region. Generally, conducting experiments on a desired chemical system, which may be commercially available or will be produced under experimental conditions from suitable precursors, requires first a sequence of quantum mechanical calculations to determine its stable conformers and their rotational constants, which is key information for the spectroscopic measurements. Once the molecule is acquired, the cp-FTMW spectrometer is used to obtain a broadband spectrum within the frequency range of 8 to 18 GHz, providing an overview spectrum of the rotational transitions of different species (conformers, isotopologues) in the molecular system. Subsequently, a cavity-based FTMW spectrometer is used to carry out the final frequency measurements, usually between 4 and 26 GHz. This cutting-edge instrument offers exceptional resolution and sensitivity, facilitating the measurement of a wide range of rotational transitions, including those from minor isotopologues in natural abundance.

3.1.1 Sample Injection and Supersonic Jet Expansion

In this dissertation, a gas mixture comprising of a small amount (~1%) of the sample diluted in an inert gas (e.g., neon, 100-200 kPa) was meticulously prepared at room temperature for both

cp-FTMW and BF-FTMW spectrometers. A pulsed solenoid nozzle with a circular orifice of 1 mm diameter was used to inject the gas mixture into the high vacuum chamber (~10^{-6} Torr) of the spectrometers. As all of the molecules investigated in this thesis are low-boiling point liquids with high vapor pressures at room temperature, including diallyl sulfide (DAS) and diallyl ether (DAE) in chapter 4, allyl ethyl ether (AEE) and allyl ethyl sulfide (AES) in chapter 5, and propyl vinyl ether (PVE) and butyl vinyl ether (BVE) in chapter 6, they were collected directly as vapors in a mixing chamber and diluted with the inert gas, as mentioned above. To create water adducts, such as the diallyl ether-water (DAE-w) and diallyl sulfide-water (DAS-w) complexes in chapter 7, the gas mixture (sample + Ne) was bubbled through a water-containing reservoir placed outside the chamber.

The expansion of the gas mixture in the high-vacuum environment of the spectrometer resulted in a supersonic jet expansion or molecular beam, which cools down the rotational temperature of the sample to a few Kelvin. The low temperature of the collision-free jet enhances the lowest rotational energy states population and, sometimes, even enables the detection of rotational transitions within vibrationally excited states. This generally improves peak resolution and reduces peak broadening due to collisions as molecules travel in the same direction with the same velocity.

After the gas mixture was rotationally excited by inserting a microwave pulse into the chamber, the relaxation process of the sample was observed by recording the free induction decay (FID) in the time domain. Finally, the frequency spectrum was obtained by applying a fast Fourier transformation (FFT) to the FID signals.

3.1.2 Chirped-Pulse FTMW Spectrometer

In 2006, Prof. Dr. Brooks Pate's team[1,2] at the University of Virginia pioneered the development of the chirped-pulse FTMW spectrometer, an incredibly powerful instrument that can capture a wide spectrum spanning multiple GHz all at once. This breakthrough innovation has significantly increased the speed of data collection, enabling researchers to perform experiments that were once considered challenging. The van Wijngaarden laboratory uses a custom-built spectrometer (depicted in Figure 3.1) with a frequency range of 8 to 18 GHz, capable of acquiring spectra with a bandwidth of up to 6 GHz which each pulse.[3] The vacuum chamber of the spectrometer houses two high-gain horn antennae, one for transmitting the microwave pulse or chirp pulse (linear frequency sweep) and the other for receiving the emitted microwave radiation. The linear frequency sweep is created by an arbitrary waveform generator (AWG), and after, is combined with microwave radiation from a microwave signal synthesizer. In general, in the work described in this thesis, the pulse sweeps the frequency linearly from a center frequency (ν_o) to ±1 GHz (ν_w) within a very short time interval of 1-5 μs for a 2 GHz frequency window measurement, but in principle, each measurement can cover up to a bandwidth of 6 GHz. The sample molecules are rotationally excited by this pulse, rotating at frequencies within this band of radiation, and ultimately leading to the generation of a broadband spectrum comprising of rotational transitions over the entire bandwidth for every excitation pulse.

The excitation pulse is first amplified to 25 W using a solid-state amplifier to ensure sufficient power, before being introduced into the vacuum chamber. The gas sample is inserted into the chamber using a solenoid pulsed nozzle, which is perpendicular to the excitation and detection axis. The sample is then polarized using a microwave pulse broadcast by a high-gain horn antenna. The rotational frequencies of all excited transitions within the chirp range are

received by a second horn antenna on the opposite side of the chamber. After downconverting the amplified emission, the signal FIDs are digitized with a powerful, fast oscilloscope whose high sampling rate allows processing of the full band of frequencies with each pulse sequence. In the cp-FTMW experiment, millions of FIDs are typically collected over several hours to phase-coherently average the broadband molecular signal and improve spectrum quality. The resulting signals are subjected to FFT to convert the time-domain signal to the frequency domain. The spectrum typically exhibits linewidths ranging from 150-200 kHz (Full Width at Half Maximum, FWHM), with an experimental repetition rate of around 5 Hz. Although the cp-FTMW spectrometer allows for swift acquisition of a broad frequency range, its lack of a resonant cavity compromises both sensitivity and resolution. Therefore, the cp-FTMW spectrum is primarily used for an initial survey to guide further measurements of transitions using the BF-FTMW instrument which boasts higher sensitivity and resolution.

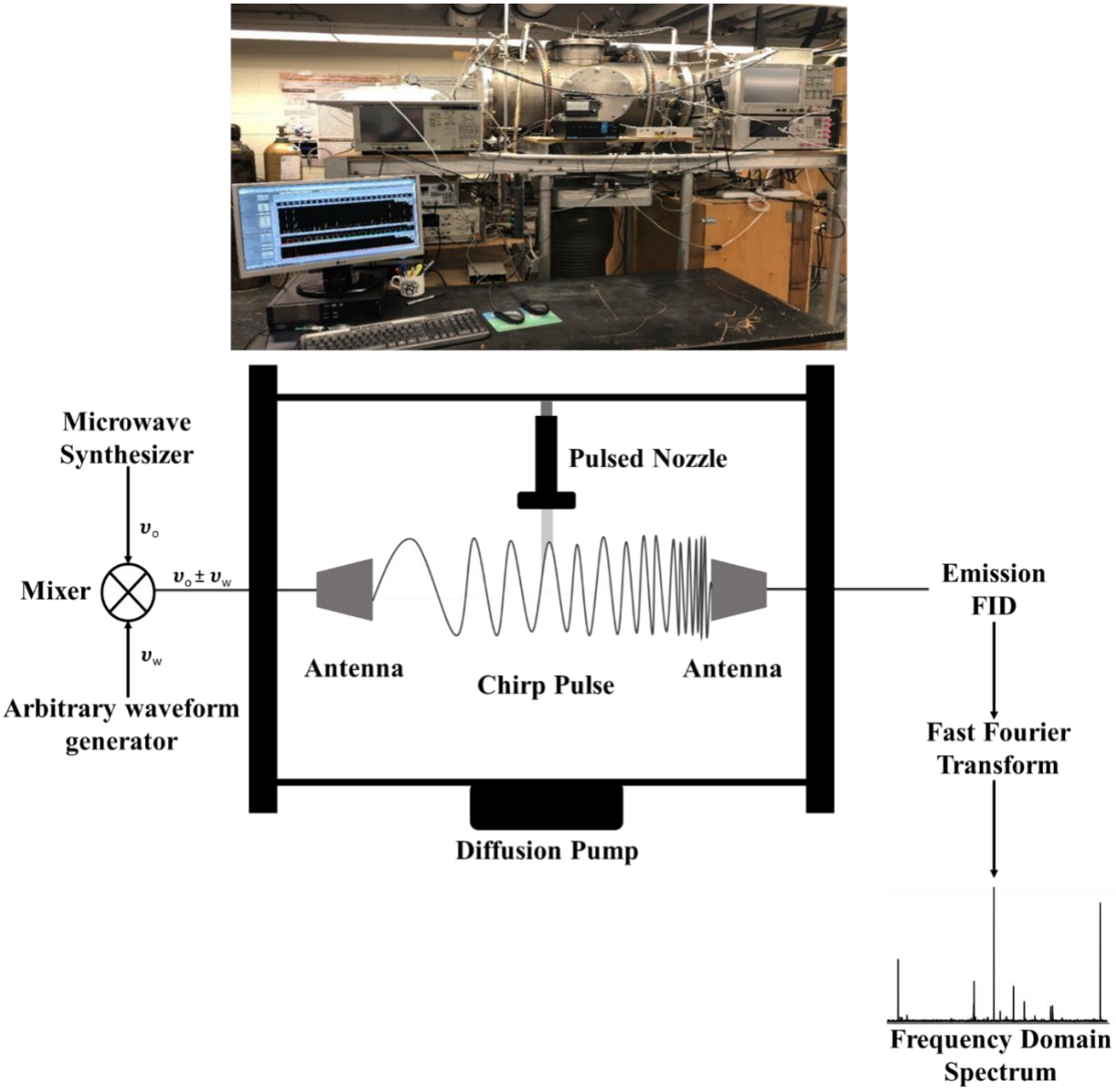

Figure 3.1 Simplified scheme of the broadband CP-FTMW spectrometer used in this thesis. The full details can be found in reference 3.

3.1.3 Balle-Flygare (BF) FTMW Spectrometer

The van Wijngaarden lab[4] has a custom-built cavity-based BF-FTMW operating within the 4-26 GHz microwave frequency range, following the Balle-Flygare design.[5] The spectrometer is a narrowband instrument that can accurately collect individual rotational transitions within a frequency window of 1 MHz or less. The spectrometer is composed of three primary components: a Fabry-Pérot cavity, an excitation circuit, and a detection circuit, which are illustrated in Figure 3.2.

The cavity is constructed within a 300 L stainless steel chamber that operates under a high vacuum pressure of ~10^{-6} Torr. It is composed of two 36 cm diameter concave aluminum mirrors, one of which is stationary, and the other movable, to form a resonator that traps the microwave signal. The movable mirror is regulated by a servo motor to adjust the cavity to the corresponding frequency, enabling the acquisition of the spectrum of a desired rotational transition. The cavity resonance can be checked using an L-shaped hook antenna, positioned at the center of the stationary mirror, while the second antenna on the movable mirror broadcasts the excited signal and receives the emitted signals from molecules. The resonant cavity functions to trap the microwave field, providing exceptional sensitivity (improved signal-to-noise ratio) and high resolution (linewidth of 7 kHz FWHM) for the collection of transitions.

The gas sample is injected into the cavity via a pulsed solenoid nozzle positioned slightly below the center of the movable mirror. Typically, the gas pulse lasts for approximately 1000 μs. To excite the sample, a microwave pulse with a duration of about ~5 μs is generated by mixing the continuous wave radiation produced by a microwave synthesizer and radiofrequency generator using a single sideband mixer. The resulting excitation radiation is delivered to the cavity through a L-shaped wire hook antenna situated in the moving mirror. During this process, a single pole

double throw (SPDT) switch is used to protect the detection circuit from the intense microwave input. When the sample interacts with the excitation pulse inside the cavity, the dipole moments of the molecules align, resulting in a rotating macroscopic polarization of the sample, assuming the cavity is tuned to a molecular resonance. After the polarization of the sample, the signal path is then switched to the detection circuit. The weak emission signal received by the antenna is subsequently amplified and the FIDs resulting from the relaxation of the ensemble is recorded. To avoid the expense of directly sampling the digitized signals, the resulting signal is mixed with a microwave signal to downconvert it to a lower frequency range (~30 MHz), and then further downconverted to ~2.5 MHz using a 27.5 MHz signal from a radiofrequency synthesizer. A digitizer with a sampling rate greater than 1.25 MHz can process the digitized signal, which is subsequently converted into a digital format by an A/D converter in the computer. After that the signal is FFT in the frequency domain spectrum. To enhance the signal-to-noise ratio (SNR) of a weak emission signal, multiple phase-synchronized experiment cycles are averaged. This process can be done phase coherently by repeating the pulse sequence and averaging the emission signal, which is referenced to the 10 MHz system clock. Also, the coaxial arrangement of the sample and resonator axis causes rotational transitions to produce doublets in the frequency domain due to the Doppler effect, as shown in Figure 3.2.

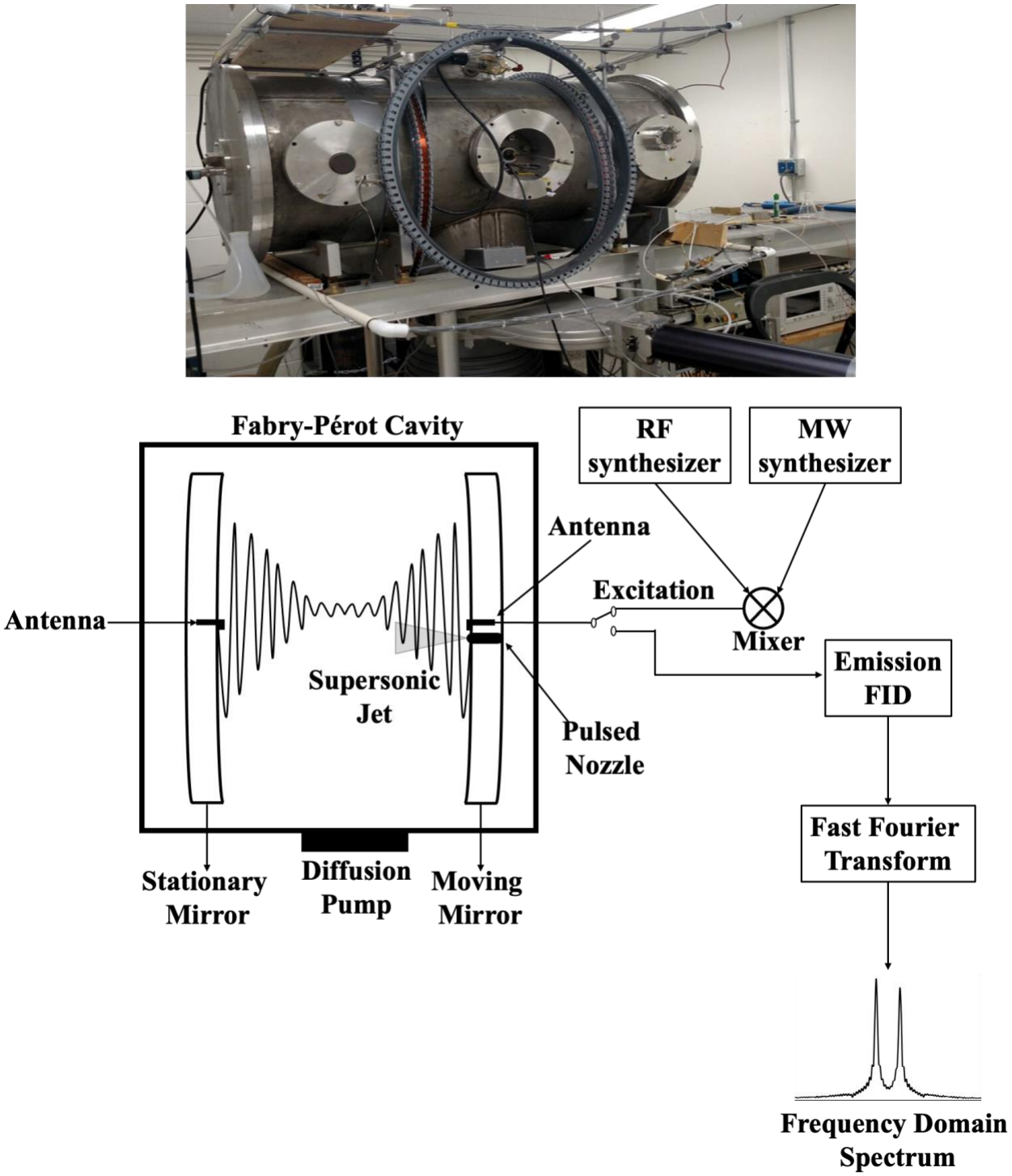

Figure 3.2 An image and a simplified scheme of a narrowband BF-FTMW spectrometer. The full details can be found in the reference 4.

As explained above, cavity-based FTMW spectrometers offer significant advantages in terms of sensitivity and resolution. However, its application is limited by the narrow excitation bandwidth, which makes studying complex molecular systems with dense spectra and multiple transitions from numerous conformers that requires separate acquisitions a time-consuming and laborious process. As a result, using a cp-FTMW instrument to collect survey spectra in combination with a BF-FTMW instrument for higher resolution and sensitivity measurements is a recommended approach in typical rotational spectroscopic studies. To guide the search for spectral data, extensive quantum chemical calculations were performed in this thesis since there were no prior reports on the molecular systems investigated. The next section contains a detailed description of the computational methods used.

3.2 Computational Chemistry

3.2.1 Conformational Search

Quantum mechanical calculations play an important role in guiding rotational spectroscopic studies. High level quantum chemical calculations are performed to anticipate critical spectroscopic parameters such as rotational constants, distortion constants and dipole moments, before collecting the rotational spectrum. To comprehend a molecule's conformational equilibrium, the initial step is to investigate its potential energy surface (PES), which characterizes the system's energy with respect to its internal coordinates. As all the molecules investigated in this thesis are large flexible molecules or monohydrated complexes, the preliminary analysis entails conformational searches to identify potential energy minima on the PES. The next step involves carrying out geometry optimization and frequency calculations.

Given that the molecules studied in this thesis are flexible consisting of molecular geometries with more than two dihedral angles, an automated conformational search is used

instead of modeling various points on the PES manually. To accomplish this, the GFN2-xTB, a semi-empirical quantum chemical method developed by Grimme *et al.*,[6] was employed. This approach incorporates an exchange-correlation correction with an electrostatic interaction to approximate the density-dependent dispersion and electron-electron interaction. This correction is essential to accurately model the non-covalent forces, particularly in weakly-bound complexes. Grimme *et al.*[6] have integrated the GFN2-xTB method into the conformer-rotamer ensemble sampling tool (CREST),[7,8] for conformational searches. Using the CREST tool, the chemical space of both monomers and molecular adducts can be analyzed automatically. Once all the possible geometries of the studied molecules are obtained by the search, higher level quantum chemical calculations are employed to optimize and calculate vibrational frequencies of each geometry. To accomplish this, the Gaussian 16 program[9] is used to implement the dispersion-corrected density functional theory (DFT) B3LYP-D3(BJ)[10–12] method, along with Dunning's aug-cc-pVTZ[13] basis set.

The resulting (optimized) geometries can be sorted by energy to determine their relative stabilities, and their corresponding rotational constants and dipole moment components are obtained to guide spectral searches. The frequency calculations, typically performed within the harmonic approximation, enable the computation of vibrational frequencies, providing zero-point energy (ZPE) corrections, and quartic centrifugal distortion constants. Additionally, the presence or absence of imaginary frequencies indicates whether the stationary points are true energy minima geometries or transition states. This multi-step procedure is crucial to pinpoint the most promising experimental candidates, such as low-energy conformers, which are the dominant species in the conformational equilibrium and thus, the primary targets for assignment in the rotational spectrum.

3.2.2 Spectral Analysis and Structure Determination

After identifying the spectral pattern of a targeted conformer candidate, the corresponding experimental line positions can be manually assigned to their respective transition quantum numbers. The PGOPHER[14] software is used to estimate a set of experimental rotational constants with reasonable accuracy using least squares fitting to a suitable Hamiltonian (usually Watson's asymmetric (A) or symmetric (S) Hamiltonian).[15] A portion of the assigned spectrum of the DAE[16] is shown in Figure 3.3 as an example.

The obtained rotational constants from the PGOPHER fits are used to predict transitions within the frequency range of 4–26 GHz in the BF-FTMW spectrometer, which has a resolution of ~7 kHz and is capable of detecting transitions with an accuracy of ~1 kHz. Pickett's SPFIT[17] program is then used for final fits to acquire precise rotational and centrifugal distortion constants. The XIAM software[17,18] is employed to fit molecules with a methyl rotor that exhibit an observable A and E state splitting. This software uses the combined axis method (CAM) and determines crucial parameters for the molecule and the methyl rotor, such as the V_3 barrier.

When studying rotational spectra of flexible molecules with multiple conformations, some transitions of certain conformers may be missing from the spectrum despite being populated and possessing significant dipole moments. This may occur due to relaxation where a higher energy form is converted to a lower energy one at the start of the supersonic jet expansion as a result of collisions with the inert gas. Empirical evidence suggests that if the interconversion barrier between conformers is below ~5 kJ mol^{-1}, relaxation is likely to occur, such as those shown in Figure 3.4 for AEE and AES.[19]

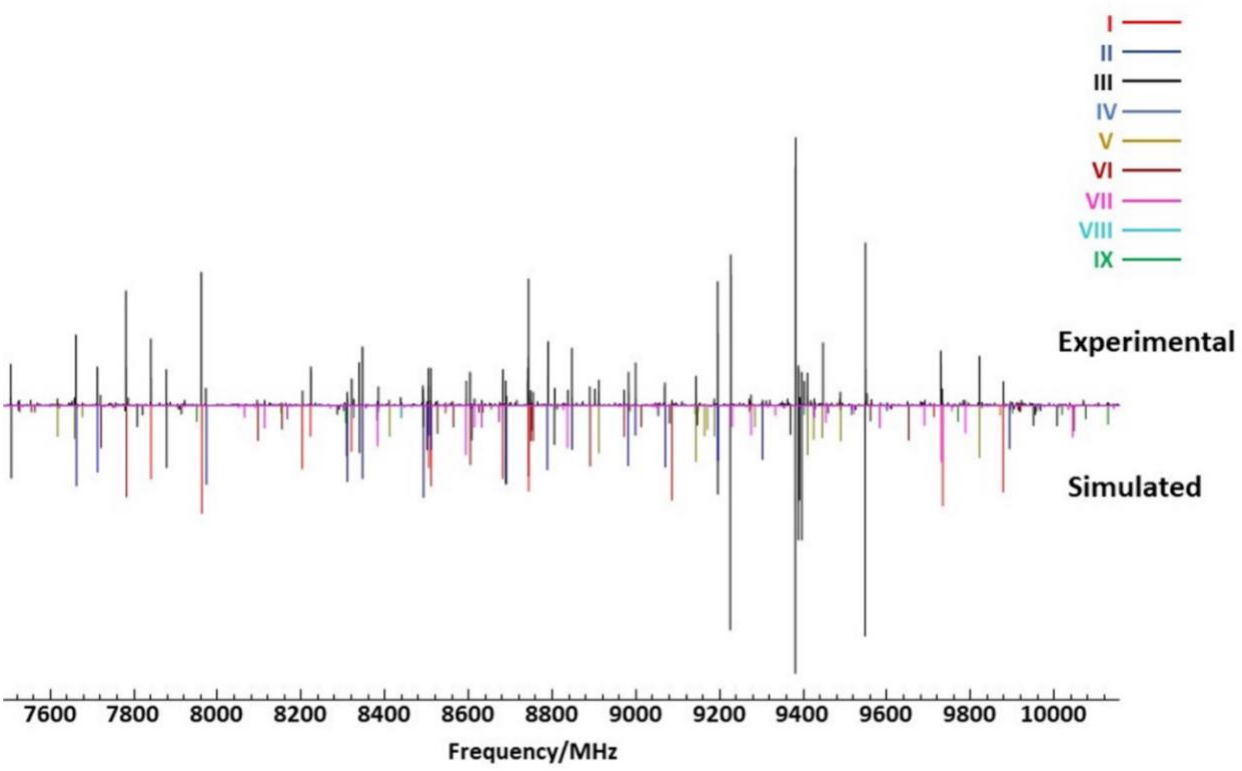

Figure 3.3 A segment of the broadband cp-FTMW spectrum (average of 1.5 million free induction decays) of DAE displaying the rotational transitions for the nine lowest energy conformers. Conformers were labeled with Roman numerals to indicate their stability ordering, which was determined based on their relative energy, with conformer I predicted to be the most stable. The top part of the figure depicts the experimental spectrum, while the simulated spectrum is shown at the bottom.[16]

Also, rotational transitions of isotopologues substituted with a single heavy atom can be observed for molecular systems alongside the transitions of their parent species. The unique rotational fingerprints of each isotope are a result of isotopic substitution affecting only the moments of inertia and rotational constant parameters of the studied molecule. In this thesis, transitions due to isotopes in natural abundance, such as ^{13}C and ^{34}S, are detected. To estimate the rotational constants for isotopes, Kisiel's PMIFST[17] program is used where the masses of individual atoms in the optimized molecular geometry are replaced one by one to estimate the new moments of inertia. With the observation of rotational spectra due to the parent and singly

substituted isotopologues, the geometry of the studied molecules is obtained using the experimentally derived rotational constants. Two different software programs, KRA[17] and STRFIT,[17] are used to derive the substitution (r_s)[20] and the ground state effective (r_0)[21,22] structures, respectively. The r_s method is an approach employed to determine the positions of substituted atoms within a molecule. By using Kraitchman's equations,[23] it computes the coordinates of each substituted atom along the a, b, and c inertial axes of the parent molecule. These equations consider the mass distribution of the parent molecule and the positions of non-substituted atoms to accurately determine the positions of the substituted atoms within the molecule. The r_0 structure is a fitting method that uses experimental rotational constants to determine the molecular structure of a molecule in its ground vibrational state. Equilibrium r_e values are used for non-substituted atoms, but the accuracy of the r_0 fit can be limited if the molecule undergoes significant low-lying vibrational distortions.

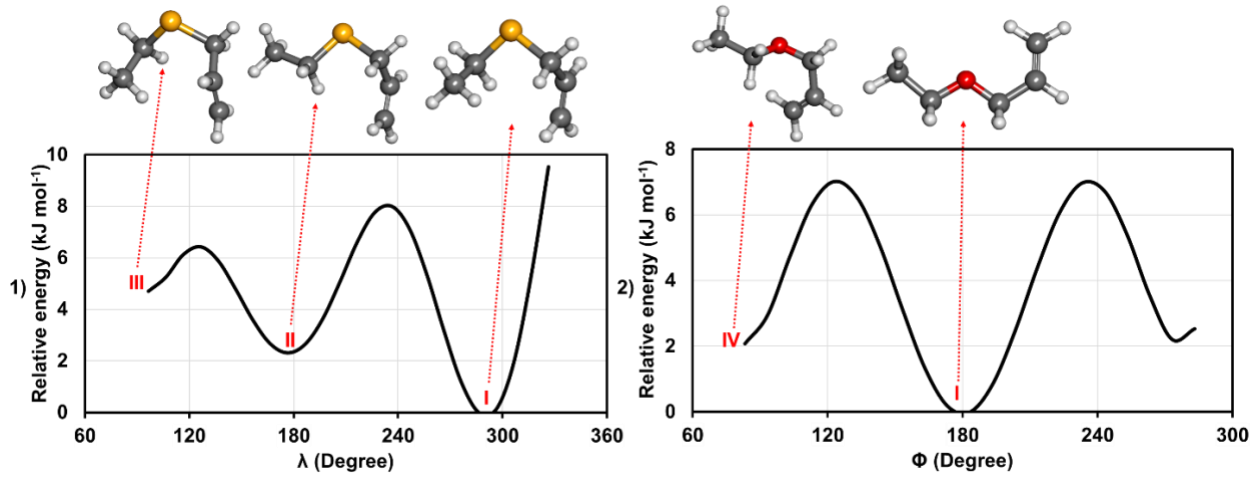

Figure 3.4 Interconversion relaxation pathways of 1) allyl ethyl sulfide = conformer III → conformer II (barrier ~1.7 kJ mol^{-1}) and 2) allyl ethyl ether = conformer IV → conformer I (barrier ~4.9 kJ mol^{-1}) calculated at the B3LYP-D3(BJ)/aug-cc-pVTZ level of theory.[19]

3.2.3 Conformational Preferences

Experimentally, one can confirm the presence and geometric characteristics of conformers, but the reasons behind their favored geometries can only be elucidated through quantum mechanical calculations. In this regard, four different methods were used to investigate the non-covalent intramolecular and intermolecular interactions ruling the conformational preferences in the studied systems, namely natural bond orbital (NBO),[24] symmetry-adapted perturbation theory (SAPT),[25] quantum theory of atoms in molecules (QTAIM),[26] and non-covalent interaction (NCI) analysis.[27] These methods were executed using the programs NBO7,[28] Psi4,[29] AIMALL,[30] and NCIPLOT,[31] respectively.

NBO analysis is used to study the bonding and general electronic structure in molecules. It is based on the concept of Natural Bond Orbitals, which represent the Lewis-type bonds and lone pairs in a molecule. The method uses second-order perturbation theory to determine the contribution of each Lewis structure to the overall molecular wave function, which is represented by the following equation:

$$\Delta E_{i\to j}^{(2)} = q_i \frac{|F(i,j)|^2}{\varepsilon_j - \varepsilon_i} \qquad 3.1$$

where, the energy (second order perturbation theory corrections) related to the orbital interaction is denoted by $\Delta E^{(2)}$, while q_i represents the donor orbital occupancy, the degree of overlap between the donor and acceptor orbitals is given by the Kohn-Sham matrix element |F(i,j)| and the donor and acceptor orbital energies are denoted as ε_i and ε_j, respectively. Basically, a strong interaction between the orbitals is determined by a larger value of $\Delta E^{(2)}$, which indicates a smaller energy gap between the interacting orbitals and a favorable overlap between them.

SAPT is an approach that allows the total interaction energy of a molecular complex to be separated into four distinct components: electrostatic, exchange, induction, and dispersion. These individual components can be used to better understand the physical nature of intermolecular contacts and identify the primary energy contributor that drives complex formation. Additionally, by comparing SAPT results for similar complexes, one can determine the impact of functional groups or atomic substitutions on the intermolecular interaction energy.

The QTAIM theory involves analyzing molecular electron density (ρ) to establish a connection between molecular geometry and chemical bonding. This is achieved by dissecting the molecular system into its constituent atomic fragments, allowing for the identification of atomic positions and the assessment of forces between them based on each atom's ρ within the molecule. To determine chemical bonding between two atoms, QTAIM employs two crucial parameters, the bond critical point (BCP) and the bond path (BP). The BCP represents a saddle point within the electron density space, signifying a minimum in ρ along the bonding direction but a maximum in other directions. In contrast, the BP serves as a spatial arrangement, akin to a chemical bond in a Lewis-type structure. It traces a path in three-dimensional space where electron density (ρ) attains its maximum value. Besides these two, there are other critical points, such as ring critical point (RCP), which emerge in the presence of a cyclic structure. In QTAIM molecular graphs, BPs are depicted as solid or dashed lines, while BCPs are marked by green dots, as shown in Figure 3.5 for DAE-w and DAS-w (Chapter 7). Also, QTAIM analysis gives quantitative data at each critical point, including values for the Laplacian, electron density, and potential energy (V). These values can subsequently be used to assess the strength of individual interactions by calculating their respective energies. In Chapter 7 of this thesis, the energy of the interaction for the molecules

studied were calculated as $0.5 \times V$, where V is the potential energy at the bond critical point, following the approach suggested by Espinosa et al.[32]

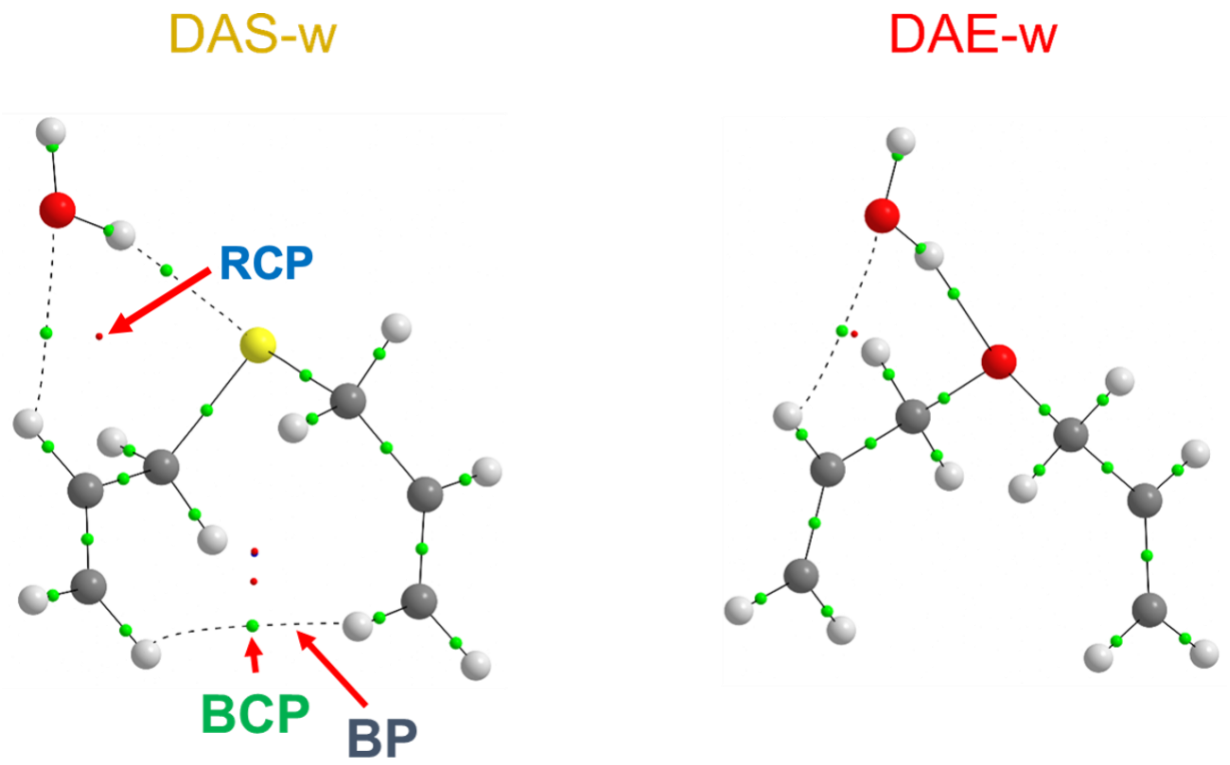

Figure 3.5 DAS-w and DAE-w molecular interaction graphs obtained using QTAIM.

The NCI analysis uses the reduced electron density gradients (*s*) to rigorously identify and characterize non-covalent interactions present in chemical systems. Visualization of non-covalent forces within a molecule is achieved through isosurfaces of *s* at low electron density (ρ). While ρ is helpful in identifying non-covalent interactions and their strength, the sign of the Laplacian of the electron density ($\nabla^2\rho$) is a superior indicator for distinguishing weak (such as van der Waals) from strong attractive or repulsive interactions. The second eigenvalue of the ρ Hessian matrix allows one to differentiate between attractive λ_2 = negative (< 0) and repulsive λ_2 = positive (> 0) interactions. Results of NCI analysis are often presented as gradient isosurfaces that are colored

based on the sign(λ_2)ρ values, with blue representing strong attractive, red representing strong repulsive, and green representing weak van der Waals interactions. As an illustration, the isosurfaces depicted in Figure 3.6 for DAE and DAS[16] shows that the NCI graphs demonstrating the absence of considerable strong attractive interactions (blue isosurfaces). Instead, green isosurfaces suggestive of weak contacts (either attractive or repulsive) are visible, implying that the interactions do not have a significant effect on the stability of the conformers I of DAE and DAS.

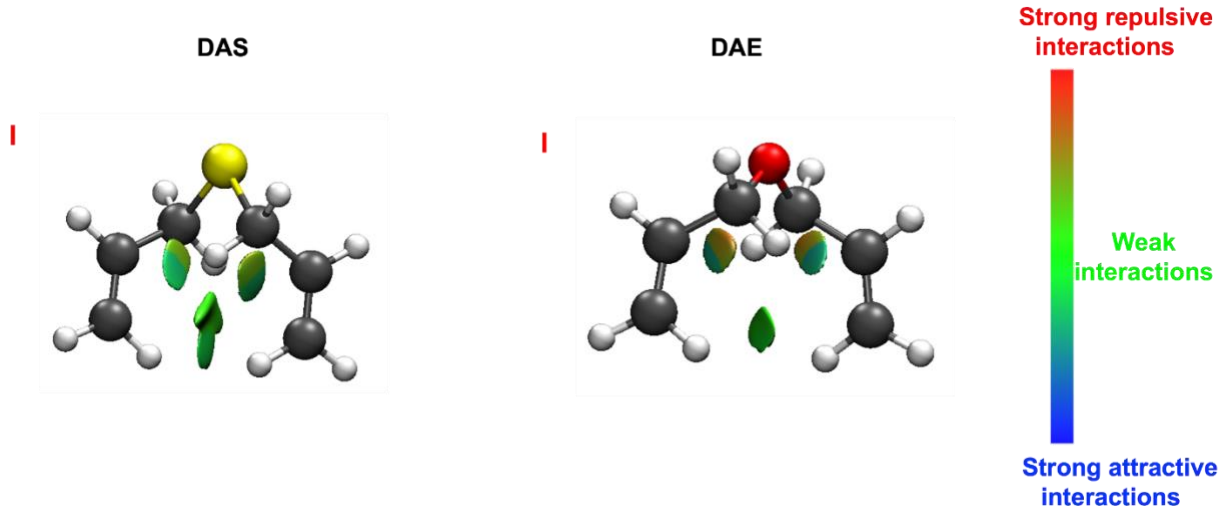

Figure 3.6 NCI isosurfaces (s = 0.05, color scale for -0.02 < ρ < + 0.02 au) for conformer I of DAS and DAE respectively.

The upcoming chapters use rotational spectroscopy and computational chemistry to investigate large flexible monomers and complexes with water for two of these species. The aforementioned methods were essential for these studies which aim to provide molecular level

understanding of the conformational preferences and underlying stereoelectronic effects ruling the conformational preferences of the systems.

3.3 References

1 G. G. Brown, B. C. Dian, K. O. Douglass, S. M. Geyer and B. H. Pate, The rotational spectrum of epifluorohydrin measured by chirped-pulse Fourier transform microwave spectroscopy, *J. Mol. Spectrosc.*, 2006, **238**, 200–212.

2 G. G. Brown, B. C. Dian, K. O. Douglass, S. M. Geyer, S. T. Shipman and B. H. Pate, A broadband Fourier transform microwave spectrometer based on chirped pulse excitation, *Rev. Sci. Instrum.*, , 2008, **79**, 053103.

3 L. Evangelisti, G. Sedo and J. van Wijngaarden, Rotational Spectrum of 1,1,1-Trifluoro-2-butanone Using Chirped-Pulse Fourier Transform Microwave Spectroscopy, *J. Phys. Chem. A*, 2011, **115**, 685–690.

4 G. Sedo and J. van Wijngaarden, Fourier transform microwave spectra of a “new” isomer of OCS-CO_2, *J. Chem. Phys.*, 2009, **131**, 044303.

5 T. J. Balle and W. H. Flygare, Fabry-Perot cavity pulsed Fourier transform microwave spectrometer with a pulsed nozzle particle source, *Rev. Sci. Instrum.*, 1981, **52**, 33–45.

6 C. Bannwarth, S. Ehlert and S. Grimme, GFN2-xTB - An Accurate and Broadly Parametrized Self-Consistent Tight-Binding Quantum Chemical Method with Multipole Electrostatics and Density-Dependent Dispersion Contributions, *J. Chem. Theory Comput.*, 2019, **15**, 1652–1671.

7 P. Pracht, F. Bohle and S. Grimme, Automated exploration of the low-energy chemical space with fast quantum chemical methods, *Phys. Chem. Chem. Phys.*, 2020, **22**, 7169–

7192.

8 S. Grimme, Exploration of Chemical Compound, Conformer, and Reaction Space with Meta-Dynamics Simulations Based on Tight-Binding Quantum Chemical Calculations, *J. Chem. Theory Comput.*, 2019, **15**, 2847–2862.

9 M. J. Frisch, G. W. Trucks, H. B. Schlegel, G. E. Scuseria, M. A. Robb, J. R. Cheeseman, G. Scalmani, V. Barone, B. Mennucci, G. A. Petersson, H. Nakatsuji, M. Caricato, X. Li, H. P. Hratchian, A. F. Izmaylov, J. Bloino, G. Zheng, J. L. Sonnenberg, M. Hada, M. Ehara, Fukuda, K. T. R., J. Hasegawa, M. Ishida, T. Nakajima, Y. Honda, O. Kitao, H. Nakai, T. Vreven, J. A. Montgomery, J. E. Peralta, F. Ogliaro, M. Bearpark, J. J. Heyd, E. Brothers, K. N. Kudin, V. N. Staroverov, R. Kobayashi, J. Normand, K. Raghavachari, A. Rendell, J. C. Burant, S. S. Iyengar, J. Tomasi, M. Cossi, N. Rega, J. M. Millam, M. Klene, J. E. Knox, J. B. Cross, V. Bakken, C. Adamo, J. Jaramillo, R. Gomperts, R. E. Stratmann, O. Yazyev, A. J. Austin, R. Cammi, C. Pomelli, J. W. Ochterski, R. L. Martin, K. Morokuma, V. G. Zakrzewski, G. A. Voth, P. Salvador, J. J. Dannenberg, S. Dapprich, A. D. Daniels, Farkas, J. B. Foresman, J. V Ortiz, J. Cioslowski and D. J. Fox, Gaussian 16 (Revision C.01), Gaussian, Inc., Wallingford CT, 2016.

10 A. D. Becke, Density-functional Thermochemistry. III. The Role of Exact Exchange, *J. Chem. Phys.*, 1993, **98**, 5648–5652.

11 S. Grimme, S. Ehrlich and L. Goerigk, Effect of the damping function in dispersion corrected density functional theory, *J. Comput. Chem.*, 2011, **32**, 1456–1465.

12 S. Grimme, J. Antony, S. Ehrlich and H. Krieg, A consistent and accurate *ab initio* parametrization of density functional dispersion correction (DFT-D) for the 94 elements H-Pu, *J. Chem. Phys.*, 2010, **132**, 1–19.

13 T. H. Dunning, Gaussian basis sets for use in correlated molecular calculations. I. The atoms boron through neon and hydrogen, *J. Chem. Phys.*, 1989, **90**, 1007–1023.

14 C. M. Western, PGOPHER: A program for simulating rotational, vibrational and electronic spectra, *J. Quant. Spectrosc. Radiat. Transf.*, 2017, **186**, 221–242.

15 J. K. G. Watson, Determination of centrifugal distortion coefficients of asymmetric-top molecules. III. Sextic coefficients, *J. Chem. Phys.*, 1968, **48**, 4517–4524.

16 T. Poonia, W. G. D. P. Silva and J. van Wijngaarden, Dramatic differences in the conformational equilibria of chalcogen-bridged compounds: The case of diallyl ether versus diallyl sulfide, *Phys. Chem. Chem. Phys.*, 2022, **24**, 240–248.

17 Z. Kisiel, *Spectroscopy from Space*, Kluwer Academic Publishers, 2001, 91–106.

18 H. Hartwig and H. Dreizler, The microwave spectrum of trans-2,3-dimethyloxirane in torsional excited states, *Zeitschrift fur Naturforsch. - Sect. A J. Phys. Sci.*, 1996, **51**, 923–932.

19 T. Poonia and J. Van Wijngaarden, Exploring the distinct conformational preferences of allyl ethyl ether and allyl ethyl sulfide using rotational spectroscopy and computational chemistry, 2023, **158**, 224301.

20 C. C. Costain, Further Comments on the Accuracy of R Substitution Structures, *Trans. Am. Crystallogr. Assoc.*, 1966, **2**, 157–164.

21 J. K. G. Watson, A. Roytburg and W. Ulrich, Least-Squares Mass-Dependence Molecular Structures, 1999, **119**, 102–119.

22 Z. Kisiel, Least-squares mass-dependence molecular structures for selected weakly bound intermolecular clusters, *J. Mol. Spectrosc.*, 2003, **218**, 58–67.

23 J. Kraitchman, Determination of Molecular Structure from Microwave Spectroscopic Data,

Am. J. Phys., 1953, **21**, 17–24.

24 F. Weinhold, C. R. Landis and E. D. Glendening, What is NBO analysis and how is it useful?, *Int. Rev. Phys. Chem.*, 2016, **35**, 399–440.

25 B. Jeziorski, R. Moszynski and K. Szalewicz, Perturbation Theory Approach to Intermolecular Potential Energy Surfaces of van der Waals Complexes, *Chem. Rev.*, 1994, **94**, 1887–1930.

26 R. F. W. Bader, Atoms in Molecules, *Acc. Chem. Res.*, 1985, **18**, 9–15.

27 E. R. Johnson, S. Keinan, P. Mori-Sánchez, J. Contreras-García, A. J. Cohen and W. Yang, Revealing noncovalent interactions, *J. Am. Chem. Soc.*, 2010, **132**, 6498–6506.

28 E. D. Glendening, J. K. Badenhoop, A. E. Reed, J. E. Carpenter, J. A. Bohmann, C. M. Morales, P. Karafiloglou, C. R. Landis and F. Weinhold, NBO 7.0., Theoretical Chemistry Institute, University of Wisconsin, Madison, 2018.

29 R. M. Parrish, L. A. Burns, D. G. A. Smith, A. C. Simmonett, A. E. DePrince, E. G. Hohenstein, U. Bozkaya, A. Y. Sokolov, R. Di Remigio, R. M. Richard, J. F. Gonthier, A. M. James, H. R. McAlexander, A. Kumar, M. Saitow, X. Wang, B. P. Pritchard, P. Verma, H. F. Schaefer, K. Patkowski, R. A. King, E. F. Valeev, F. A. Evangelista, J. M. Turney, T. D. Crawford and C. D. Sherrill, Psi4 1.1: An Open-Source Electronic Structure Program Emphasizing Automation, Advanced Libraries, and Interoperability, *J. Chem. Theory Comput.*, 2017, **13**, 3185–3197.

30 T. A. Keith, AIMALL, Version 17.11.14, TK Gristmill Software: Overland Park, KS, USA, 2016.

31 J. Contreras-García, E. R. Johnson, S. Keinan, R. Chaudret, J. P. Piquemal, D. N. Beratan and W. Yang, NCIPLOT: A program for plotting noncovalent interaction regions, *J. Chem.*

Theory Comput., 2011, **7**, 625–632.

32 E. Espinosa, E. Molins and C. Lecomte, Hydrogen bond strengths revealed by topological analyses of experimentally observed electron densities, *Chem. Phys. Lett.*, 1998, **285**, 170–173.

Chapter 4. Dramatic differences in the conformational equilibria of chalcogen- bridged compounds: The case of diallyl ether versus diallyl sulfide[1]

This chapter reports the rotational and computational study of diallyl ether (DAE) and diallyl sulfide (DAS). The study aims to address the lack of experimental data that describes the influence of the chalcogen atom on the molecular conformational landscape when the bridging atom is changed from oxygen to sulfur. The analysis reveals significant differences in the competitive nature of the conformational equilibria between DAE and DAS, which can be attributed to specific interactions involving the central bridge atom and neighboring side chains. Despite differences in the number of low energy conformers for DAE and DAS, the lowest energy conformer of each has the allyl groups in a similar orientation but with a smaller angle at the sulfur atom in the case of DAS which is consistent with greater p-character (less hybridization) at this atom.

4.1 Abstract

The conformational landscapes of diallyl ether (DAE) and diallyl sulfide (DAS) were investigated for the first time using rotational spectroscopy from 6–20 GHz supported by quantum mechanical calculations. A significant difference in the conformational distribution of these chalcogen-bridged compounds is predicted by theory at the B3LYP-D3(BJ)/aug-cc-pVTZ level as DAS has only one low energy conformer while DAE has up to 12 energy minima within 5 kJ mol-

[1] Content appearing in this chapter has been previously published as an article in the Journal of Physical Chemistry Chemical Physics under the citation: Poonia, T.; Silva, W.G.D.P.; van Wijngaarden, J. Dramatic differences in the conformational equilibria of chalcogen-bridged compounds: The case of diallyl ether versus diallyl sulfide, *Phys. Chem. Chem. Phys.*, 2022, 24, 240-248.

[1]. This was confirmed by rotational spectroscopy as only transitions corresponding to the global minimum of DAS were observed while the spectrum of DAE was much richer and composed of features from the nine lowest energy conformers. To understand the effects that govern the conformational preferences of DAE and DAS, natural bond orbital and non-covalent interaction analyses were done. These show that unique orbital interactions stabilize several conformers of the ether making its conformational landscape more competitive than that of the sulfide. This is consistent with a bonding model involving decreased hybridization of the bridging atom as one moves down the periodic table which is confirmed by the experimental ground state structures of the lowest energy forms of DAE and DAS, derived using spectra of the ^{13}C and ^{34}S substituted species in natural abundance.

4.2 Introduction

It is well-established that organic molecules can adopt different conformers by rotating about single bonds and that their tertiary structure is central to many chemical and biological processes. In most environments, it is difficult to isolate individual conformers and thus relate bulk properties to underlying molecular-level phenomena which leaves chemists to empirically screen many compounds for a desired reactivity. In this sense, modern rotational spectroscopy offers great promise in informing the design of new chemical processes as it allows the unambiguous identification of conformers that are isolated in a collision-free jet.[1–3] The conformer geometries, relative energies and dynamics extracted from a rotational spectrum provide deeper insights into the attractive and repulsive interactions that govern physical and chemical properties.[4–6]

While various allyl containing compounds are found to play an important role in processes in diverse fields such as medicine,[7] polymer science,[8] catalysis[9,10] and atmospheric chemistry,[11,12]

from a fundamental perspective, these species also serve as interesting test cases for conformational studies. This is due to the flexibility of the side chain and the presence of an unsaturated region (vinyl substituent) that can introduce additional stabilizing interactions compared with aliphatic side chains. The rich conformational landscape of allylic compounds was recently highlighted in microwave spectroscopic characterizations of molecules containing one (allyl isothiocynate,[13] allyl isocyanate[14] and allyl methyl amine[5]) and two allyl (diallyl amine[4] and diallyl disulfide[15]) moieties. For each, a highly molecule-specific balance of stereoelectronic effects (e.g. steric hindrance, orbital interactions, hydrogen bonding, etc.) was found to govern the observed conformational preferences. For the diallyl molecules in particular, the electronegative bridging group (NH in diallyl amine or the disulfide linkage in diallyl disulfide) plays a key directing role in the conformational equilibria giving rise to an unusually complex and non-intuitive distribution of conformer energies and shapes. This is seen, for example, by the significant differences in the conformational equilibria of diallyl amine (DAA)[4] and diallyl disulfide (DADS).[15] While DAA is smaller and has one fewer dihedral angle, its rotational spectrum contains transitions from four prominent conformers compared with the spectrum of DADS which features only one conformer.

The chalcogen-bridged analogs of the amine, diallyl ether (DAE) and diallyl sulfide (DAS), provide a more prescriptive case study of the role of the central atom on directing the conformational preferences as a function of its size and electronic properties. There are no prior rotational spectroscopic studies of either DAE or DAS, however, the latter has been investigated by theory and vibrational spectroscopy (liquid, solid and gas phase and Ar-matrix infrared, and Raman).[12,16] The vibrational spectrum of DAS suggests the presence of four stable conformers with the global minimum accounting for about 52% of the total conformational population. This

competition seems rather surprising in light of the results for the related disulfide (DADS) for which only one geometry was observed experimentally.[15] As chalcogen-substitution has received substantial attention in the materials science community[17] as a means to tune the optoelectronic properties of organic materials used in photovoltaics,[18] light emitting diodes[19] and sensors,[20] there is great value in deriving deeper understanding in the energy states of organochalcogens through detailed studies of their underlying potential energy surfaces.

Herein, we report the first investigation of the conformers of DAE and DAS using Fourier transform microwave (FTMW) spectroscopy supported by B3LYP-D3(BJ)/aug-cc-pVTZ predictions. A drastic reduction in the conformational competition was found when moving to the heavier organochalcogen with spectra attributable to nine unique conformers found for DAE and only one for DAS. To explain this surprising difference, we used natural bond orbital (NBO) and non-covalent interaction (NCI) analyses to characterize their electronic structures as a function of the bridging atom and to identify preferential orbital interactions that promote stability in conformers of the ether.

4.3 Methods

4.3.1 Experimental methods

DAS (97%, bp: 138ºC) and DAE (98%, bp: 94ºC) are commercially available from Sigma-Aldrich Canada and were used without further purification in this study. As both samples are liquid at room temperature, a gas mixture containing either ~1% of DAS or ~1% of DAE in neon (100-200 kPa) was prepared at room temperature. The gas mixture was then expanded into the high vacuum chamber of the spectrometers through a pulsed nozzle (1 mm diameter) resulting in a supersonic jet expansion. The rotational spectra of DAS and DAE were measured using both a

chirped-pulse (cp)[21] and a cavity-based Balle-Flygare (BF)[22] type Fourier transform microwave (FTMW) spectrometer, both of which have been described in detail previously.[23,24] A survey cp-FTMW spectrum was initially measured in 2 GHz segments from 8–18 GHz from which the most intense rotational transitions of the conformers were identified. Next, final frequency measurements were done using the BF-FTMW instrument from 6–20 GHz which features higher resolution and sensitivity. In the BF-FTMW instrument, due to the collinear arrangement of the molecular beam and the resonator axis, all rotational transitions recorded appear as two Doppler split components. In the cavity-based instrument, the transitions have line widths of ~7 kHz (FWHM) and the uncertainty in the measurement of line positions is typically ±2 kHz.

4.3.2 Computational methods

The presence of four dihedral angles ɣ, θ, δ and ∅ in the heavy atom backbones of DAS and DAE makes their conformational landscapes complex as different conformers may arise from internal rotations around these single bonds as shown in Figure 4.1. For both molecules, an automated conformational search was first carried out to identify potential conformers using the Conformer-Rotamer Ensemble Sampling Tool (CREST) at the GFN2-xTB[25] level of theory as available in the extended tight binding (xTB) program package.[26,27] The automated search led to 53 and 55 possible geometries for DAS and DAE, respectively. Next, all these 53 and 55 starting geometries were fully optimized using the dispersion-corrected density functional theory (DFT) B3LYP[28]-D3(BJ)[29,30] method with Dunning's aug-cc-pVTZ[31] basis set. Upon comparing the optimized DFT structures with those from CREST, it was noted that both methods predict similar global minimum geometries for DAE and DAS but different relative energy orderings of the remaining conformers. Vibrational frequency calculations within the harmonic approximation

were performed for all optimized geometries at the same level of theory to verify the nature of the stationary points and to obtain electronic energies with zero-point corrections (ZPE) and quartic centrifugal distortion constants. All optimization and frequency calculations were done using the Gaussian 16 software.[32] Natural bond orbital (NBO)[33] and non-covalent interaction (NCI)[34] calculations were carried out using the NBO 7.0[35] and NCIPLOT[36] programs, respectively, to investigate the stereoelectronic effects responsible for the observed conformational preferences.

4.4 Results

4.4.1 Conformational space of DAS and DAE

A surprisingly rich conformational equilibrium was predicted for DAS and DAE. The geometry optimization calculations identified 24 unique geometries of DAS within ~26 kJ mol^{-1} and 23 for DAE within 15 kJ mol^{-1}. Those found within 5 kJ mol^{-1} of the global minimum are shown in Figure 4.1 for DAS (one conformer) and DAE (12 conformers) while the energetic and spectroscopic parameters of all minima are given in Table 4.1. The Cartesian coordinates of the DAS and DAE conformers are provided in the electronic supporting information (ESI), file in Tables S1–S13 and the dihedral angles for all conformers are provided in Tables S14 and S15 (ESI). Roman numerals were used to label the conformers to reflect their stability ordering, based on the ΔE_0, with conformer I predicted to be the most stable.

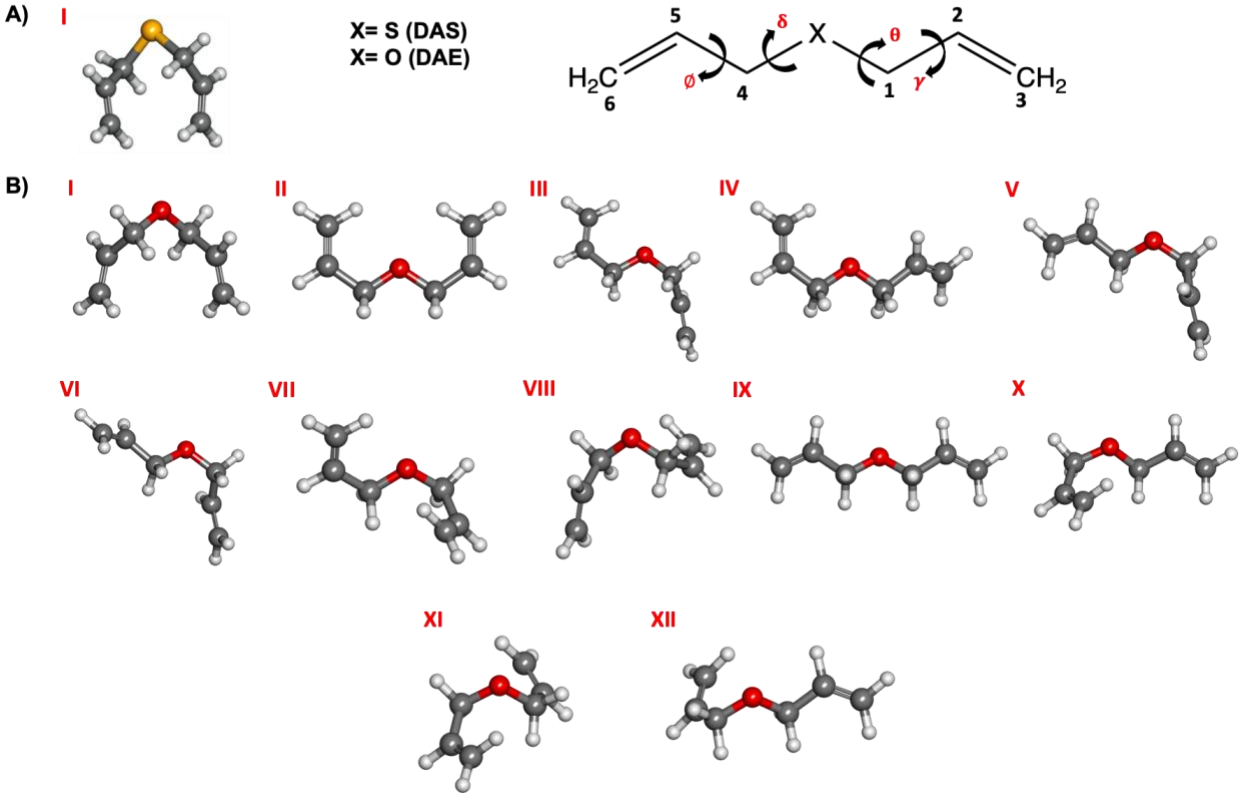

Figure 4.1 Lowest energy conformers of A) DAS and B) DAE that fall within 5 kJ mol^{-1} of the global minimum at the B3LYP-D3(BJ)/aug-cc-pVTZ level of theory.

Table 4.1 Calculated energetic and spectroscopic parameters for the conformers of DAS and DAE at the B3LYP-D3(BJ)/aug-cc-pVTZ level of theory.

DAS	ΔE_e[a]	ΔE_0[b]	P[c]	A/B/C[d]	$\lvert\mu_a\rvert/\lvert\mu_b\rvert/\lvert\mu_c\rvert$[e]
I	0.00	0.00	83.0	2449/1781/1186	0.0/1.2/0.0
II	7.06	6.58	4.8	2833/1545/1257	0.4/1.3/0.2
III	7.80	7.11	3.6	3215/1310/1044	0.4/1.3/0.1
IV	8.22	7.57	3.0	4192/1083/924	0.7/1.1/0.6
V	9.28	8.42	2.0	3949/1106/932	0.6/1.0/0.7
VI	10.04	9.27	1.4	2925/1420/1049	0.7/1.0/0.7
VII	12.42	11.34	0.6	2272/1938/1151	0.1/1.1/0.6
VIII	13.99	12.82	0.3	4397/1133/973	0.9/1.1/0.6
IX	14.22	13.13	0.3	2534/1745/1265	0.6/1.0/0.9
X	15.69	14.55	0.1	4486/1098/977	0.6/0.5/1.4
XI	16.02	14.84	0.1	4187/1125/980	0.5/0.4/1.4
XII	16.27	14.94	0.1	10163/775/765	0.0/1.6/0.1
XIII	16.37	15.04	0.1	10484/775/764	0.0/1.6/0.0
XIV	16.25	15.07	0.1	5626/912/849	0.3/0.8/1.2
XV	16.21	15.15	0.1	3659/1268/1245	0.0/1.4/0.0
XVI	16.55	15.39	0.1	4129/1118/1058	0.2/1.3/0.7
XVII	16.96	15.61	0.1	6600/874/832	0.2/0.9/1.1
XVII	17.47	16.52	0.1	4396/1056/950	0.0/1.4/0.0

XIX	17.95	16.82	0.1	2860/1532/1139	0.1/0.5/1.4
XX	18.23	17.02	0.1	3408/1191/964	0.3/0.7/1.3
XXI	20.56	19.12	0.0	4220/1182/1076	0.8/0.5/1.4
XXII	21.38	19.65	0.0	8387/860/809	0.1/1.7/0.0
XXIII	21.89	20.22	0.0	6238/935/889	0.5/1.3/0.9
XXIV	26.06	23.98	0.0	6829/974/861	0.0/1.9/0.0

DAE	ΔE_e[a]	ΔE_0[b]	P[c]	A/B/C[d]	$\lvert\mu_a\rvert$/ $\lvert\mu_b\rvert$/ $\lvert\mu_c\rvert$[e]
I	0.00	0.00	15.8	3784/1817/1396	0.0/1.2/0.0
II	2.01	0.42	13.3	5842/1379/1131	0.0/1.6/0.0
III	1.70	0.75	11.6	7505/1208/1129	1.1/0.9/0.5
IV	3.27	1.59	8.3	8059/1104/1010	0.3/1.3/0.0
V	2.78	1.76	7.7	6276/1198/1078	0.6/0.7/0.7
VI	3.03	1.95	7.2	7493/1125/1055	0.7/0.9/0.4
VII	2.84	2.16	6.6	5214/1501/1352	0.7/0.6/1.1
VIII	2.65	2.39	6.0	5204/1422/1380	0.5/1.1/0.2
IX	4.61	2.73	5.2	11535/932/924	0.0/1.1/0.4
X	4.48	3.61	3.7	5328/1421/1198	0.3/0.2/1.2
XI	4.24	3.84	3.3	6726/14191290	0.0/0.0/1.3
XII	5.18	4.20	2.9	6730/1270/1140	0.4/0.2/1.2
XIII	6.37	5.67	1.6	3941/1780/1510	0.8/0.5/1.0

XIV	7.10	6.46	1.2	6041/1267/1164	0.5/1.2/0.1
XV	7.93	6.69	1.1	8112/1112/1087	0.7/1.3/0.1
XVI	7.90	6.84	1.0	3379/2041/1411	0.1/0.9/0.6
XVII	7.43	6.90	1.0	4524/1533/1255	0.6/0.8/0.8
XVII	8.79	7.48	0.8	8192/1062/998	0.3/0.2/1.2
XIX	9.47	8.02	0.6	11167/994/973	0.3/0.3/1.2
XX	8.92	8.08	0.6	7714/1220/1144	0.0/0.2/1.3
XXI	9.70	8.97	0.4	4136/1781/1382	0.2/0.1/1.3
XXII	13.85	12.61	0.1	1187/1011/1000	0.0/0.0/1.3
XXIII	15.34	14.99	0.0	7732/1176/1134	0.0/1.3/0.0

[a]Relative total electronic energy in kJ mol^{-1}, [b]Zero-point energy (ZPE) corrected relative total energies in kJ mol^{-1}, [c]Boltzmann population at 298K in %. These populations do not account for the degeneracy of the conformers due to symmetry (see text), [d]Rotational constants in MHz, [e]Magnitude of the electric dipole moment components in Debye.

4.4.2 Spectral analysis

As the rotational spectra of DAS and DAE have not been previously reported, the calculated parameters from Table 4.1 were used as guides for the spectral analysis. Preliminary assignment of the observed patterns in the cp-FTMW spectra identified the lowest energy conformer for DAS and the first nine conformers for DAE (I-IX) in Figure 4.1. Figure 4.2 shows a region of the cp-FTMW spectrum of DAE featuring transitions for these nine assigned conformers to demonstrate the spectral complexity. For the lowest energy forms of DAS and DAE, the spectral intensity was sufficient to allow transitions from singly-substituted minor isotopologues to be observed in natural abundance. These include transitions for the three unique ^{13}C isotopologues of each as well as the ^{34}S isotopologue for DAS. For conformer I of DAE and

DAS, the relative intensity of the ^{13}C transitions were ~2% that of the parent lines due to symmetry which yields two equivalent sites for each carbon atom. Following preliminary assignment of the patterns from the broadband spectrum, the observed transitions for all conformers were re-measured using the higher resolution BF-FTMW instrument and additional lower intensity features were measured to expand the data set. Although the rotational constants and dipole components (Table 4.1) were good guides for the spectral assignments, the intensities of the observed transitions for DAE were not fully consistent with the predicted populations in Table 4.1. For a better reproduction of the experimental intensities, the symmetry and resulting degeneracies of the conformers were considered. For example, conformer I of DAE has C_2 symmetry with two equivalent minima, while conformer II with C_{2v} symmetry exists as a single geometry. On the other hand, conformer III has C_1 symmetry which leads to four equivalent conformations. Once the symmetry of all assigned conformers of DAE is considered, the calculated populations are: I: 15.5%, II: 6.5%, III: 22.9%, IV: 16.4%, V: 7.6%, VI: 7.1%, VII: 13.0%, VIII: 5.9%, IX: 5.1% rather than the values given in Table 4.1. The new values are consistent with the observed spectral intensities.

The transition frequencies of each species from the BF-FTMW measurements were least-squared fit with Pickett's SPFIT program[37] using Watson's A-reduced Hamiltonian[38] in the I^r representation to obtain experimental rotational and quartic centrifugal distortion constants which are summarized in Tables 4.2–4.4. Line lists containing all assigned rotational transitions and their residuals are given in Tables S18–S34 of the ESI. Despite careful searches, transitions attributable to higher energy conformers of DAS and DAE were not observed.

Table 4.2 Ground State Spectroscopic Constants of DAS Conformer-I Including Its ^{13}C and ^{34}S Isotopologues.

Parameter	I	$^{13}C1$	$^{13}C2$	$^{13}C3$	^{34}S
A/MHz[a]	2447.825367(51)	2438.40000(15)	2445.98277(11)	2414.296667(93)	2394.45055(14)
B/MHz	1783.279427(47)	1771.27288(26)	1759.05341(17)	1758.70686(14)	1783.30467(15)
C/MHz	1180.778463(45)	1177.021037(77)	1169.802141(59)	1162.645711(50)	1168.200759(62)
Δ_J/kHz[b]	1.67263(47)	1.6344(41)	1.6250(21)	1.6495(19)	1.6625(21)
Δ_{JK}/kHz	-4.6702(10)	-4.505(14)	-4.5602(74)	-4.5739(63)	-4.6773(89)
Δ_K/kHz	5.4083(12)	5.223(15)	5.3600(58)	5.2663(50)	5.3463(70)
δ_J/kHz	0.70110(16)	0.6838(20)	0.6794(10)	0.69231(92)	0.7030(10)
δ_K/kHz	0.70125(51)	0.7187(73)	0.7086(40)	0.7064(27)	0.6078(37)
$\mu_a/\mu_b/\mu_c$[c]	n/y/n	n/y/n	n/y/n	n/y/n	n/y/n
J'[d]	2–10	2–8	2–8	2–8	2–8
N[e]	87	35	37	37	37
σ/kHz[f]	1.0	1.1	0.9	0.8	0.9

[a]Rotational constants; [b]quartic centrifugal distortion constants; [c]electric dipole moment components ("y" if observed and "n" if not observed); [d]range of observed rotational quantum number for the upper state (J'); [e]total number of lines (N) in the fit; [f]root-mean-square deviation of the fit (σ). A complete list of the calculated rotational parameters at the B3LYP-D3(BJ)/aug-cc-pVTZ is provided in Table S16 (ESI).

Table 4.3 Ground State Spectroscopic Constants of DAE Conformer-I Including Its ^{13}C Isotopologues.

Parameter	Conformer I	$^{13}C1$	$^{13}C2$	$^{13}C3$
A/MHz[a]	3783.26132(19)	3756.61996(76)	3782.29381(82)	3731.21601(66)
B/MHz	1815.02675(18)	1806.04406(39)	1791.78164(49)	1786.36659(38)
C/MHz	1392.94239(14)	1387.99557(33)	1379.30819(38)	1369.12820(29)
Δ_J/kHz[b]	3.7222(22)	3.6924(56)	3.6918(65)	3.7003(50)
Δ_{JK}/kHz	-17.7190(49)	-17.563(56)	-17.555(58)	-17.527(46)
Δ_K/kHz	29.3613(93)	28.98(11)	29.21(11)	28.703(92)
δ_J/kHz	1.34698(82)	[1.34698]	[1.34698]	[1.34698]
δ_K/kHz	3.2401(88)	[3.2401]	[3.2401]	[3.2401]
$\mu_a/\mu_b/\mu_c$[c]	n/y/n	n/y/n	n/y/n	n/y/n
J'[d]	2–9	2–6	2–6	2–6
N[e]	46	16	14	15
σ/kHz[f]	1.6	2.3	2.2	1.8

[a]Rotational constants; [b]quartic centrifugal distortion constants; [c]electric dipole moment components ("y" if observed and "n" if not observed); [d]range of observed rotational quantum number for the upper state (J'); [e]total number of lines (N) in the fit; [f]root-mean-square deviation of the fit (σ). Values in brackets were fixed to those determined for the parent species. A complete list of the calculated rotational parameters at the B3LYP-D3(BJ)/aug-cc-pVTZ is provided in Table S17 (ESI).

Table 4.4 Ground State Spectroscopic Constants Conformers II to IX of DAE.

Parameter	II	III	IV	V	VI	VII	VIII	IX
A/MHz[a]	5778.39751(83)	7474.59182(36)	7983.34964(53)	6196.70156(13)	7433.27031(24)	5196.26139(43)	5268.65716(22)	11414.02484(47)
B/MHz	1392.06750(11)	1214.02905(52)	1110.32576(76)	1208.265554(39)	1129.15749(33)	1511.415694(91)	1415.96699(26)	934.64344(26)
C/MHz	1139.27067(14)	1133.29913(52)	1015.20606(74)	1083.339960(48)	1057.78776(32)	1359.856187(94)	1378.23179(26)	926.73986(26)
Δ_J/kHz[b]	0.25929(93)	0.40733(98)	0.1835(14)	0.50571(27)	0.26314(53)	1.81536(76)	1.13564(90)	0.1490(66)
Δ_{JK}/kHz	-1.4672(72)	-10.9365(62)	-5.2452(93)	-9.0581(18)	-4.7302(33)	-14.1707(54)	-12.9628(30)	-14.5608(83)
Δ_K/kHz	7.93(18)	[162.9582]	21.01(14)	77.203(13)	[71.538104]	55.543(87)	55.693(20)	[535.86204]
δ_J/kHz	0.06735(44)	0.00922(55)	0.02392(28)	0.11361(14)	0.05348(17)	0.53599(48)	0.17603(51)	0.01438(19)
δ_K/kHz	0.835(23)	4.57(26)	-1.02(37)	1.365(10)	0.42(16)	4.892(31)	-3.61(12)	[-6.4307101]
$\mu_a/\mu_b/\mu_c$[c]	n/y/n	y/y/y	y/y/n	y/y/y	y/y/y	y/y/y	y/y/y	n/y/y
J'[d]	1–10	1–9	1–11	1–11	1–11	1–9	1–9	1–11
N[e]	30	67	40	110	74	71	67	28
σ/kHz[f]	1.5	1.5	1.1	1.1	1.0	1.3	1.4	1.5

[a]Rotational constants; [b]quartic centrifugal distortion constants; [c]electric dipole moment components ("y" if observed and "n" if not observed); [d]range of observed rotational quantum number for the upper state (J'); [e]total number of lines (N) in the fit; [f]root-mean-square deviation of the fit (σ). Values in brackets were fixed to the predicted values obtained at the B3LYP-D3(BJ)/aug-cc-pVTZ level of theory. A complete list of the calculated rotational parameters at the B3LYP-D3(BJ)/aug-cc-pVTZ is provided in Table S17 (ESI).

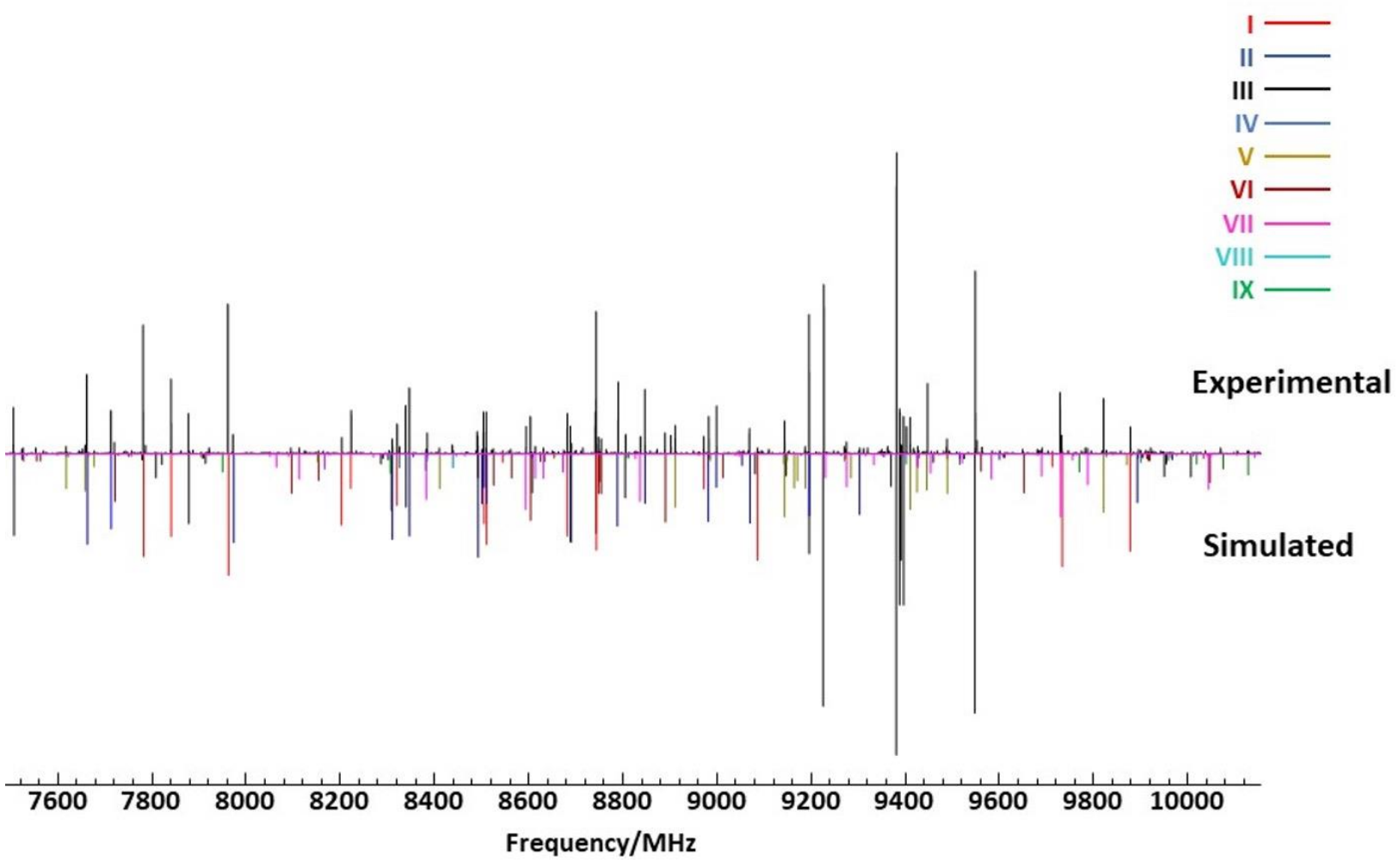

Figure 4.2 Portion of the broadband cp-FTMW spectrum (average of 1.5 million free induction decays) of DAE showing rotational transitions observed for the nine lowest energy conformers. The top portion is the experimental spectrum and the lower is the simulated spectrum using the fitted parameters from Table 4.3 and Table 4.4. Intensities are dependent on the calculated dipole moment components and the relative populations from Table 4.1.

4.4.3 Structural determination

With the measurement of the spectra of minor isotopic species for conformer I of both compounds, the geometries of the heavy atom skeletons were determined using the complete sets of experimental rotational constants from Tables 4.2 and 4.3 for DAS and DAE, respectively. Accounting for symmetry, the atomic coordinates of the substituted atoms and their Costain[39] errors were estimated by solving Kraitchman's equations[40] as implemented in Kisiel's KRA program.[41] These are summarized in Table S35 of the ESI. The signs of the coordinates were inferred by comparison with the computational geometries and the imaginary c-coordinate for sulfur in the case of DAS was set to zero in the subsequent analysis as it lies in the ab-plane of the molecule. The resulting sets of coordinates were used to estimate the internal geometric parameters involving the heavy atoms using the EVAL program[41] which are summarized in Tables 4.5 and 4.6 for DAS and DAE, respectively, under the r_s headings. Overall, fewer structural elements were determined for DAE due to absence of ^{18}O data and the uncertainty in the derived bond lengths is about three times larger than in the sulfur containing analog. This is likely a consequence of the relatively large Costain error in the position of C2 (Figure 4.1) in DAE which lies only 0.065(23) Å from the ac-plane.

The ground state effective geometries, r_0, of DAS and DAE were then derived using Kisiel's STRFIT program[41] to fit the effective moments of inertia to a set of internal parameters. This procedure was carried out by fixing the equilibrium internal coordinates of hydrogen atoms to those derived at the B3LYP-D3(BJ)/aug-cc-pVTZ level of theory. Accounting for symmetry, there are eight internal parameters needed to define the arrangement of the allyl side chains (three bond lengths, three angles and two dihedral angles) relative to the central atom. With 15 rotational constants determined from fitting transitions arising from five isotopologues of DAS, all eight

structural parameters were well-determined and these are listed in Table 4.5. For DAE, with data from one fewer isotopologue, several combinations of parameters were considered as the fit was not particularly sensitive to the C–O bond length. In the end, six structural parameters were determined for DAE in the fit after keeping the C–O bond length and the C–C–C–O dihedral angle fixed at the computed values. The results are provided in Table 4.6. Overall, the derived r_0 parameters are an excellent model of the geometries as this procedure successfully reproduced the experimental rotational constants of conformer I of DAS and DAE to within 0.004% and 0.013% or better.

Table 4.5 Equilibrium (r_e) (B3LYP-D3(BJ)/aug-cc-pVTZ), Substitution (r_s), and Ground State Effective (r_0) Structural Parameters (Bond Lengths in Å, Angles in deg) Determined for DAS.

	r_e	r_s	r_0
S-C1	1.838	1.823(3)	1.826(5)
C1-C2	1.490	1.489(7)	1.490(10)
C2-C3	1.328	1.347(4)	1.349(9)
∠C4-S-C1	100.1	99.3(2)	99.6 (3)
∠ S-C1-C2	112.1	111.9(3)	111.9(6)
∠C1-C2-C3	124.3	122.5(5)	122.6(13)
∠C2-C1-S-C4	68.7	69.5(2)	69.4(4)
∠C3-C2-C1-S	-115.5	-119.4(6)	-119.0(15)

Table 4.6 Equilibrium (r_e) (B3LYP-D3(BJ)/aug-cc-pVTZ), Substitution (r_s), Ground State Effective (r_0) Structural Parameters (Bond Lengths in Å, Angles in deg) Determined for DAE.

	r_e	r_s	r_0
C1-C2	1.499	1.507(12)	1.487(8)
C2-C3	1.326	1.340(23)	1.309(17)

∠C1-O-C4	114.2	-	113.8(6)
∠C2-C1-O	112.6	-	113.0(3)
∠C1-C2-C3	124.2	122.6(10)	125.1(9)
∠C2-C1-O-C4	-69.1	-	-69.4(5)

4.5 Discussion

The surprising differences in the conformational landscapes of DAS and DAE, both in terms of the conformer geometries and relative energies predicted by DFT calculations, are confirmed by the FTMW measurements. The ground state spectroscopic constants obtained from fitting the experimental spectrum of both molecules are well-determined and in good agreement with the calculated values for conformer I of DAS and conformers I through IX of DAE at the B3LYP-(D3)BJ/aug-cc-pVTZ level of theory shown in Tables 4.1–4.4. Although additional conformers for both molecules are populated at 298K (Table 4.1), the absence of features from higher energy structures in the rotational spectrum may be justified by insufficient population in the supersonic jet which is likely exacerbated by conformational cooling. This process allows higher energy conformers to interconvert to lower energy forms through collisions with the carrier gas at the beginning of the expansion. For small molecules and complexes, interconversion barriers less than ~5 kJ mol^{-1} are known to allow for relaxation in the molecular beam.[42] Modelling the interconversion pathways for the conformer relaxation of DAE and DAS is complex as it requires simultaneous changes for up to four dihedral angles, but the observation of nine conformers for DAE affirms that relaxation involving movement of the heavy alkyl chains is not facile. In general, for both DAS and DAE, conformers with relative energies within 3 kJ mol^{-1} of the global minimum

were observed, which is coincidentally the same energy cut-off reported in a previous microwave study of the related diallyl amine (DAA) compound.[4]

Based on the relative energies from Table 4.1 and the number of species identified in the supersonic jet for DAS and DAE, it is evident that the conformational landscape of DAE is highly competitive compared to that of DAS. Interestingly, although conformational changes upon replacing oxygen with sulfur in organic molecules were predicted from theoretical studies of a series of analogs of alcohols, thiols, ethers and sulfides,[43] with the oxygen compounds showing a more competitive equilibrium, these large differences in conformational equilibria have not been widely explored spectroscopically. This makes DAE and DAS excellent prototypes to test whether these phenomena are observed experimentally. By analyzing the geometries corresponding to the minima of DAE and DAS (Figure 4.1), it is readily apparent that many of the low energy conformers of DAE have one or both vinyl groups in the plane of the (C–X–C) link and pointed up (dihedral angles ϕ and γ = 0º), such as in conformer II in which the orientation of the allyl moieties form a "W-shaped" structure. The analogous geometries are not stable in DAS or are much higher in energy which provides an important clue towards understanding why the conformational distribution is so unique for these two organochalcogens.

According to NBO calculations, this marked difference in conformational stability can be rationalized in terms of orbital interactions through their second order perturbation energies. Conformers of DAE with a W-shaped or with a V-shaped side chain (only one allyl group pointing up, e.g. conformer III) favour $LP_1(O) \rightarrow \sigma^*_{C–C}$ orbital interactions involving donation from the lone pair LP_1 on oxygen to the antibonding σ* orbital of the neighbouring C1–C2 and/or C4–C5 bond, whereas in the DAS analogs, these hyperconjugative interactions are largely absent. This is illustrated in Figure 4.3 and Table S36 (ESI) using the NBO results for conformer II of DAE and

conformer XXIV of DAS, which have comparable dihedral angles. The greater stabilizing orbital interactions in the DAE geometries are possible because of better overlap between the donor and acceptor orbitals compared with that in the heavier congener. The enhanced orbital interactions in the ether are responsible for its competitive conformational landscape. A similar observation was noted for oxygen *versus* sulfur compounds in the case of 1-butanol and 1-butanethiol and for *iso*-butanol and *iso*-butanethiol[44] in which the alcohols exhibited LP(O)→σ^*_{C-H} and LP(O)→σ^*_{C-C} interactions and the thiols did not. The increased favourability of orbital interactions is also consistent with the natural charges on oxygen (-0.56) and sulfur (+0.19) from conformer I in DAE and DAS, respectively, as expected based on their relative intrinsic electronegativities. These results are illustrative of how sensitive molecular potential energy surfaces are to subtle changes in non-covalent interactions as one moves down the periodic table and how this gives rise to measurable differences in molecular properties such as structure.

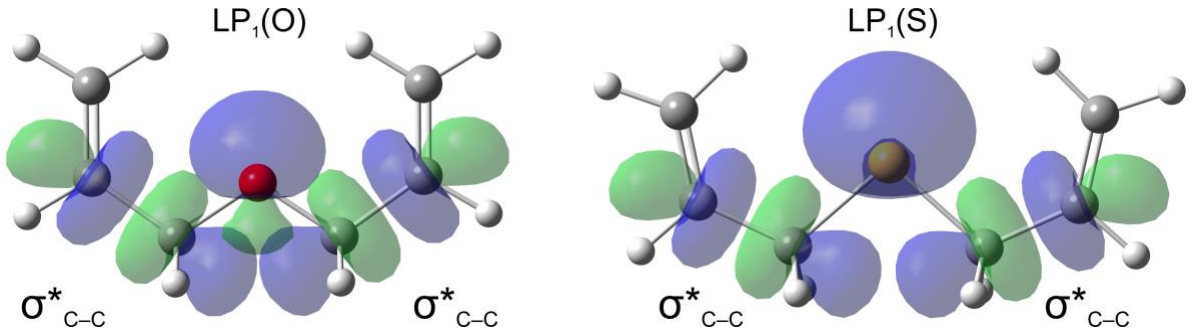

Figure 4.3 NBO plots for conformers II of DAE (left) and XXIV of DAS (right) showing the $LP_1(X)$ and σ^*_{C-C} orbitals.

Although the richness of the conformational distributions of DAE and DAS are surprisingly different, the orientation of the two allyl groups in the lowest energy structure of each is somewhat similar as seen in Figure 4.1. Upon closer inspection of the geometric parameters in

Tables 4.5 and 4.6, the most notable difference is that the bridging angle C–S–C is ~14º smaller than the corresponding C–O–C angle which brings the allyl groups closer to each other in DAS. This is consistent with the hybridization of the central atoms from the NBO calculations with the sulfide C–S bonding orbitals showing larger p-character on sulfur (84.8% for both) compared to those on oxygen (72.5%-78.7%) in DAE. This confirms that hybridization models of bonding used to understand molecular geometry around lighter elements (O) cannot be extrapolated to heavier analogs (S).

To further investigate the origin of the high stability of conformers I of DAE and DAS, we carried out NCI analysis. While one might think that conformer I is favoured by interactions between the two allyl groups as this is the main effect governing the stability of other allyl containing molecules such as diallyl disulfide (DADS)[15] and from the structures shown in Figure 4.1, no strong interactions (represented by blue-coloured isosurfaces) are found in the NCI graphs (Figure 4.4). Rather, a green-coloured surface indicative of a weak contact (either attractive or repulsive) is present suggesting that interactions between the allyl groups are not a substantial stabilizing effect. Indeed, based on the NBO output, neither conformer I of DAE nor DAS show charge transfer between the two allyl groups. Instead, this arrangement of the two allyl fragments appears to optimize other charge transfer interactions (summarized in Table S36, ESI), including electron donation from the lone pair on the bridge atom $LP_2(S)/LP_2(O)$ to the antibonding π^* orbitals of the C=C bonds of both allyl side chains and thus stabilizes conformer I relative to others.

The dramatic differences in the conformational equilibria of DAE and DAS through the observed species and their geometries reinforces the fact that even substitution of heteroatoms within a group can completely alter the properties of an organic compound in impactful ways. Although bonding among p-block elements is of critical importance in most branches of chemistry,

chemical intuition does not seamlessly extend to molecules with rich conformational landscapes as subtle changes in non-covalent interactions are sufficient to completely alter the relative energies of competing structures. This unexpected conformational complexity is surprising in DAE and DAS as the side chains are small, and thus, the identity of the center atom controls the conformer distribution rather than interactions between the side chains.

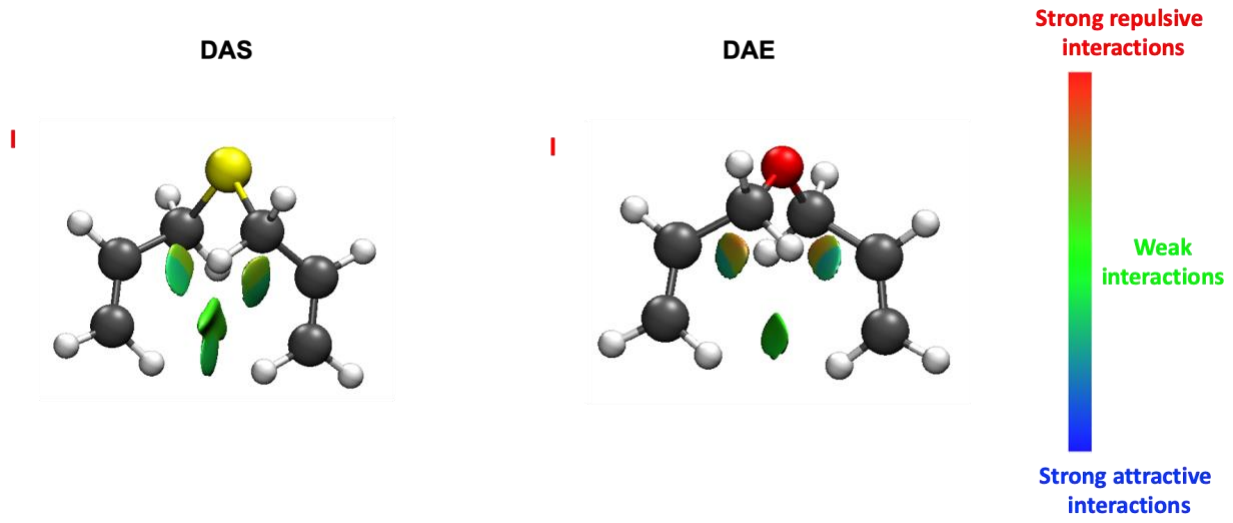

Figure 4.4 NCI isosurfaces (s = 0.05, color scale for -0.02 < ρ < + 0.02 au) for conformer I of DAS and DAE respectively.

4.6 Conclusions

Using quantum chemical calculations and rotational spectroscopy, the conformational landscapes of DAE and DAS were investigated for the first time. The results revealed a dramatic conformational change upon replacing the central bridging atom from oxygen to sulfur with the ether existing as a rich conformational mixture. This was confirmed by FTMW spectra from which transitions were assigned for nine stable conformers of DAE but for only one of DAS. A NBO analysis contributed new physical insights by identifying unique orbital interactions involving one

lone pair on oxygen that stabilize specific geometries of DAE. By comparison, these interactions are absent in DAS because the lone pairs on sulfur do not adopt a favourable spatial arrangement. The larger p-character on S is consistent with less hybridization in the bonding between sulfur and carbon which is also manifested in the C–X–C angle of DAS which is 14º smaller than that of the ether. The surprising conformational differences of DAE and DAS highlight that the electronic properties of the bridging atom have a dramatic effect on the arrangement of the organic side chains. This re-affirms that models of bonding, dynamics and reactivity based on carbon and its neighbours cannot be automatically extrapolated as one moves down the periodic table. Our results lay the foundation for the development of improved models of chemical bonding, dynamics and reactivity in organochalcogens for better design of main group and organometallic compounds.

4.7 References

1 S. R. Domingos, C. Pérez, C. Medcraft, P. Pinacho and M. Schnell, Flexibility unleashed in acyclic monoterpenes: Conformational space of citronellal revealed by broadband rotational spectroscopy, *Phys. Chem. Chem. Phys.*, 2016, **18**, 16682–16689.

2 F. Xie, N. A. Seifert, M. Heger, J. Thomas, W. Jäger and Y. Xu, The rich conformational landscape of perillyl alcohol revealed by broadband rotational spectroscopy and theoretical modelling, *Phys. Chem. Chem. Phys.*, 2019, **21**, 15408–15416.

3 S. I. Murugachandran, J. Tang, I. Peña, D. Loru and M. E. Sanz, New Insights into Secondary Organic Aerosol Formation: Water Binding to Limonene, *J. Phys. Chem. Lett.*, 2021, **12**, 1081–1086.

4 W. G. D. P. Silva, G. Daudet, S. Perez, S. Thorwirth and J. van Wijngaarden, Conformational preferences of diallylamine: A rotational spectroscopic and theoretical

study, *J. Chem. Phys.*, 2021, **154**, 1–25.

5 W. G. D. P. Silva, T. Poonia and J. van Wijngaarden, Targeting the Rich Conformational Landscape of N-Allylmethylamine Using Rotational Spectroscopy and Quantum Mechanical Calculations, *ChemPhysChem*, 2020, **21**, 2515–2522.

6 W. G. D. P. Silva, T. Poonia and J. van Wijngaarden, Exploring the non-covalent interactions behind the formation of amine-water complexes: The case of N-allylmethylamine monohydrate, *Phys. Chem. Chem. Phys.*, 2021, **23**, 7368–7375.

7 K. C. Lai, C. L. Kuo, H. C. Ho, J. S. Yang, C. Y. Ma, H. F. Lu, H. Y. Huang, F. S. Chueh, C. C. Yu and J. G. Chung, Diallyl sulfide, diallyl disulfide and diallyl trisulfide affect drug resistant gene expression in colo 205 human colon cancer cells in vitro and in vivo, *Phytomedicine*, 2012, **19**, 625–630.

8 Z. Jian and S. Mecking, Insertion Homo- and Copolymerization of Diallyl Ether, *Angew. Chemie - Int. Ed.*, 2015, **54**, 15845–15849.

9 P. Wu, Y. Liu, M. He and T. Tatsumi, A novel titanosilicate with MWW structure Catalytic properties in selective epoxidation of diallyl ether with hydrogen peroxide, *J. Catal.*, 2004, **228**, 183–191.

10 K. H. Dragnev, R. W. Nims and R. A. Lubet, The chemopreventive agent diallyl sulfide, *Biochem. Pharmacol.*, 1995, **50**, 2099–2104.

11 A. R. Oliaey, A. Shiroudi, E. Zahedi and M. S. Deleuze, Theoretical study on the elimination kinetics in the gas phase of allyl methyl compounds, *Monatshefte fur Chemie*, 2018, **149**, 1389–1400.

12 B. E. Arango Hoyos and R. M. Romano, Experimental and theoretical conformational studies on diallyl sulfide, *J. Mol. Struct.*, 2019, **1182**, 54–62.

13 J. Stitsky, W. G. D. P. Silva, W. Sun and J. Van Wijngaarden, Conformers of Allyl Isothiocyanate: A Combined Microwave Spectroscopy and Computational Study, *J. Phys. Chem. A*, 2020, **124**, 3876–3885.

14 W. Sun, O. P. Sogeke, W. G. D. P. Silva and J. Van Wijngaarden, Dispersion-driven conformational preference in the gas phase: Microwave spectroscopic and theoretical study of allyl isocyanate, *J. Chem. Phys.*, 2019, **151,** 194304.

15 J. Demaison, N. Vogt, R. T. Saragi, M. Juanes, H. D. Rudolph and A. Lesarri, How flexible is the disulfide linker? A combined rotational-computational investigation of diallyl disulfide, *Phys. Chem. Chem. Phys.*, 2019, **21**, 19732–19736.

16 M. T. Devlin, V. F. Kalasinsky and I. W. Levin, Solid and liquid phase Raman and infrared spectra of diallyl sulfide and diallyl disulfide, *J. Mol. Struct.*, 1989, **213**, 35–50.

17 G. C. Hoover and D. S. Seferos, Photoactivity and optical applications of organic materials containing selenium and tellurium, *Chem. Sci.*, 2019, **10**, 9182–9188.

18 J. G. Manion, J. R. Panchuk and D. S. Seferos, Applying Heteroatom Substitution in Organic Photovoltaics, *Chem. Rec.*, 2019, **19**, 1113–1122.

19 T. Gneuß, M. J. Leitl, L. H. Finger, N. Rau, H. Yersin and J. Sundermeyer, A new class of luminescent Cu(i) complexes with tripodal ligands-TADF emitters for the yellow to red color range, *Dalt. Trans.*, 2015, **44**, 8506–8520.

20 Z. Lou, P. Li and K. Han, Redox-responsive fluorescent probes with different design strategies, *Acc. Chem. Res.*, 2015, **48**, 1358–1368.

21 G. G. Brown, B. C. Dian, K. O. Douglass, S. M. Geyer and B. H. Pate, The rotational spectrum of epifluorohydrin measured by chirped-pulse Fourier transform microwave spectroscopy, *J. Mol. Spectrosc.*, 2006, **238**, 200–212.

22 T. J. Balle and W. H. Flygare, Fabry-Perot cavity pulsed Fourier transform microwave spectrometer with a pulsed nozzle particle source, *Rev. Sci. Instrum.*, 1981, **52**, 33–45.

23 L. Evangelisti, G. Sedo and J. van Wijngaarden, Rotational Spectrum of 1,1,1-Trifluoro-2-butanone Using Chirped-Pulse Fourier Transform Microwave Spectroscopy, *J. Phys. Chem. A*, 2011, **115**, 685–690.

24 G. Sedo and J. van Wijngaarden, Fourier transform microwave spectra of a "new" isomer of OCS-CO_2, *J. Chem. Phys.*, 2009, **131**, 044303.

25 C. Bannwarth, S. Ehlert and S. Grimme, GFN2-xTB - An Accurate and Broadly Parametrized Self-Consistent Tight-Binding Quantum Chemical Method with Multipole Electrostatics and Density-Dependent Dispersion Contributions, *J. Chem. Theory Comput.*, 2019, **15**, 1652–1671.

26 S. Grimme, Exploration of Chemical Compound, Conformer, and Reaction Space with Meta-Dynamics Simulations Based on Tight-Binding Quantum Chemical Calculations, *J. Chem. Theory Comput.*, 2019, **15**, 2847–2862.

27 P. Pracht, F. Bohle and S. Grimme, Automated exploration of the low-energy chemical space with fast quantum chemical methods, *Phys. Chem. Chem. Phys.*, 2020, **22**, 7169–7192.

28 A. D. Becke, A new inhomogeneity parameter in density-functional theory, *J. Chem. Phys.*, 1998, **109**, 2092–2098.

29 S. Grimme, S. Ehrlich and L. Goerigk, Effect of the damping function in dispersion corrected density functional theory, *J. Comput. Chem.*, 2011, **32**, 1456–1465.

30 S. Grimme, J. Antony, S. Ehrlich and H. Krieg, A consistent and accurate ab initio parametrization of density functional dispersion correction (DFT-D) for the 94 elements H-

Pu, *J. Chem. Phys.*, 2010, **132**, 1–19.

31 T. H. Dunning, Gaussian basis sets for use in correlated molecular calculations. I. The atoms boron through neon and hydrogen, *J. Chem. Phys.*, 1989, **90**, 1007–1023.

32 M. J. Frisch, G. W. Trucks, H. B. Schlegel, G. E. Scuseria, M. A. Robb, J. R. Cheeseman, G. Scalmani, V. Barone, B. Mennucci, G. A. Petersson, H. Nakatsuji, M. Caricato, X. Li, H. P. Hratchian, A. F. Izmaylov, J. Bloino, G. Zheng, J. L. Sonnenberg, M. Hada, M. Ehara, Fukuda, K. T. R., J. Hasegawa, M. Ishida, T. Nakajima, Y. Honda, O. Kitao, H. Nakai, T. Vreven, J. A. Montgomery, J. E. Peralta, F. Ogliaro, M. Bearpark, J. J. Heyd, E. Brothers, K. N. Kudin, V. N. Staroverov, R. Kobayashi, J. Normand, K. Raghavachari, A. Rendell, J. C. Burant, S. S. Iyengar, J. Tomasi, M. Cossi, N. Rega, J. M. Millam, M. Klene, J. E. Knox, J. B. Cross, V. Bakken, C. Adamo, J. Jaramillo, R. Gomperts, R. E. Stratmann, O. Yazyev, A. J. Austin, R. Cammi, C. Pomelli, J. W. Ochterski, R. L. Martin, K. Morokuma, V. G. Zakrzewski, G. A. Voth, P. Salvador, J. J. Dannenberg, S. Dapprich, A. D. Daniels, Farkas, J. B. Foresman, J. V Ortiz, J. Cioslowski and D. J. Fox, Gaussian 16 (Revision C.01), Gaussian, Inc., Wallingford CT, 2016.

33 F. Weinhold, C. R. Landis and E. D. Glendening, What is NBO analysis and how is it useful?, *Int. Rev. Phys. Chem.*, 2016, **35**, 399–440.

34 E. R. Johnson, S. Keinan, P. Mori-Sánchez, J. Contreras-García, A. J. Cohen and W. Yang, Revealing noncovalent interactions, *J. Am. Chem. Soc.*, 2010, **132**, 6498–6506.

35 E. D. Glendening, J. K. Badenhoop, A. E. Reed, J. E. Carpenter, J. A. Bohmann, C. M. Morales, P. Karafiloglou, C. R. Landis and F. Weinhold, NBO 7.0., Theoretical Chemistry Institute, University of Wisconsin, Madison, 2018.

36 J. Contreras-García, E. R. Johnson, S. Keinan, R. Chaudret, J. P. Piquemal, D. N. Beratan

and W. Yang, NCIPLOT: A program for plotting noncovalent interaction regions, *J. Chem. Theory Comput.*, 2011, **7**, 625–632.

37 H. M. Pickett, The fitting and prediction of vibration-rotation spectra with spin interactions, *J. Mol. Spectrosc.*, 1991, **148**, 371–377.

38 J. K. G. Watson, Determination of centrifugal distortion coefficients of asymmetric-top molecules. III. Sextic coefficients, *J. Chem. Phys.*, 1968, **48**, 4517–4524.

39 C. C. Costain, Further comments on the accuracy of r substitution structures, s Trans., *Am. Crystallogr. Assoc.*, 1966, **2**, 157–164.

40 J. Kraitchman, Determination of Molecular Structure from Microwave Spectroscopic Data, *Am. J. Phys.*, 1953, **21**, 17–24.

41 Z. Kisiel, in Spectroscopy from Space, ed. J. Demaison et al. Kluwer Academic Publishers, , Dordrecht, 2001, 91-106.

42 R. S. Ruoff, T. D. Klots, T. Emilsson and H. S. Gutowsky, Relaxation of conformers and isomers in seeded supersonic jets of inert gases, *J. Chem. Phys.*, 1990, **93**, 3142–3150.

43 P. Vansteenkiste, E. Pauwels, V. Van Speybroeck and M. Waroquier, Rules for generating conformers and their relative energies in n-alkanes with a heteroelement O or S: Ethers and alcohols, or sulfides and thiols, *J. Phys. Chem. A*, 2005, **109**, 9617–9626.

44 Y. Kawashima, Y. Tanaka, T. Uzuyama and E. Hirota, Conformations and low-frequency intramolecular motions of 1-butanol, 1-butanethiol, iso-butanol, and iso-butanethiol investigated by fourier transform microwave spectroscopy combined with quantum chemical calculations, *J. Phys. Chem. A*, 2021, **125**, 1166–1183.

Chapter 5. Exploring the distinct conformational equilibria of allyl ethyl ether and allyl ethyl sulfide using rotational spectroscopy and computational chemistry[2]

In chapter 4, both computational and experimental results confirmed that the conformational landscape of the chalcogen-bridged compound is significantly influenced by the central bridged atom (oxygen *vs* sulfur). This was confirmed by the observation of nine conformers for DAE and only one for DAS. The competitive landscape of DAE was due to the presence of hyperconjugative interactions between the oxygen atom and the neighboring allyl chains, whereas these interactions were absent in DAS. Additionally, the lowest energy conformer exhibited a similar orientation of the allyl groups for both molecules. However, the applicability of these findings to other organochalcogens was previously untested. Therefore, to develop a comprehensive understanding of how the central chalcogen atom directs the orientation of different R-groups, this chapter focuses on the study of the allyl ethyl ether (AEE) and allyl ethyl sulfide (AES) compounds. The computational and experimental results for AEE and AES highlight a distinct difference from the previous study on diallyl compounds. In this case, the S-bridged compound exists as a mixture of conformers instead of one dominant form. While it remains true that the ether analogue, AEE, still has the more competitive conformational equilibrium, the inclusion of a saturated side chain has considerably enhanced the richness of the conformational equilibria for the S-bridged analogue. Even more surprising is that the predicted conformer geometries of AEE and AES are substantially different, even for the lowest energy form.

[2] Content appearing in this chapter has been previously published as an article in the Journal of Chemical Physics under the citation: Poonia, T.; van Wijngaarden, J. Exploring the Distinct Conformational Equilibria of Allyl Ethyl Ether and Allyl Ethyl Sulfide using Rotational Spectroscopy and Computational Chemistry, *J. Chem. Phys.*, 2023, 158, 224301.

5.1 Abstract

The conformational landscapes of allyl ethyl ether (AEE) and allyl ethyl sulfide (AES) were investigated using Fourier transform microwave spectroscopy in the frequency range of 5-23 GHz aided by density functional theory (DFT) B3LYP-D3(BJ)/aug-cc-pVTZ calculations. The latter predicted highly competitive equilibria for both species, including 14 unique conformers of AEE and 12 for the sulfur analog AES within 14 kJ mol^{-1}. The experimental rotational spectrum of AEE was dominated by transitions arising from its three lowest energy conformers, which differ in the arrangement of the allyl side chain, while in AES, transitions due to the two most stable forms, distinct in the orientation of the ethyl group, were observed. Splitting patterns attributed to methyl internal rotation were analyzed for AEE conformers I and II, and the corresponding V_3 barriers were determined to be 12.172(55) and 12.373(32) kJ mol^{-1}, respectively. The experimental ground state geometries of both AEE and AES were derived using the observed rotational spectra of the ^{13}C and ^{34}S isotopic species and are highly dependent on the electronic properties of the linking chalcogen (oxygen *vs* sulfur). The observed structures are consistent with a decrease in hybridization in the bridging atom from oxygen to sulfur. The molecular-level phenomena that drive the conformational preferences are rationalized through natural bond orbital and non-covalent interaction analyses. These show that interactions involving the lone pairs on the chalcogen atom with the organic side chains favor distinct geometries and energy orderings for the conformers of AEE and AES.

5.2 Introduction

Chalcogen-substitution has garnered attention in the materials science[1] and polymer electronics communities[1–5] as a way to tune the physical and chemical properties of sensors,[6] light

emitting devices,[7] transistors[8] and photovoltaics.[9] When a heavier chalcogen atom replaces a lighter one, the electronic structure is sensitively affected by the differences in atomic size, polarizability, and electronegativity, which alter molecular-level interactions, and consequently, the bulk and surface properties of the material.[1,10–13] A subclass of these materials are the organochalcogens, compounds having a group 6 element covalently bonded to an organic fragment, with applications across chemistry and biochemistry.[14–20] From a fundamental point of view, these systems serve as excellent prototypes to explore the intramolecular interactions between chalcogen atoms and organic frameworks as the lone pairs on the former can stabilize multiple arrangements of the latter. Rotational spectroscopy combined with quantum chemical calculations provides sensitive and detailed information about the underlying potential energy surfaces that govern such conformational distributions in monomers[21–23] and molecular complexes.[24,25] As conformationally specific processes play a pivotal role in the selectivity and function of chemical and biochemical reactions,[26–30] a further understanding of the factors that define conformational space in organochalcogens may lead to improved design and tunability of these materials.

In *n*-alkane substituted alcohols and thiols, computational models predict that the chalcogen strongly influences the conformational arrangement (even as far as three dihedral angles away) and that sulfur-containing species have more energetically distinct conformers.[31] This has been experimentally verified in ethanethiol,[32] 1-propanethiol[33] and 1-butanethiol,[34] for which rotational spectroscopic measurements confirmed that the most stable conformers have a *gauche* arrangement of the CCSH fragment, whereas in the oxygen analogs,[34–37] the lowest energy conformers slightly favour *trans* CCOH orientations (sometimes by only a few tenths of kJ mol^{-1}). While Vansteenkiste *et al.*[31] predicted that *n*-alkane substituted ethers also present much more

competitive equilibria than their sulfur counterparts, establishing a general rule for the conformational preferences of ethers *vs* sulfides is less tractable because of the complexity in isolating the effects of the two organic fragments.

A recent microwave spectroscopic study of the chalcogen-bridged compounds, diallyl sulfide (DAS) and diallyl ether (DAE)[38] (chapter 4), confirmed that the sulfur compound does give rise to more energetically distinct conformers even when the organic substituent is partially unsaturated, as rotational transitions for nine low energy (< 3 kJ mol^{-1}) conformers for DAE and only one conformer for DAS were observed under analogous experimental conditions. The accompanying quantum chemical calculations revealed that the numerous DAE conformers were stabilized by hyperconjugative interactions involving the lone pairs on oxygen shared with the allyl side chains, which were absent in DAS despite a similar arrangement of the allyl side chains. This finding is consistent with the geometry at the central atom (C-X-C angle), which is ~14° larger in DAE than in sulfide due to the greater hybrid character of the bonding orbitals on oxygen. The prevalence of these stabilizing interactions in the ether was consequently reported to be the underlying cause of the competitive equilibrium of DAE (in comparison with DAS); however, the observation that the CCXC dihedral angles (where X = S or O) are gauche, regardless of the bridging atom identity, is an important distinction in comparison with earlier studies of alcohols and thiols having the chalcogen within the terminal functional group.

To investigate whether it is universally true that organic ethers adopt many more stable forms than their heavy congeners and that the conformational preferences are less unique than when the chalcogen is part of an end group, the present study targets the conformational equilibria of allyl ethyl ether (AEE) and allyl ethyl sulfide (AES). The replacement of one of the allyl side chains of DAE and DAS by a fully saturated ethyl group removes bilateral symmetry and provides

a more direct comparison with the studies on n-alkane substituted organochalcogens.[31] It also introduces the possibility of observing effects due to methyl rotation, as has been reported for related compounds, such as allyl methyl ether[39] (conformer I, V_3 = 8.71(13) kJ mol^{-1}; conformer II, V_3 = 9.93(13) kJ mol^{-1}), allyl methyl sulfide[40] (V_3 = 7.41(34) kJ mol^{-1}), methyl vinyl ether[41] (V_3 =16.03(42) kJ mol^{-1}) and ethyl vinyl ether[42] (V_3 = 12.85(10) kJ mol^{-1}).

In this chapter, the conformational equilibria of AEE and AES are reported for the first time using Fourier transform microwave (FTMW) spectroscopy aided by B3LYP-D3(BJ)/aug-cc-pVTZ calculations. The computational results predicted unique conformational landscapes for both species and were used to assign rotational transitions for three conformers of AEE and two conformers of AES. The experimental rotational constants of several isotopologues of conformers I of AEE and AES were then used to accurately derive their experimental substitution (r_s) and ground state effective (r_0) geometries. For conformers I and II of AEE, a splitting consistent with the methyl internal rotation was resolved sufficiently to derive experimental V_3 barriers that are in good agreement with theoretical estimates. Natural bond orbital (NBO)[43] and non-covalent interaction (NCI)[44] analyses provide insights into the molecular-level interactions that give rise to unique geometric forms in the conformational mixtures of AEE and AES.

5.3 Methods

5.3.1 Experimental methods

Commercial samples of AEE (95%, bp: 67^{o}C) from Sigma-Aldrich Canada and AES (97%, bp: 115-116^{o}C) from Alfa Aesar Canada were used without further purification. A gas mixture was prepared for each compound with ~ 1% AEE or AES diluted in neon (100-200 kPa) using the vapour pressure from the liquid samples at room temperature. To generate a supersonic jet, the gas

mixtures were expanded through a pulsed nozzle (1 mm diameter) into the high vacuum chambers of the spectrometers. The rotational spectra of AEE and AES were then obtained using both chirped-pulse (cp)[45] and Balle-Flygare (BF)[46] FTMW instruments which were previously described in detail.[47,48] Initially, a survey cp-FTMW spectrum of each compound was collected in the frequency range of 8-18 GHz in segments of 2 GHz each and used to assign the most intense transitions of the conformers of AEE and AES. Later, on the basis of the survey spectrum, final frequency measurements were done using the higher resolution, higher sensitivity BF-FTMW spectrometer from 5 to 23 GHz. The collinear arrangement of the resonator axis and the molecular beam in the BF-FTMW spectrometer creates a Doppler splitting of the observed transitions, and the transition frequency is taken as the arithmetic mean of the doublet. With this instrument, rotational transitions have line widths of ~7 kHz (FWHM) and the uncertainty in measuring line positions is typically 2 kHz.

5.3.2 Computational methods

The arrangement of the heavy atoms of the organic side chains is described by three dihedral angles θ, ϕ and λ (defined in Figure 5.1) and gives rise to the various conformers of AEE and AES. Initially, a conformational search was performed using the Conformer-Rotamer Ensemble Sample Tool (CREST) at the GFN2-xTB[49] level of theory making use of extended tight binding (xTB).[50,51] The conformational search identified 34 and 44 possible molecular geometries for AEE and AES, respectively. Next, these potential geometries were optimized using dispersion-corrected density functional theory (DFT) at the B3LYP[52]-D3(BJ)[53,54]/aug-cc-pVTZ[55] level using the Gaussian 16 program.[56] To confirm the nature of the stationary points and to obtain electronic energies with zero-point energy (ZPE) corrections and quartic centrifugal distortion constants,

harmonic frequency calculations were performed. To generate the interconversion pathways between conformers, relaxed potential energy curves were derived for both molecules at the same level of theory from a series of single point energy calculations involving a change in the dihedral angle of interest by 10°. In a similar manner, the methyl internal rotation barriers (V_3) were calculated and are plotted in Figure 5.2 for conformers I and II of AEE. To investigate intra- and intermolecular contacts, non-covalent interaction (NCI)[44] and natural bond orbital (NBO)[43] calculations were done using the NCIPLOT[57] and NBO 7.0[58] programs, respectively.

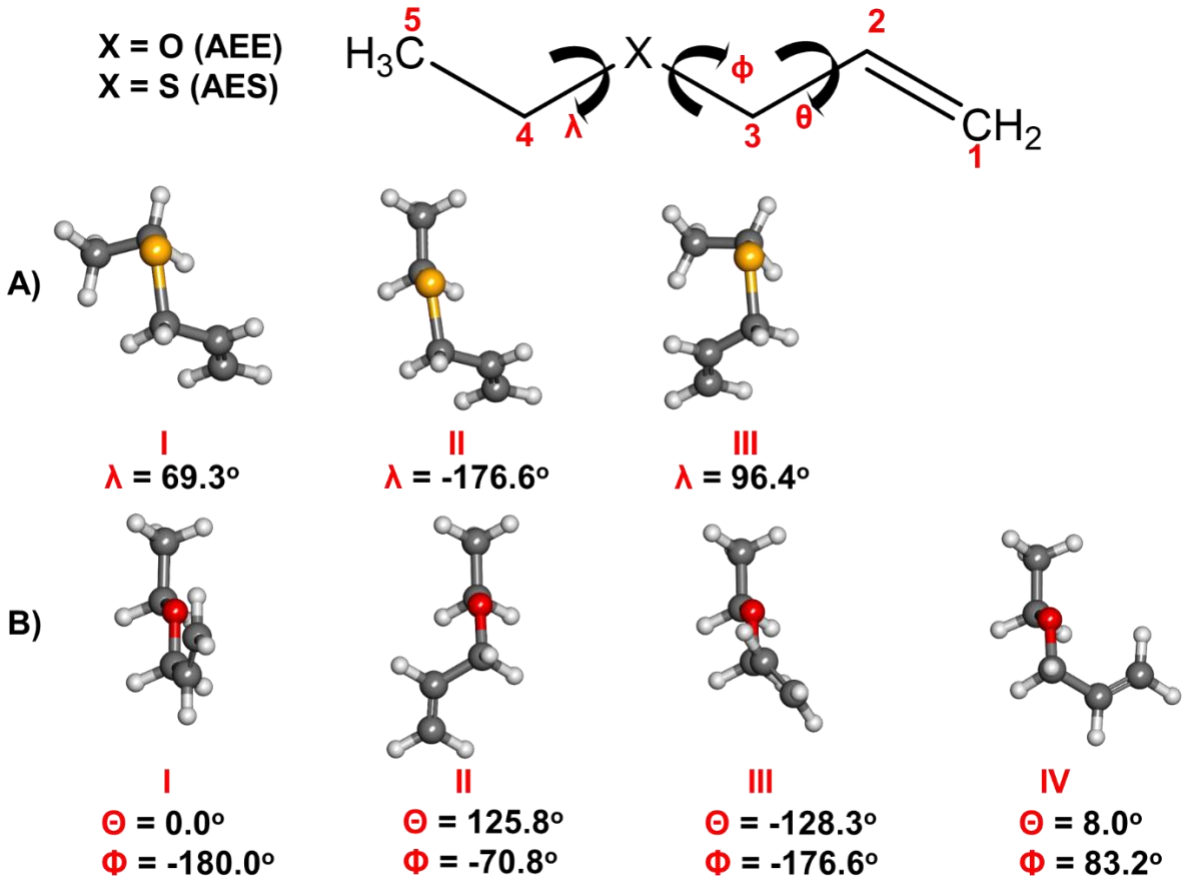

Figure 5.1 Minimum energy conformers of A) AES and B) AEE within 5 kJ mol^{-1} of the global minimum at the B3LYP-D3(BJ)/aug-cc-pVTZ level of theory. The internal rotation around the θ, ϕ and λ dihedral angles is responsible for the different conformers.

5.4 Results

5.4.1 Conformational space of AEE and AES

A surprisingly rich conformational space was identified for both AEE and AES, as geometry optimization calculations identified 14 unique conformers for AEE within 13.4 kJ mol^{-1} and 12 for AES within 13 kJ mol^{-1}. The Cartesian coordinates of all conformers of AES and AEE are summarized in the ESI (Electronic Supplementary Material file) in Tables S1-S26. Their calculated energetic and spectroscopic parameters at the B3LYP-D3(BJ)/aug-cc-pVTZ level of theory are given in Table 5.1. As high energy conformers are not anticipated to be sufficiently populated at room temperature to persist in the supersonic jet for microwave spectroscopic detection, only conformers with relative energies within 5 kJ mol^{-1} of the global minimum were considered further and these geometries are shown in Figure 5.1 for both compounds. The labeling of conformers was done using Roman numerals to describe their stability ordering where conformer I is the most stable conformer (relative energy set to zero).

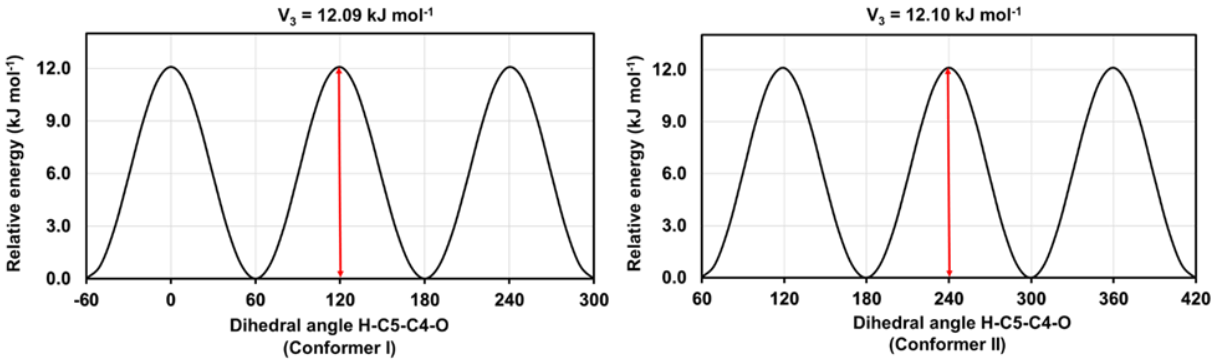

Figure 5.2 Methyl internal rotation potential energy scan for AEE conformers I and II at B3LYP-D3(BJ)/aug-cc-pVTZ level of theory. The analogous barrier in conformer III was found to be 11.97, and it was 11.20 and 11.84 kJ mol^{-1} in conformers I and II of AES, respectively.

Table 5.1 Calculated energetic and spectroscopic parameters for the conformers of AES and AEE at the B3LYP-D3(BJ)/aug-cc-pVTZ level of theory.

AES	ΔE_0[a]	P[b]	A/B/C[c]	$\lvert\mu_a\rvert$/ $\lvert\mu_b\rvert$/ $\lvert\mu_c\rvert$[d]
I	0.0	55.8	3667/2049/1531	0.5/1.3/0.2
II	2.2	23.1	4792/1626/1312	0.5/1.2/0.6
III	4.6	8.9	3518/2140/1499	0.8/1.1/0.7
IV	7.6	2.6	6998/1309/1199	0.7/1.3/0.9
V	8.2	2.0	4166/1794/1644	0.0/1.4/0.7
VI	8.3	1.9	7556/1275/1188	0.7/1.3/0.8
VII	8.8	1.6	4881/1576/1375	0.1/1.6/0.2
VIII	9.0	1.4	7193/1283/1190	0.0/1.2/1.0
IX	9.4	1.3	4944/1582/1317	0.5/1.2/1.1
X	10.8	0.7	3741/2087/1623	0.1/0.9/1.4
XI	12.8	0.3	7341/1404/1261	0.9/1.5/0.6
XII	13.0	0.3	9831/1267/1146	0.6/1.7/0.0
AEE	ΔE_0[a]	P[b]	A/B/C[c]	$\lvert\mu_a\rvert$/ $\lvert\mu_b\rvert$/ $\lvert\mu_c\rvert$[d]
I	0.0	31.7	9584/1712/1493	0.7/1.2/0.0
II	0.8	23.0	8502/1745/1582	0.5/0.9/0.5
III	1.3	18.8	15000/1385/1346	0.3/1.1/0.0
IV	2.8	10.3	6998/2069/1761	0.1/0.2/1.2
V	5.4	3.6	10237/1703/1602	1.1/1.1/0.4
VI	5.6	3.3	6169/2113/1845	0.3/1.2/0.1
VII	6.3	2.5	10729/1572/1462	0.6/0.6/1.0
VIII	7.0	1.9	12836/1487/1451	0.6/0.7/0.9
IX	7.3	1.7	7947/1966/1803	0.3/0.2/1.3
X	7.6	1.5	5434/2376/1886	0.5/0.8/0.8
XI	9.0	0.8	5621/2478/2027	0.5/0.1/1.3
XII	11.3	0.3	7988/1866/1629	0.5/0.6/1.1

XIII	11.4	0.3	11737/1554/1534	0.3/0.2/1.3
XIV	13.4	0.1	6639/2031/1704	0.1/0.5/1.2

[a]Zero-point energy (ZPE) corrected relative energies in kJ mol^{-1}, [b]Boltzmann population at 298K in %,), [c]Rotational constants in MHz, [d]Magnitude of the electric dipole moment components in Debye.

5.4.2 Spectral analysis

The theoretical results (Table 5.1) were used to simulate the rotational spectra of the low-energy forms of AEE and AES for comparison with the experimental data. From this, transitions due to three near prolate top conformers of AEE and two conformers of AES were assigned in the cp-FTMW spectrum. For the ground states (conformer I) of AEE and AES, transitions due to all five ^{13}C isotopologues were also observed in natural abundance, as were those of the ^{34}S analog of AES with intensities of ~1% and ~4% of the corresponding parent lines, respectively. A portion of the broadband spectrum of AEE featuring transitions of the three assigned conformers is shown in Figure 5.3, revealing spectral intensities that are qualitatively consistent with the predicted populations and dipole moments. A more quantitative analysis of the observed intensities, to confirm the conformer abundances, is challenging because of variations in instrument response across the spectral region and differences in spectroscopic constants such that comparable transitions have distinct energies. The initial assignments were confirmed using measurements from the BF-FTMW spectrometer, and additional transitions were recorded to extend the frequency coverage and augment the dataset with lower intensity features.

During higher resolution measurements of AEE, a splitting pattern was observed in some transitions of conformers I and II. These were readily resolved for 20 strong Q-branch *b*-type transitions of conformer II with $K_a' = 2$ and also for the R-branch *a*-type transitions (both conformers) and P-branch *b*-type transitions (conformer I) with $K_a' = 3$. Initially, we attempted to model the splitting as a tunnelling motion involving a torsion of the allyl group as reported for

allyl methyl amine,[21] but this was not consistent with the observed *c*-type transitions, which would need to connect the tunnelling states (+/-) to create closed loops in the energy level diagram. In the end, the tunnelling splitting was successfully treated as a methyl rotation with the individual components fit to the A/E states of the internal rotor. A sample spectrum is shown in Figure 5.4. Although conformer III has a similar V_3 barrier for this motion, splitting was not observed in its spectrum. This was attributed to the fact that only the more intense $K_a = 0$ and 1 transitions were measured for this higher energy form. In conformers I and II, the analogous lower K_a transitions did not exhibit splitting.

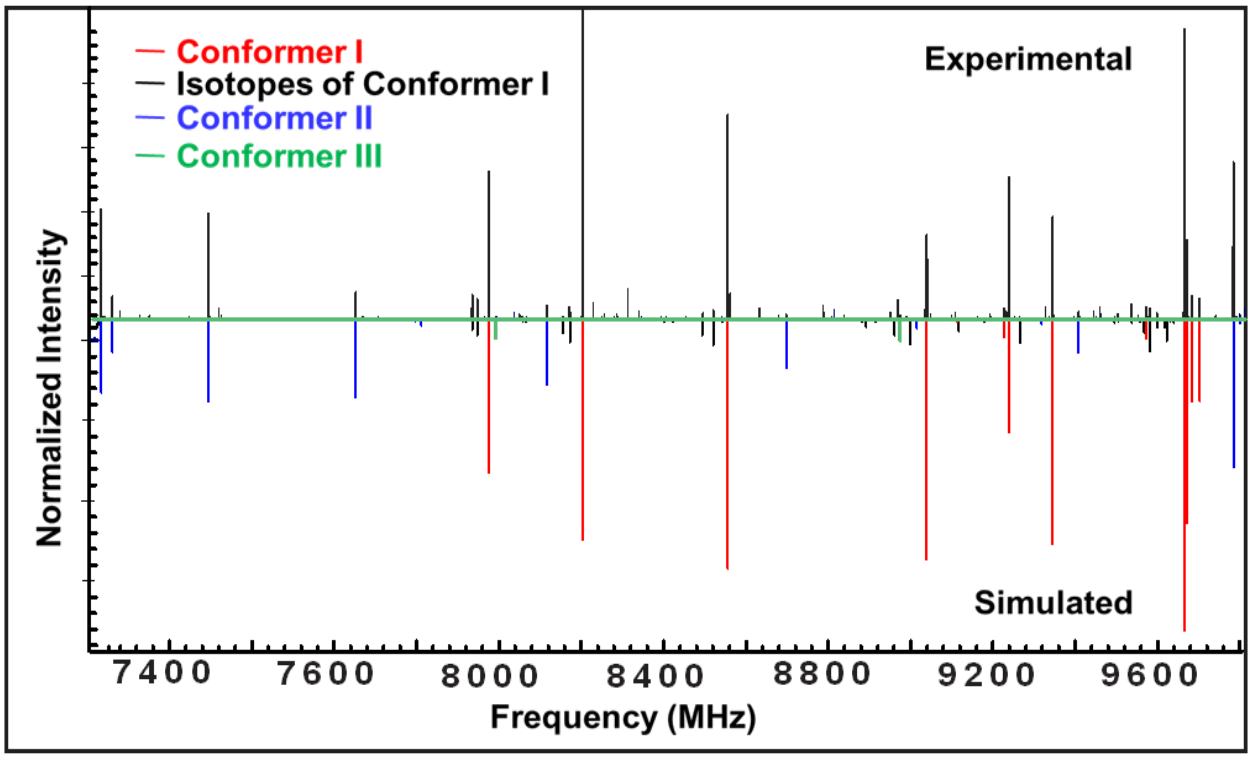

Figure 5.3 Portion of the broadband cp-FTMW spectrum (1.5×10^6 free induction decays) of AEE for conformer I and its minor heavy atom isotopic species, plus those of conformers II and III. The top portion is the experimental spectrum, and the lower portion is the simulated spectrum using the fitted parameters.

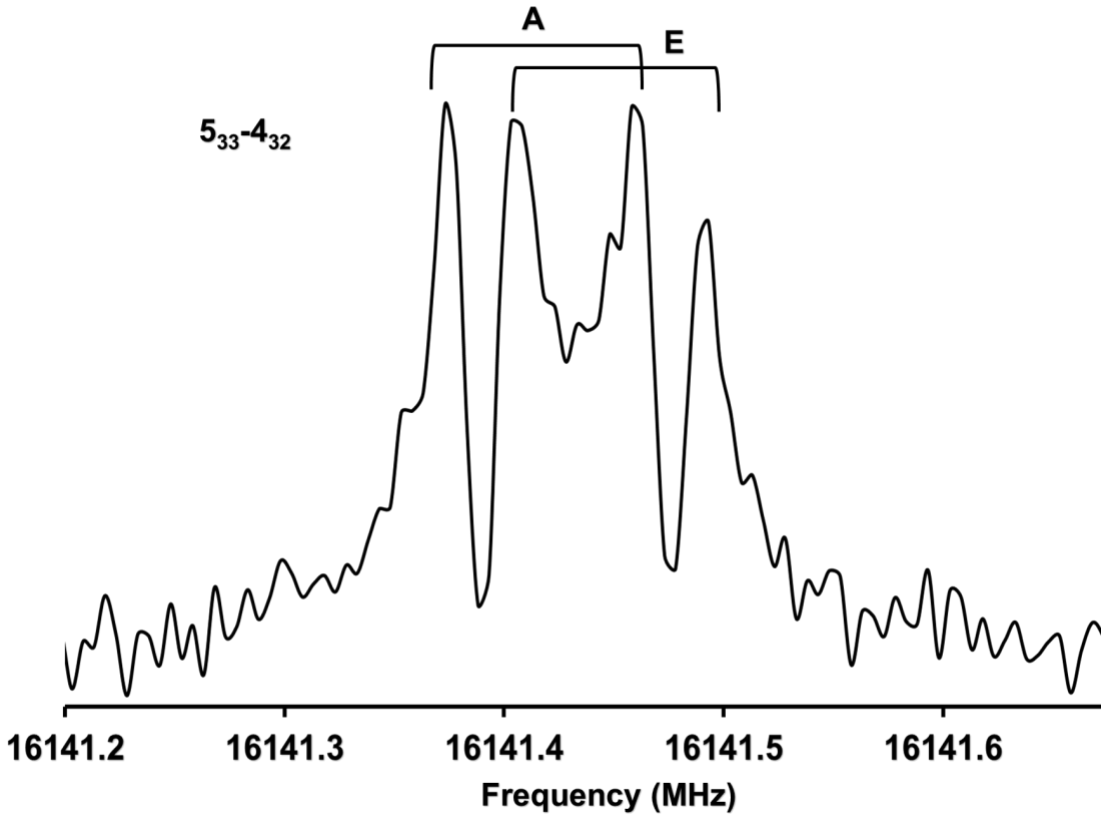

Figure 5.4 A sample of BF-FTMW spectrum showing A/E splitting pattern due to the methyl internal rotation in conformer I in addition to the Doppler splitting of the instrument.

For molecular species whose spectra showed no tunnelling splitting, rotational transitions were fit using Pickett's SPFIT program[59] with Watson's A-reduced Hamiltonian[60] in the I^r representation to determine the experimental ground state rotational constants and centrifugal distortion constants. The results are provided in Table 5.2 and Table 5.3 for the conformers and isotopologues of AES and AEE, respectively. For conformers I and II of AEE, the observed spectra were fit using the XIAM program,[61] which accounts for the methyl internal rotation using the combined axis method (CAM) and allows the derivation of key parameters for the molecule and the methyl rotor, including the V_3 barrier. This was done by assuming a value of the rotational constant of the methyl top (F_0) as well as the angle between the rotor a-axis and the principal

inertial a-axis of the molecule (Δ) based on the theoretical geometry obtained from the B3LYP/D3(BJ)/aug-cc-PVTZ level of theory. The parameters determined in the fit are summarized in Table 5.3 and compared with those derived from SPFIT (Table 5.4), where transitions within the two states (A/E) are treated separately. The complete line lists of the observed transition frequencies are given in Tables S29-S48 with the residuals (obs-calc) from the two fitting methods. Overall, the experimentally derived rotational and centrifugal distortion constants are in good agreement with their theoretical counterparts in Tables S27 and S28 of the electronic supplementary material. Furthermore, the internal rotation barriers of the methyl group for conformers I and II of AEE, 12.172(55) and 12.373(32) kJ mol^{-1}, respectively, are very similar to those from the B3LYP-D3(BJ)/aug-cc-pVTZ calculations (12.09 and 12.10 kJ mol^{-1}), which lends support to the assertion that methyl rotation is the origin of the observed splitting. This is similar to the V_3 barrier found in ethyl vinyl ether (12.85(10) kJ mol^{-1})[42] by analyzing rotational transitions in excited vibrational states when the ethyl adopts a comparable orientation relative to the bridging oxygen atom.

Table 5.2 Experimental spectroscopic parameters of AES for conformer I, including its ^{13}C and ^{34}S isotopologues, and conformer II.

Parameter	SPFIT							
	Conformer I	$^{13}C1$	$^{13}C2$	$^{13}C3$	^{34}S	$^{13}C4$	$^{13}C5$	Conformer II
A/MHz[a]	3715.979404(78)	3687.22654(48)	3713.84057(47)	3688.17448(53)	3655.33974(19)	3695.58856(72)	3649.42822(39)	4890.40541(17)
B/MHz	2038.353451(57)	1994.35965(84)	2011.43017(82)	2029.04156(92)	2028.02220(18)	2021.8542(12)	2014.12893(49)	1621.808257(76)
C/MHz	1530.615636(54)	1501.05836(48)	1515.45705(47)	1525.45944(52)	1514.60159(11)	1521.78901(72)	1507.45448(22)	1315.459828(69)
Δ_J/kHz[b]	2.27646(72)	2.176(24)	2.202(24)	2.216(27)	2.1802(24)	2.181(37)	2.323(13)	0.85223(86)
Δ_{JK}/kHz	-3.9803(21)	-3.298(76)	-3.868(74)	-4.022(86)	-3.237(13)	-3.89(11)	-4.765(55)	-5.8879(58)
Δ_K/kHz	7.4990(34)	6.588(65)	7.641(64)	7.743(72)	6.403(12)	7.395(85)	8.674(50)	21.231(17)
δ_J/kHz	0.82056(32)	0.7738(98)	0.7892(96)	0.799(11)	0.7862(15)	0.780(15)	0.8458(59)	0.26699(50)
δ_K/kHz	3.0463(33)	3.23(24)	2.90(23)	2.68(25)	3.181(20)	2.52(34)	2.626(83)	1.359(15)
$\mu_a/\mu_b/\mu_c$[c]	y/y/y	y/y/n	y/y/n	y/y/n	y/y/n	y/y/n	y/y/n	y/y/y
N[d]	110	22	22	22	46	24	23	85
σ/kHz[e]	1.2	0.9	0 .9	1.0	1.2	1.4	0.8	1.3

[a]Rotational constants; [b]quartic centrifugal distortion constants; [c]electric dipole moment components ("y" if observed and "n" if not observed); [d]total number of lines (N) in the fit; [e]root-mean-square error of the fit (σ). A complete list of the calculated rotational parameters at the B3LYP-D3(BJ)/aug-cc-pVTZ is given in Table S27.

Table 5.3 Experimental spectroscopic parameters of AEE for conformer I, including its ^{13}C isotopologues, conformer II, and conformer III.

Parameter	XIAM	SPFIT					XIAM	SPFIT
	Conformer I	$^{13}C1$	$^{13}C2$	$^{13}C3$	$^{13}C4$	$^{13}C5$	Conformer II	Conformer III
A/MHz[a]	9469.24234(37)	9297.71651(46)	9453.45716(50)	9322.08486(49)	9429.01237(45)	9396.64993(49)	8444.66706(55)	14855.87928(48)
B/MHz	1724.23322(8)	1694.48529(12)	1700.41437(14)	1721.64552(16)	1708.89034(13)	1684.76859(13)	1754.76066(12)	1389.64874(11)
C/MHz	1500.88913(12)	1474.05160(11)	1482.44124(13)	1495.19360(12)	1488.28301(11)	1469.14317(11)	1587.99554(14)	1350.728993(91)
Δ_J/kHz[b]	0.27568(69)	0.2739(10)	0.2651(13)	0.2727(18)	0.2688(11)	0.2661(12)	0.8631(11)	0.20491(84)
Δ_{JK}/kHz	-2.5459(69)	-2.581(13)	-2.454(15)	-2.477(17)	-2.504(13)	-2.514(13)	-14.2207(65)	-12.752(22)
Δ_K/kHz	27.052(31)	[27.052]	[27.052]	[27.052]	[27.052]	[27.052]	102.29(11)	[371.092]
δ_J/kHz	0.05949(35)	0.0639(12)	0.0594(17)	0.0611(15)	0.0604(13)	0.0594(13)	0.20645(17)	-0.00725(46)
δ_K/kHz	0.719(28)	[0.719]	[0.719]	[0.719]	[0.719]	[0.719]	1.728(46)	[-1.363]
V_3 (kJ/mol)	12.172(55)						12.373(32)	
F_0 (GHz)	[160.291]						[160.309]	

Δ (rad)	[2.295]						[2.838]	
$\mu_a/\mu_b/\mu_c$[c]	y/y/n	y/y/n	y/y/n	y/y/n	y/y/n	y/y/n	y/y/y	y/y/n
N[d]	138	30	30	29	32	31	164	30
σ/kHz[e]	2.9	1.1	1.3	1.2	1.2	1.2	2.9	1.1

[a]Rotational constants; [b]quartic centrifugal distortion constants; [c]electric dipole moment components ("y" if observed and "n" if not observed); [d]total number of lines (*N*) in the fit; [e]root-mean-square deviation of the fit (σ). The value in brackets for the isotopes were fixed to the conformer I values and for conformer I and II to the values derived from theoretical molecular geometry obtained at the B3LYP-D3(BJ)/aug-cc-pVTZ level and for conformer III to the predicted values obtained at the same level of theory. A complete list of the calculated rotational parameters at the B3LYP-D3(BJ)/aug-cc-pVTZ is given in Table S28.

Table 5.4 Experimental spectroscopic parameters of AEE for conformer I and conformer II using SPFIT and XIAM.

Parameter	SPFIT		XIAM	SPFIT		XIAM
	Conformer I(A)	Conformer I(E)	Conformer I	Conformer II(A)	Conformer II(E)	Conformer II
A/MHz[a]	9469.24263(48)	9469.2434(12)	9469.24234(37)	8444.66709(47)	8444.6687(23)	8444.66706(55)
B/MHz	1724.223937(89)	1724.22394(22)	1724.23322(8)	1754.74966(11)	1754.74959(55)	1754.76066(12)
C/MHz	1500.89835(14)	1500.89863(34)	1500.88913(12)	1588.00653(13)	1588.00657(62)	1587.99554(14)
Δ_J/kHz[b]	0.27488(80)	0.2768(20)	0.27568(69)	0.8632(10)	0.8629(51)	0.8631(11)
Δ_{JK}/kHz	-2.5383(80)	-2.541(20)	-2.5459(69)	-14.2201(59)	-14.227(29)	-14.2207(65)
Δ_K/kHz	26.902(36)	27.197(90)	27.052(31)	101.40(10)	103.24(50)	102.29(11)

δ_J/kHz	0.05981(41)	0.0594(10)	0.05949(35)	0.20639(15)	0.20647(75)	0.20645(17)
δ_K/kHz	0.723(33)	0.661(81)	0.719(28)	1.753(42)	1.72(21)	1.728(46)
V_3 (kJ/mol)			12.172(55)			12.373(32)
F_o (GHz)			[160.291]			[160.309]
Δ (rad)			[2.295]			[2.838]
$\mu_a/\mu_b/\mu_c$[c]	y/y/n	y/y/n	y/y/n	y/y/y	y/y/y	y/y/y
N[d]	69	69	138	82	82	164
σ/kHz[e]	2.3	5.6	2.9	1.8	8.8	2.9

[a]Rotational constants; [b]quartic centrifugal distortion constants; [c]electric dipole moment components ("y" if observed and "n" if not observed); [d]total number of lines (*N*) in the fit; [e]root-mean-square deviation of the fit (σ). For conformer I and II the values in the brackets were fixed to the values derived from theoretical molecular geometry obtained at the B3LYP-D3(BJ)/aug-cc-pVTZ level of theory.

5.4.3 Structure determination

With rotational spectra observed for multiple isotopic species of the ground states of AEE and AES, their internal geometric parameters involving the heavy atoms were estimated using the experimental rotational constants given in Tables 5.2 and 5.3. First, positions of the substituted atoms were determined from Kraitchman's equations[62] as executed in Kisiel's KRA program.[63] The signs of the Kraitchman coordinates were deduced by comparing the positions of atoms in the equilibrium geometry (r_e) at the B3LYP-D3(BJ)/aug-cc-pVTZ level of theory, and the imaginary c-coordinate for oxygen in AEE was set to zero in the subsequent analysis as it lies in the ab-plane of the molecule. The results are given in Table S49 of the ESI. The atomic positions and their Costain errors[64] were then used to calculate the internal parameters of the r_s geometry using the EVAL routine,[63] and the results are summarized in Tables 5.5 and 5.6 for both molecules. For AES, the r_e and r_s values for most parameters match to within two standard deviations with the exception of a few, r(C3-S), r(S-C4) and ∠C1-C2-C3-S, that depend on the position of sulfur, which is not well-determined due to its small c-coordinate (-0.08628±0.01739Å from Table S49). As the signal was not sufficient to observe transitions of ^{18}O for AEE, fewer parameters were determined in comparison with AES, but all derived values are within two standard deviations of the r_e values.

Next, the effective ground state geometries (r_0) of AES and AEE were derived using Kisiel's STRFIT program,[63] which performs a least squares fit of the selected geometric parameters to the moments of inertia of all observed isotopologues. For AES and AEE, 21 and 12 rotational constants were used in the fit, respectively. Since all of the heavy atoms in AEE are in the ab-plane (Figure 5.5), the geometry was derived using only 2 rotational constants (A and B) for each isotopologue. The internal coordinates involving the hydrogen atoms for both AEE and

AES (and oxygen in the case of AEE) were fixed to the computationally derived values at the B3LYP-D3(BJ)/aug-cc-pVTZ level of theory. The resulting r_0 parameters are summarized in Tables 5.5 and 5.6 and, based on agreement with the theoretical predictions, provide confirmation that the assigned spectra arise from conformers I of AEE and AES. It is interesting to note that the bridging angle C-S-C (~101°) in the sulfide is smaller than the C-O-C angle (~113°) in AEE. This is analogous to what was reported in DAE and DAS[38] and is consistent with the hybridization of the bridging atoms identified from the NBO calculations,[58] with the C–S bonding orbitals on sulfur possessing a larger p-character (84%-85.03%) and favouring angles closer to those of atomic p-orbitals in AES compared to those on oxygen (72.2%–72.05%) in AEE, where the geometry at the center atom is closer to tetrahedral. This result confirms that hybridization models of bonding used to understand the molecular geometry of organic compounds that include second row elements (such as an sp^3 hybridized oxygen in this case) do not necessarily describe bonding in heavier p-block elements.

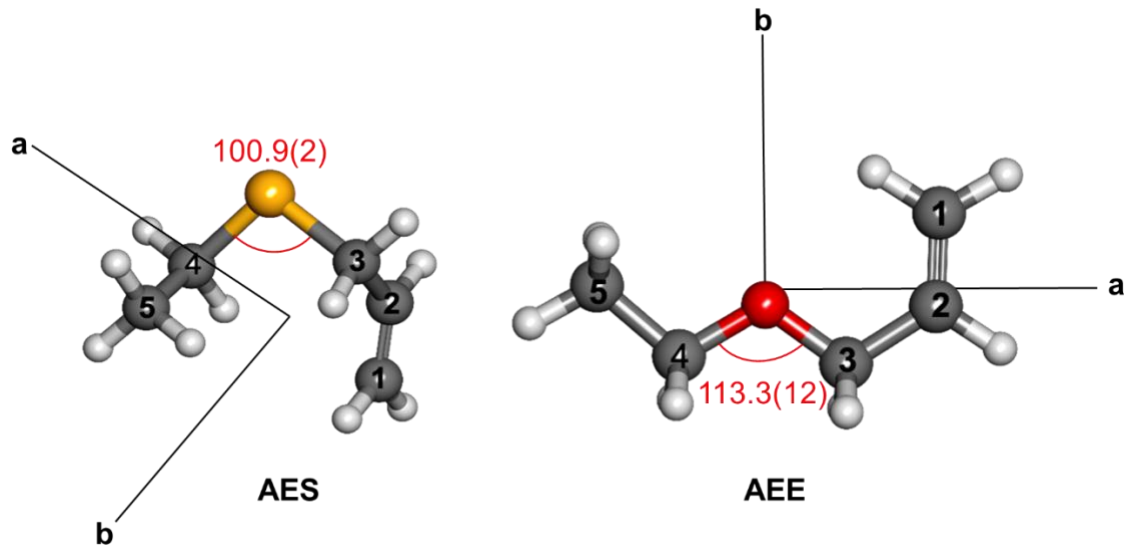

Figure 5.5 Molecular geometries of conformers I of AES and AEE corresponding to the parameters in Tables 5.5 and 5.6.

Table 5.5 Equilibrium (r_e) (B3LYP/aug-cc-pVTZ), substitution (r_s), ground state effective (r_0) structural parameters (bond lengths in Å; angles in deg) determined for AES.

	$\mathbf{r_e}$	$\mathbf{r_s}$	$\mathbf{r_0}$
C1-C2	1.328	1.339(8)	1.343(8)
C2-C3	1.489	1.498(6)	1.482(10)
C3-S	1.841	1.810(8)	1.832(5)
S-C4	1.827	1.808(6)	1.796(5)
C4-C5	1.521	1.523(3)	1.536(8)
∠*C1-C2-C3*	124.3	123.0(7)	123.8(8)
∠ *C3-S-C4*	101.0	100.8(1)	100.9(2)
∠*S-C4-C5*	114.5	114.3(5)	114.4(4)
∠*S-C3-C2*	112.1	112.6(5)	112.5(5)
∠*C1-C2-C3-S*	-113.2	-116.5(5)	-115.3(8)
∠*C2-C3-S-C4*	62.8	62.7(7)	63.3(5)
∠*C3-S-C4-C5*	69.3	69.8(6)	69.4(4)

Table 5.6 Equilibrium (r_e) (B3LYP/aug-cc-pVTZ), substitution (r_s), ground state effective (r_0) structural parameters (bond lengths in Å; angles in deg) determined for AEE.

	$\boldsymbol{r_e}$	$\boldsymbol{r_s}$	$\boldsymbol{r_0}$
C1-C2	1.325	1.328(7)	1.337(10)
C2-C3	1.494	1.505(6)	1.498(8)
C3-O	1.408	-	1.398(14)
O-C4	1.417	-	1.407(9)
C4-C5	1.513	1.514(4)	1.513(8)
∠*C1-C2-C3*	125.4	124.7(6)	124.7(4)
∠*C3-O-C4*	113.2	-	113.3(13)

∠O-C3-C2	111.3	-	111.2(6)
∠O-C4-C5	108.8	-	109.1(9)

5.5 Discussion

Quantum chemical calculations predicted rich conformational landscapes for both AEE and AES arising from variations in the three dihedral angles that define the orientation of the organic fragments. In the jet-cooled rotational spectrum, the relative stabilities of the three lowest energy conformers of AEE and two most stable conformers of AES were confirmed based on the observed spectral patterns that were consistent with the theoretical energy ordering. The absence of higher energy conformers is fairly common in jet-cooled studies, as it is well known that these can relax to lower energy geometries during the molecular beam expansion if the interconversion barrier is smaller than ~5 kJ mol^{-1}.[65] To further investigate the absence of conformer IV in AEE and conformer III in AES (as their relative energies indicate room temperature Boltzmann populations of around 9%-10%), potential relaxation pathways were calculated using systematic scans of the dihedral angles involved in the interconversion between these and lower energy conformers. Figure 5.6 shows the energy profile for the conversion of conformer III→II (barrier ~1.7 kJ mol^{-1}) of AES and conformer IV→I of AEE (barrier ~4.9 kJ mol^{-1}) by changing the λ and ϕ dihedral angles (Figure 5.1), respectively, while other parameters are relaxed. These barriers are sufficiently low to enable relaxation and explain the absence of transitions attributable to conformers III of AES and conformer IV of AEE in the rotational spectrum.

For AEE and AES, the computational results in Table 5.1 highlight a distinct difference from the earlier study of the related diallyl compounds[38] (chapter 4), as now, the S-bridged

compound exists as a mixture of conformers at room temperature with three structures falling within a 5 kJ mol^{-1} energy window rather than one dominant form as in the earlier study of DAS. While it remains true that the lighter congener AEE still has the more competitive conformational equilibrium (as the conformers are more closely spaced energetically than for AES in Table 5.1), the inclusion of an ethyl side chain has drastically altered the richness of the conformational equilibria for the S-bridged compound. Even more notable is that the predicted conformer geometries of AEE and AES are substantially different, and surprisingly, this is even true for the lowest energy form (Figure 5.1) in contrast to the case of DAE and DAS,[38] in which the organic groups were similarly oriented in the ground state structures. A closer inspection of the most stable structures in Figure 5.1 shows that, in AES, the allyl side chain is described by dihedral angles (θ, ϕ) of similar magnitude such that the conformers are largely differentiated by the orientation of the ethyl fragments (λ). The opposite dependence is seen in the lowest energy forms of AEE, with the ethyl groups adopting similar positions (λ) while the dihedral angles describing the allyl fragment (θ, ϕ) vary. The results of this comparison suggest that the bridging chalcogen atoms (oxygen *vs* sulfur) engage in unique interactions with saturated and unsaturated organic groups and that this key difference governs the conformational preferences of AEE and AES.

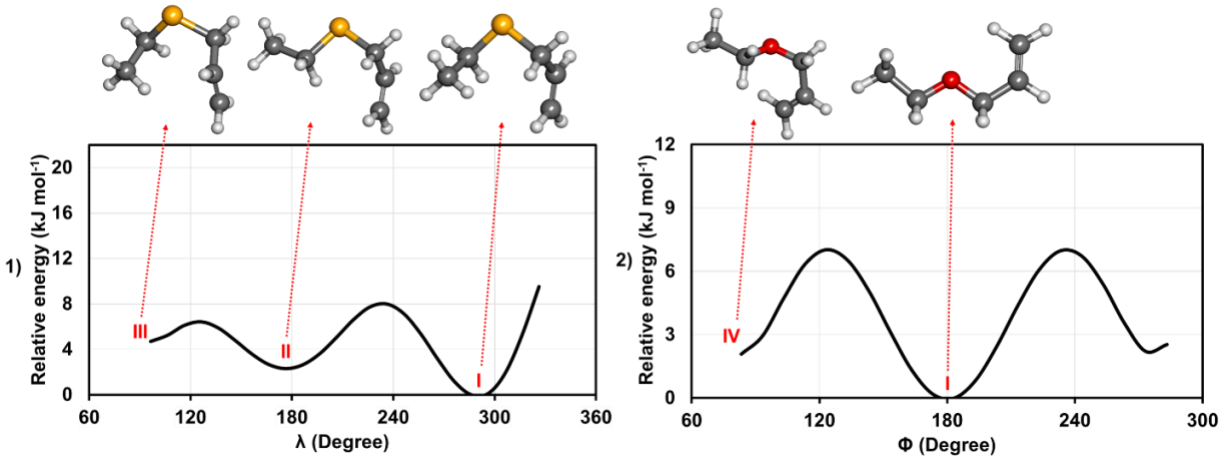

Figure 5.6 Interconversion relaxation pathways 1) AES = III→II and 2) AEE = IV→I attained at the B3LYP-D3(BJ)/aug-cc-pVTZ level of theory.

To identify possible non-covalent interactions that give rise to such distinct conformers of AES and AEE and to understand the underlying reasons for the energy ordering, we plotted the isosurfaces of the reduced electron density gradient derived from NCI calculations.[57] For AEE, the results (Figure 5.7) reveal blue-green and red regions that reflect the balance of attractive and repulsive interactions, respectively. In conformer I, the overall stabilizing influence seems to be due to attractive interactions between the terminal C–H bond of the allyl fragment and the oxygen atom (C–H---O), as seen by the blue isosurface appearing between these moieties. Similar interactions (C–H---N) were reported in the lower energy forms of diallyl amine (DAA)[22] and in a number of the low energy forms of DAE (although not the global minimum)[38] where the allyl group adopts an analogous orientation. For the remaining conformers of AEE and AES depicted in Figure 5.7, it is difficult to predict the reason for the stability ordering due to the presence of largely green isosurfaces, which indicate a combination of weak contacts between different bonds or atoms that can be either net attractive or repulsive interactions (referring to the color-coded

scale in Figure 5.7). In such cases, second-order perturbation energies from NBO analyses can help identify specific orbital interactions and their relative importance in stabilizing the conformer.

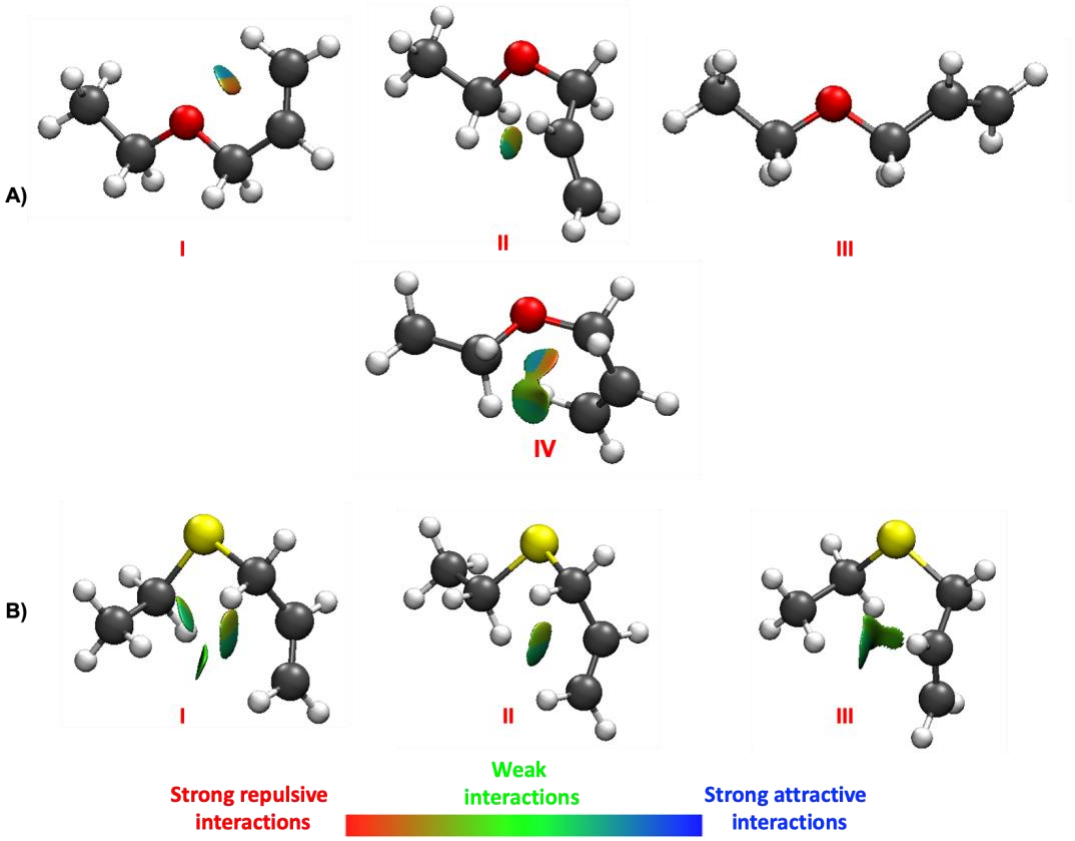

Figure 5.7 NCI isosurfaces (s = 0.05, color scale for -0.02 < ρ < + 0.02 au) for A) AEE conformers I-IV and B) for conformers I-III of AES.

The stabilizing interactions identified via NBO analysis are provided as the supplementary material in Table S50, and a shorter summary is provided in Table 5.7 to highlight some key interactions involving the lone pair (LP) electron density on sulfur and oxygen. For AES, for example, there are no significant differences in the intramolecular contacts between sulfur and the allyl fragment (Table S50) for the three stable conformers. This is consistent with the θ and ϕ

dihedral angles being similar for all three; however, note that conformer III differs from the other two in the signs of both θ and ϕ, but the magnitude is comparable. This orientation of the allyl fragment is also observed for the most stable geometries of both DAE and DAS, where both side chains point downward, and was found to facilitate charge transfer of LP electron density from the chalcogen to the π* orbital of the C=C bond. Maintaining the stability offered by this orientation of the allyl group, the relative energies of conformers I through III are then dependent on LP donation from sulfur into the C–C bond (LP(S) → σ*C_5–C_4) and neighbouring methylene C–H bonds (LP(S) → σ*C_4–H) of the ethyl fragment. The corresponding second-order perturbation energies for these interactions, which vary with λ (i.e., the orientation of ethyl), are summarized in Table 5.7 for AES.

Table 5.7 Select second-order perturbation energy for conformers I-III of AES and conformers I-IV of AEE with charge transfer interactions involving the lone pair (LP) on S and O. Figure 5.1 displays the labels for the atomic numbers, and the complete results are listed in ESI, Table S50.

AES Interaction	Conformer I E (kJ/mol)	Conformer II E (kJ/mol)	Conformer III E (kJ/mol)
$LP_1(S) \rightarrow \sigma^*C_4–H'$	–	–	3.6
$LP_2(S) \rightarrow \sigma^*C_4–H$	–	16.6	5.8
$LP_2(S) \rightarrow \sigma^*C_4–H'$	14.8	16.7	3.1
$LP_1(S) \rightarrow \sigma^*C_5–C_4$	3.7	–	–
$LP_2(S) \rightarrow \sigma^*C_5–C_4$	17.4	–	20.6
$LP_2(S) \rightarrow \sigma^*C_5–H'$	3.6	–	4.2

AEE Interaction	Conformer I E (kJ/mol)	Conformer II E (kJ/mol)	Conformer III E (kJ/mol)	Conformer IV E (kJ/mol)
$LP_1(O) \rightarrow \sigma^*C_3–C_2$	5.4	3.3	4.6	2.5
$LP_2(O) \rightarrow \sigma^*C_3–C_2$	–	27.2	–	4.7
$LP_2(O) \rightarrow \pi^*C_2–C_1$	–	4.9	–	3.8
$LP_1(O) \rightarrow \sigma^*C_3–H$	3	4.9	3.1	-

$LP_1(O) \rightarrow \sigma^*C_3–H'$	3	11.1	–	-
$LP_2(O) \rightarrow \sigma^*C_3–H$	28.6	27.2	25.1	10
$LP_2(O) \rightarrow \sigma^*C_3–H'$	28.6	–	29.6	7.3

Interestingly, as noted earlier, the ethyl side chains in the most stable conformers of AEE are positioned similarly, and it is the unique interactions between the LP electron density on oxygen and the allyl fragments that influence the relative energies of the first four conformers. In this case, the conformational equilibrium is very competitive, as seen by the similar energies in Table 5.1, and thus, it is difficult to pinpoint a specific interaction or set of interactions that give rise to this energy ordering. The overall ordering is, instead, a balance of many subtle effects, of which only a small subset involving the allyl fragment is included in Table 5.7 in AEE. In comparing the NBO results for AEE and AES, the overarching trend appears to be that it is the bridging atom's LP interactions with the saturated side chains that are most important for defining the relative stability of conformers in the sulfide and with the (partially) unsaturated group in the case of the ether. It would be interesting to extend this to other side chains, and in fact, we are currently pursuing several other examples to test the universality of this finding.

5.6 Conclusions

The conformational equilibria of AEE and AES were characterized using quantum chemical calculations and Fourier transform microwave spectroscopy. Rotational transitions consistent with the three lowest energy forms of AEE and two most stable conformers of AES were assigned. A tunnelling splitting in the high resolution spectra of conformers I and II of AEE was attributed to methyl internal rotation and used to derive the corresponding V_3 barriers that

were consistent with theoretical predictions. The results of this study highlight the dramatic differences in the stability of various conformers of AEE and AES upon replacing the bridging atom from oxygen to sulfur. The experimentally derived structural parameters for the ground state conformers of AEE and AES revealed that the C-X-C angle is 12º smaller in the latter due to the greater p-orbital character of bonding orbitals on sulfur. More surprising, however, are the distinct orientations of organic side chains in the ether *vs* sulfide species. Based on NBO calculations, this appears to arise from stabilizing orbital interactions involving the lone pair electron density on the bridging atom. For AEE, it is the unique LP(O) donation to the allyl fragment that drives the energy ordering of the lowest conformers, while it is the differences in the LP(S) donation to the ethyl group that define the relative stabilities in AES. The results presented here for AEE and AES highlight the subtle but critically important nature of intramolecular interactions that stabilize distinct geometries of organic ethers and sulfides. The surprising variability in the relative energies and shapes of these organochalcogens reaffirms the role that rotational spectroscopy and quantum chemistry play in informing improved models of bonding, structure, and dynamics that may inspire the design of novel compounds with desirable functional properties.

5.7 References

1 G. C. Hoover and D. S. Seferos, Photoactivity and optical applications of organic materials containing selenium and tellurium, *Chem. Sci.*, 2019, **10**, 9182–9188.

2 I. F. Perepichka, D. F. Perepichka, H. Meng and F. Wudl, Light-emitting polythiophenes, *Adv. Mater.*, 2005, **17**, 2281–2305.

3 Y. Li and Y. Zou, Conjugated polymer photovoltaic materials with broad absorption band and high charge carrier mobility, *Adv. Mater.*, 2008, **20**, 2952–2958.

4 T. P. Kaloni, P. K. Giesbrecht, G. Schreckenbach and M. S. Freund, Polythiophene: From Fundamental Perspectives to Applications, *Chem. Mater.*, 2017, **29**, 10248–10283.

5 M. C. Iovu, E. E. Sheina, R. R. Gil and R. D. McCullough, Experimental evidence for the quasi-"living" nature of the grignard metathesis method for the synthesis of regioregular poly(S-alkylthiophenes), *Macromolecules*, 2005, **38**, 8649–8656.

6 Z. Lou, P. Li and K. Han, Redox-responsive fluorescent probes with different design strategies, *Acc. Chem. Res.*, 2015, **48**, 1358–1368.

7 T. Gneuß, M. J. Leitl, L. H. Finger, N. Rau, H. Yersin and J. Sundermeyer, A new class of luminescent Cu(i) complexes with tripodal ligands-TADF emitters for the yellow to red color range, *Dalt. Trans.*, 2015, **44**, 8506–8520.

8 Y. Yamashita, Organic semiconductors for organic field-effect transistors, *Sci. Technol. Adv. Mater.*, 2009, **10**, 5084–5085.

9 J. G. Manion, J. R. Panchuk and D. S. Seferos, Applying Heteroatom Substitution in Organic Photovoltaics, *Chem. Rec.*, 2019, **19**, 1113–1122.

10 S. Ye, L. Janasz, W. Zajaczkowski, J. G. Manion, A. Mondal, T. Marszalek, D. Andrienko, K. Müllen, W. Pisula and D. S. Seferos, Self-Organization and Charge Transport Properties of Selenium and Tellurium Analogues of Polythiophene, *Macromol. Rapid Commun.*, 2019, **40**, 1800596.

11 E. L. Kynaston, K. J. Winchell, P. Y. Yee, J. G. Manion, A. D. Hendsbee, Y. Li, S. Huettner, S. H. Tolbert and D. S. Seferos, Poly(3-alkylthiophene)- block-poly(3-alkylselenophene)s: Conjugated Diblock Co-polymers with Atypical Self-Assembly Behavior, *ACS Appl. Mater. Interfaces*, 2019, **11**, 7174–7183.

12 M. Jeffries-El, B. M. Kobilka and B. J. Hale, Optimizing the performance of conjugated

polymers in organic photovoltaic cells by traversing group 16, *Macromolecules*, 2014, **47**, 7253–7271.

13 E. L. Kynaston, Y. Fang, J. G. Manion, N. K. Obhi, J. Y. Howe, D. F. Perepichka and D. S. Seferos, Patchy Nanofibers from the Thin Film Self-Assembly of a Conjugated Diblock Copolymer, *Angew. Chemie*, 2017, **129**, 6248–6252.

14 A. Breder and S. Ortgies, Recent developments in sulfur- and selenium-catalyzed oxidative and isohypsic functionalization reactions of alkenes, *Tetrahedron Lett.*, 2015, **56**, 2843–2852.

15 T. Nishiguchi, Y. Yoshikawa and H. Yasui, Anti-diabetic effect of organo-chalcogen (sulfur and selenium) zinc complexes with hydroxy-pyrone derivatives on leptin-deficient type 2 diabetes model ob/ob mice, *Int. J. Mol. Sci.*, 2017, **18**, 2647.

16 D. De Souza, D. O. C. Mariano, F. Nedel, E. Schultze, V. F. Campos, F. Seixas, R. S. Da Silva, T. S. Munchen, V. Ilha, L. Dornelles, A. L. Braga, J. B. T. Rocha, T. Collares and O. E. D. Rodrigues, New organochalcogen multitarget drug: Synthesis and antioxidant and antitumoral activities of chalcogenozidovudine derivatives, *J. Med. Chem.*, 2015, **58**, 3329–3339.

17 F. Penteado, B. Monti, L. Sancineto, G. Perin, R. G. Jacob, C. Santi and E. J. Lenardão, Ultrasound-Assisted Multicomponent Reactions, Organometallic and Organochalcogen Chemistry, *Asian J. Org. Chem.*, 2018, **7**, 2368–2385.

18 P. Oswal, A. Arora, S. Singh, D. Nautiyal, S. Kumar, G. K. Rao and A. Kumar, Organochalcogen ligands in catalysis of oxidation of alcohols and transfer hydrogenation, *Dalt. Trans.*, 2020, **49**, 12503–12529.

19 A. Kirchhain, W. Yu and L. Engman, Organochalcogen stabilizers efficiently protect model

polyolefins exposed to chlorinated media, *Polym. Degrad. Stab.*, 2015, **118**, 82–87.

20 I. C. Mondal, M. Galkin, S. Sharma, N. A. Murugan, D. A. Yushchenko, K. Girdhar, A. Karmakar, P. Mondal, P. Gaur and S. Ghosh, Organosulfur/Selenium-Based Highly Fluorogenic Molecular Probes for Live-Cell Nucleolus Imaging, *Chem. - An Asian J.*, 2022, **17**, e2021012.

21 W. G. D. P. Silva, T. Poonia and J. van Wijngaarden, Targeting the Rich Conformational Landscape of N-Allylmethylamine Using Rotational Spectroscopy and Quantum Mechanical Calculations, *ChemPhysChem*, 2020, **21**, 2515–2522.

22 W. G. D. P. Silva, G. Daudet, S. Perez, S. Thorwirth and J. van Wijngaarden, Conformational preferences of diallylamine: A rotational spectroscopic and theoretical study, *J. Chem. Phys.*, 2021, **154**, 1–25.

23 J. Stitsky, W. G. D. P. Silva, W. Sun and J. Van Wijngaarden, Conformers of Allyl Isothiocyanate: A Combined Microwave Spectroscopy and Computational Study, *J. Phys. Chem. A*, 2020, **124**, 3876–3885.

24 W. G. D. P. Silva, T. Poonia and J. van Wijngaarden, Exploring the non-covalent interactions behind the formation of amine-water complexes: The case of N-allylmethylamine monohydrate, *Phys. Chem. Chem. Phys.*, 2021, **23**, 7368–7375.

25 F. Xie, S. Mahendiran, N. A. Seifert and Y. Xu, Modifying conformational distribution of chiral tetrahydro-2-furoic acid through its interaction with water: a rotational spectroscopic and theoretical investigation, *Phys. Chem. Chem. Phys.*, 2021, **23**, 3820–3825.

26 A. M. Rijs, B. O. Crews, M. S. de Vries, J. S. Hannam, D. A. Leigh, M. Fanti, F. Zerbetto and W. J. Buma, Shaping of a Conformationally Flexible Molecular Structure for Spectroscopy, *Angew. Chemie*, 2008, **120**, 3218–3223.

27 S. R. Domingos, C. Pérez, C. Medcraft, P. Pinacho and M. Schnell, Flexibility unleashed in acyclic monoterpenes: Conformational space of citronellal revealed by broadband rotational spectroscopy, *Phys. Chem. Chem. Phys.*, 2016, **18**, 16682–16689.

28 M. Fatima, D. Maué, C. Pérez, D. S. Tikhonov, D. Bernhard, A. Stamm, C. Medcraft, M. Gerhards and M. Schnell, Structures and internal dynamics of diphenylether and its aggregates with water, *Phys. Chem. Chem. Phys.*, 2020, **22**, 27966–27978.

29 A. Mardyukov, H. Quanz and P. R. Schreiner, Conformer-specific hydrogen atom tunnelling in trifluoromethylhydroxycarbene, *Nat. Chem.*, 2017, **9**, 71–76.

30 C. Cabezas, J. C. Guillemin and Y. Endo, Conformational analysis of ethyl-substituted Criegee intermediate by FTMW spectroscopy, *J. Chem. Phys.*, 2016, **145**, 224314.

31 P. Vansteenkiste, E. Pauwels, V. Van Speybroeck and M. Waroquier, Rules for generating conformers and their relative energies in n-alkanes with a heteroelement O or S: Ethers and alcohols, or sulfides and thiols, *J. Phys. Chem. A*, 2005, **109**, 9617–9626.

32 R. E. Schmidtt and C. R. Quade, Microwave spectrum of ethyl mercaptan, *J. Chem. Phys.*, 1975, **62**, 3864-3874.

33 J. Nakagawa and M. Hayashi, Internal rotation in propyl mercaptan by microwave spectroscopy, *J. Mol. Spectrosc.*, 1981, **85**, 327–340.

34 Y. Kawashima, Y. Tanaka, T. Uzuyama and E. Hirota, Conformations and low-frequency intramolecular motions of 1-butanol, 1-butanethiol, iso-butanol, and iso-butanethiol investigated by fourier transform microwave spectroscopy combined with quantum chemical calculations, *J. Phys. Chem. A*, 2021, **125**, 1166–1183.

35 M. Takano, Y. Sasada and T. Satoh, Microwave spectrum of ethyl alcohol: The trans rotamer, *J. Mol. Spectrosc.*, 1968, **26**, 157–162.

36 A. Maeda, F. C. De Lucia, E. Herbst, J. C. Pearson, J. Riccobono, E. Trosell and R. K. Bohn, The Millimeter- and Submillimeter-Wave Spectrum of the *Gt* Conformer of n-Propanol (n-$CH_3CH_2CH_2OH$) , *Astrophys. J. Suppl. Ser.*, 2006, **162**, 428–435.

37 Z. Kisiel, O. Dorosh, A. Maeda, I. R. Medvedev, F. C. De Lucia, E. Herbst, B. J. Drouin, J. C. Pearson and S. T. Shipman, Determination of precise relative energies of conformers of n-propanol by rotational spectroscopy, *Phys. Chem. Chem. Phys.*, 2010, **12**, 8329–8339.

38 T. Poonia, W. G. D. P. Silva and J. van Wijngaarden, Dramatic differences in the conformational equilibria of chalcogen-bridged compounds: The case of diallyl ether versus diallyl sulfide, *Phys. Chem. Chem. Phys.*, 2022, **24**, 240–248.

39 W. Caminati, A. C. Fantoni, C. Paolucci and B. Velino, Conformational equilibrium in methyl allyl ether, *J. Mol. Spectrosc.*, 1991, **145**, 362–370.

40 A. C. Fantoni, Microwave spectrum, conformation rotation in allyl methyl sulfide, *J. Mol. Struct.*, 1991, **243**, 131–139.

41 P. Cahill, L. Peter Gold and N. L. Owen, Microwave spectrum, conformation, dipole moment, and barrier to internal rotation in methyl vinyl ether, *J. Chem. Phys.*, 1968, **48**, 1620–1626.

42 N. L. Owen and G. O. Sorensen, Microwave Spectrum, Conformation, Internal and Barrier to Rotation of Ethyl Vinyl Ether, *J. Phys. Chem.*, 1979, **83**, 1483-1488.

43 F. Weinhold, C. R. Landis and E. D. Glendening, What is NBO analysis and how is it useful?, *Int. Rev. Phys. Chem.*, 2016, **35**, 399–440.

44 E. R. Johnson, S. Keinan, P. Mori-Sánchez, J. Contreras-García, A. J. Cohen and W. Yang, Revealing noncovalent interactions, *J. Am. Chem. Soc.*, 2010, **132**, 6498–6506.

45 G. G. Brown, B. C. Dian, K. O. Douglass, S. M. Geyer and B. H. Pate, The rotational

spectrum of epifluorohydrin measured by chirped-pulse Fourier transform microwave spectroscopy, *J. Mol. Spectrosc.*, 2006, **238**, 200–212.

46 T. J. Balle and W. H. Flygare, Fabry-Perot cavity pulsed Fourier transform microwave spectrometer with a pulsed nozzle particle source, *Rev. Sci. Instrum.*, 1981, **52**, 33–45.

47 L. Evangelisti, G. Sedo and J. van Wijngaarden, Rotational Spectrum of 1,1,1-Trifluoro-2-butanone Using Chirped-Pulse Fourier Transform Microwave Spectroscopy, *J. Phys. Chem. A*, 2011, **115**, 685–690.

48 G. Sedo and J. van Wijngaarden, Fourier transform microwave spectra of a "new" isomer of OCS-CO_2, *J. Chem. Phys.*, 2009, **131**, 044303.

49 C. Bannwarth, S. Ehlert and S. Grimme, GFN2-xTB–An Accurate and Broadly Parametrized Self-Consistent Tight-Binding Quantum Chemical Method with Multipole Electrostatics and Density-Dependent Dispersion Contributions, *J. Chem. Theory Comput.*, 2019, **15**, 1652–1671.

50 S. Grimme, Exploration of Chemical Compound, Conformer, and Reaction Space with Meta-Dynamics Simulations Based on Tight-Binding Quantum Chemical Calculations, *J. Chem. Theory Comput.*, 2019, **15**, 2847–2862.

51 P. Pracht, F. Bohle and S. Grimme, Automated exploration of the low-energy chemical space with fast quantum chemical methods, *Phys. Chem. Chem. Phys.*, 2020, **22**, 7169–7192.

52 A. D. Becke, A new inhomogeneity parameter in density-functional theory, *J. Chem. Phys.*, 1998, **109**, 2092–2098.

53 S. Grimme, S. Ehrlich and L. Goerigk, Effect of the damping function in dispersion corrected density functional theory, *J. Comput. Chem.*, 2011, **32**, 1456–1465.

54 S. Grimme, J. Antony, S. Ehrlich and H. Krieg, A consistent and accurate ab initio parametrization of density functional dispersion correction (DFT-D) for the 94 elements H-Pu, *J. Chem. Phys.*, 2010, **132**, 1–19.

55 T. H. Dunning, Gaussian basis sets for use in correlated molecular calculations. I. The atoms boron through neon and hydrogen, *J. Chem. Phys.*, 1989, **90**, 1007–1023.

56 M. J. Frisch, G. W. Trucks, H. B. Schlegel, G. E. Scuseria, M. A. Robb, J. R. Cheeseman, G. Scalmani, V. Barone, B. Mennucci, G. A. Petersson, H. Nakatsuji, M. Caricato, X. Li, H. P. Hratchian, A. F. Izmaylov, J. Bloino, G. Zheng, J. L. Sonnenberg, M. Hada, M. Ehara, Fukuda, K. T. R., J. Hasegawa, M. Ishida, T. Nakajima, Y. Honda, O. Kitao, H. Nakai, T. Vreven, J. A. Montgomery, J. E. Peralta, F. Ogliaro, M. Bearpark, J. J. Heyd, E. Brothers, K. N. Kudin, V. N. Staroverov, R. Kobayashi, J. Normand, K. Raghavachari, A. Rendell, J. C. Burant, S. S. Iyengar, J. Tomasi, M. Cossi, N. Rega, J. M. Millam, M. Klene, J. E. Knox, J. B. Cross, V. Bakken, C. Adamo, J. Jaramillo, R. Gomperts, R. E. Stratmann, O. Yazyev, A. J. Austin, R. Cammi, C. Pomelli, J. W. Ochterski, R. L. Martin, K. Morokuma, V. G. Zakrzewski, G. A. Voth, P. Salvador, J. J. Dannenberg, S. Dapprich, A. D. Daniels, Farkas, J. B. Foresman, J. V Ortiz, J. Cioslowski and D. J. Fox, Gaussian 16 (Revision C.01), Gaussian, Inc., Wallingford CT, 2016.

57 J. Contreras-García, E. R. Johnson, S. Keinan, R. Chaudret, J. P. Piquemal, D. N. Beratan and W. Yang, NCIPLOT: A program for plotting noncovalent interaction regions, *J. Chem. Theory Comput.*, 2011, **7**, 625–632.

58 E. D. Glendening, J. K. Badenhoop, A. E. Reed, J. E. Carpenter, J. A. Bohmann, C. M. Morales, P. Karafiloglou, C. R. Landis and F. Weinhold, NBO 7.0., Theoretical Chemistry Institute, University of Wisconsin, Madison, 2018.

59 H. M. Pickett, The fitting and prediction of vibration-rotation spectra with spin interactions, *J. Mol. Spectrosc.*, 1991, **148**, 371–377.

60 J. K. G. Watson, Determination of centrifugal distortion coefficients of asymmetric-top molecules. III. Sextic coefficients, *J. Chem. Phys.*, 1968, **48**, 4517–4524.

61 H. Hartwig and H. Dreizler, The microwave spectrum of trans-2,3-dimethyloxirane in torsional excited states, *Zeitschrift fur Naturforsch. - Sect. A J. Phys. Sci.*, 1996, **51**, 923–932.

62 J. Kraitchman, Determination of Molecular Structure from Microwave Spectroscopic Data, *Am. J. Phys.*, 1953, **21**, 17–24.

63 Z. Kisiel, Spectroscopy from Space, Kluwer Academic Publishers, 2001, 91-106.

64 C. C. Costain, Further comments on the accuracy of r substitution structures, s Trans., *Am. Crystallogr. Assoc.*, 1966, **2**, 157–164.

65 R. S. Ruoff, T. D. Klots, T. Emilsson and H. S. Gutowsky, Relaxation of conformers and isomers in seeded supersonic jets of inert gases, *J. Chem. Phys.*, 1990, **93**, 3142–3150.

Chapter 6. Investigating conformational equilibria in chalcogen-bridged compounds with vinyl and saturated organic substituents: A combined approach of rotational spectroscopy and computational chemistry

6.1 Introduction

In this chapter, we extend our knowledge of the influence of different side chains on the conformational equilibria of chalcogen-containing molecules by studying vinyl-substituted compounds, namely ethyl vinyl ether (EVE), ethyl vinyl sulfide (EVS), propyl vinyl ether (PVE), propyl vinyl sulfide (PVS), butyl vinyl ether (BVE) and butyl vinyl sulfide (BVS). The inclusion of the vinyl (fully unsaturated) group introduces a notable shift by reducing the conformer flexibility compared to previously studied allyl (partially unsaturated) derivatives DAE, DAS (chapter 4), AEE and AES (chapter 5). This transition provides a unique opportunity to explore the impact of interactions with a direct double bond attachment to the chalcogen-bridged atom (O *vs* S) and the role of the saturated side chain length in shaping the conformational landscape.

Microwave spectroscopic investigations of the O- and S-bridged compounds, methyl vinyl ether ($CH_3OCH=CH_2$, MVE)[1] and methyl vinyl sulfide ($CH_3SCH=CH_2$, MVS),[2] reported the observation of one isomer of each having the vinyl group in downward orientation termed cis. Another microwave study of EVE ($CH_3CH_2OCH=CH_2$)[3] and EVS ($CH_3CH_2SCH=CH_2$)[4] highlighted that EVE has a less competitive conformational landscape, with only one identified conformer, while spectral features of EVS were consistent with two conformers. It is worth noting that the geometries of the observed conformers in both EVE and EVS shared similarities. Conformer I of EVE exhibits a sickle-shaped structure, with the vinyl group in the downward position and all heavy atoms are arranged in a co-planar C=COCC framework with the ethyl group in an anti-position, similar to conformer I of EVS. Conformer II of EVS differs from its lower

energy form by the gauche arrangement of the ethyl fragement.[3,4] These observations demonstrated how altering the size of the saturated side chain (transitioning from methyl to ethyl) affects the conformational equilibria. Moreover, a theoretical study of a series of analogs of ethers, alcohols, sulfides and thiols[5] showed that the conformational changes extend up to three dihedral angles away from the central atom, further motivating the exploration of interactions with a variety of saturated side chains.

In this study, our objective is to shed light on the impact of altering saturated fragments on the conformational landscape of chalcogen-bridged compounds (O *vs* S) as they transition from smaller side chains like ethyl to larger counterparts such as propyl and butyl, all while retaining the unsaturated vinyl chain. It is interesting to investigate how the larger side chain increases complexity and makes the conformational equilibrium even more challenging. Additionally, the research seeks to compare these findings with the previously studied allyl derivative molecules (in chapters 4 and 5) to understand general trends in organochalcogenides. Furthermore, the microwave spectroscopic investigation of similar vinyl molecules shows complex splitting patterns due to the barrier associated with the internal rotation of the methyl group at the end of each fragment; for example, in MVE (V_3 =16.03(42) kJ mol^{-1}),[1] MVS (V_3 =13.51 (42) kJ mol^{-1})[2] and EVE (V_3 = 12.85(10) kJ mol^{-1})[3]. Thus, this research also considers the possibility of observing insightful effects from methyl internal rotation as the chain increases in length.

Herein, we report for the first time the rotational spectroscopic investigation of PVE and BVE using Fourier transform microwave (FTMW) spectroscopy, supported by density functional theory (DFT) calculations at the B3LYP-D3(BJ)/aug-cc-pVTZ level. To compare the results with their sulfur analogs, theoretical calculations were performed for EVE, EVS, PVS and BVS using the same level of theory. Theoretical calculations reveal a decrease in the number of low energy

conformers when transitioning from a heavier organochalcogen to a lighter one, within a 5 kJ mol^{-1} energy window. In the present work, we focused solely on investigating the rotational spectrum of the PVE and BVE, due to the commercial unavailability of PVS and BVS and the already published rotational studies on EVE[3] and EVS.[4] The observed rotational spectra exhibited transitions corresponding to two conformers of PVE and four conformers of BVE. Subsequently, the experimental rotational constants of the ^{13}C isotopologues of conformers I of PVE and BVE were used to determine their substitution (r_s) and ground state effective (r_0) geometries. By resolving the A/E splittings in conformers I and II of both PVE and BVE, the three-fold barrier associated with the methyl internal rotor was determined. Analysis of non-covalent interactions (NCI) and natural bond orbitals (NBO) provided valuable insights into the stereoelectronic effects responsible for the unique conformational landscape of EVE, EVS, PVE, PVS, BVE, and BVS, including their conformational preferences and stability.

6.2 Methods

6.2.1 Experimental methods

The rotational spectra of PVE and BVE were investigated using a chirped pulse (cp) and a cavity-based Balle-Flygare (BF) Fourier transform microwave (FTMW) spectrometer that have been previously described.[6,7] The broadband cp-FTMW spectra were collected from the 8-18 GHz frequency range in 2 GHz segments to identify the most intense rotational transitions for the conformers of PVE and BVE. Subsequently, the BF-FTMW instrument was employed to carry out final frequency measurements in the 5-21 GHz frequency range with higher sensitivity and resolution. The transitions recorded with the BF-FTMW spectrometer have linewidths of approximately ~7 kHz (FWHM), enabling accurate determination of the line positions with

uncertainties around ±2 kHz. In the cavity-based instrument, all transitions are split into Doppler doublets due to the collinear arrangement of the resonator axis and the molecular beam.

To investigate the conformers in the laboratory, commercial samples of PVE (99%, purity) and BVE (98%, purity), which are liquids at room temperature and have relatively low boiling points (bp = 65 ^{o}C (lit.) for PVE and bp = 94 ^{o}C (lit.) for BVE), were purchased from Sigma Aldrich, Canada and used without further purification. A gas mixture containing ~1% of either of the compounds seeded in neon (100-200 kPa) was prepared at room temperature. The mixture was then expanded into the high vacuum chambers of the microwave spectrometers using a pulsed nozzle with a 1 mm diameter orifice to generate a supersonic jet expansion.

6.2.2 Computational methods

Conformer-Rotamer Ensemble Sampling Tool (CREST) was employed to carry out a conformational search by generating the possible low-energy conformers of PVE, BVE, PVS and BVS along with the experimental studied EVS[4] and EVE[3] molecules, for comparison. The search was carried out at the semiempirical GFN2-xTB[8] level of theory, available in the extended tight binding (xTB) program package,[9,10] and was performed using a computer code created by Grimme and co-workers.[10] The presence of multiple dihedral angles in the ether and sulfide compounds, as defined in Figures 6.1, 6.2 and 6.3, resulted in a complex conformational landscape due to the rotations around single bonds. Initially, the conformational search identified 5 conformers for both EVE and EVS and 15, 51, 13 and 94 potential geometries for PVE, BVE, PVS and BVS, respectively. All of these possible geometries were then fully optimized using dispersion-corrected density functional theory (DFT) B3LYP[11]-D3(BJ)[12,13] functional with Dunning's aug-cc-pVTZ[14] basis set. Harmonic frequency calculations were also performed for all optimized geometries using

the same level of theory and basis set to obtain the relative energies with zero-point energy corrections (ZPE), to validate the nature of stationary points and to obtain quartic centrifugal distortion constants. Gaussian 16 software[15] was used for optimization and frequency calculations. To estimate the internal rotation barrier (V_3) of the methyl group for PVE and BVE, relaxed potential energy scan calculations were done by varying the C-C-C-H dihedral angle in 36 steps of 10^o each at the same level of theory and the results are shown in Figure 6.4 for conformer I of BVE. To gain a better understanding of the electronic effects and interactions that influence the conformational preferences of ether and sulfur compounds, natural bond orbital (NBO) and non-covalent interaction (NCI) analyses were performed using NBO 7.0[16] and NCIPLOT[17] programs, respectively.

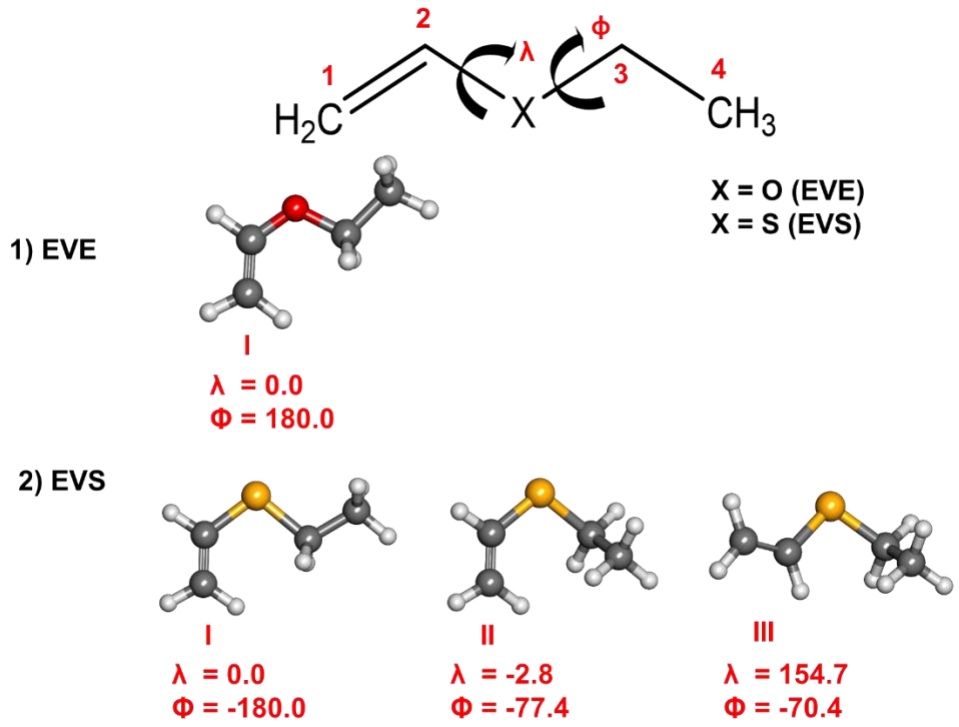

Figure 6.1 Most stable conformers of 1) EVE and 2) EVS within a relative energy window of 5 kJ mol^{-1} obtained at B3LYP-D3(BJ)/aug-cc-pVTZ level of theory which arises due to the rotation around λ, ϕ.

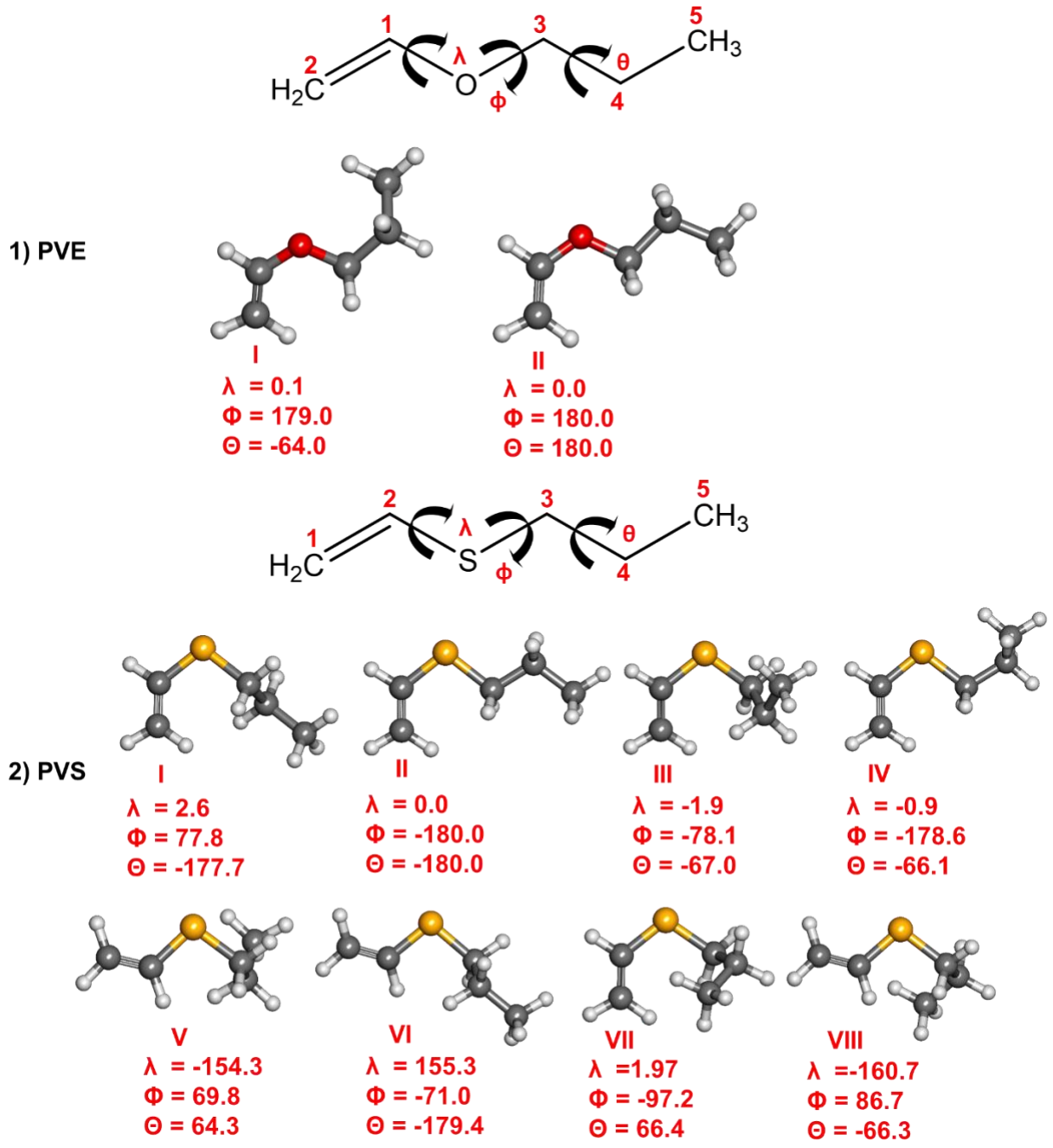

Figure 6.2 Most stable conformers of 1) PVE and 2) PVS within a relative energy window of 5 kJ mol^{-1} obtained at B3LYP-D3(BJ)/aug-cc-pVTZ level of theory which arises due to the rotation around λ, ϕ and θ.

X = O (BVE)
X = S (BVS)

1) BVE

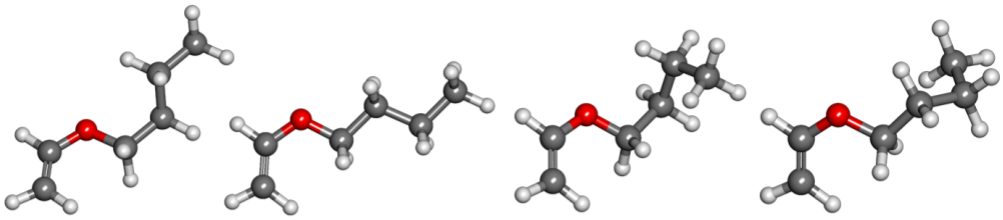

I
λ = - 0.1
Φ = -179.1
Θ = 64.8
δ = 179.9

II
λ = 0.0
Φ = 180.0
Θ = -180.0
δ = -180.0

III
λ = -0.4
Φ = -178.8
Θ = 60.6
δ = 61.9

IV
λ = 0.4
Φ = 179.5
Θ = 176.4
δ = 65.1

2) BVS

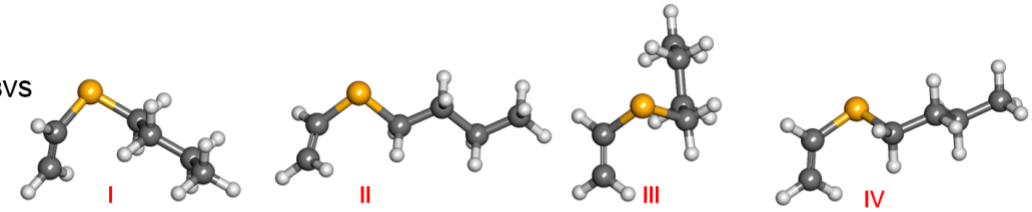

I
λ = - 2.4
Φ = -77.5
Θ = 177.0
δ = 179.2

II
λ = 0.0
Φ = 180.0
Θ = -180.0
δ = 180.0

III
λ = 1.8
Φ = 78.0
Θ = 68.2
δ = -179.2

IV
λ = -1.1
Φ = -177.8
Θ = -66.2
δ = -177.3

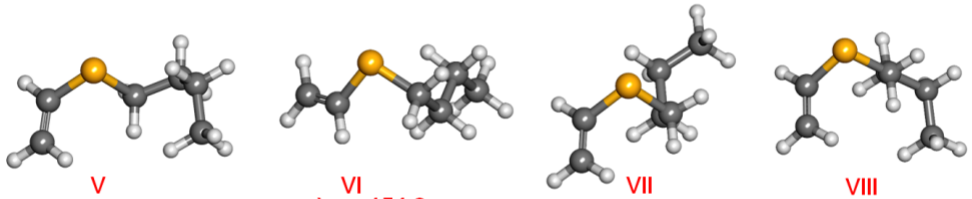

V
λ = 0.6
Φ = 178.6
Θ = 60.8
δ = 57.9

VI
λ = -154.2
Φ = 69.5
Θ = 65.1
δ = -180.0

VII
λ = 2.5
Φ = 77.4
Θ = 61.5
δ = 61.5

VIII
λ = 2.5
Φ = 78.4
Θ = -177.3
δ = 69.0

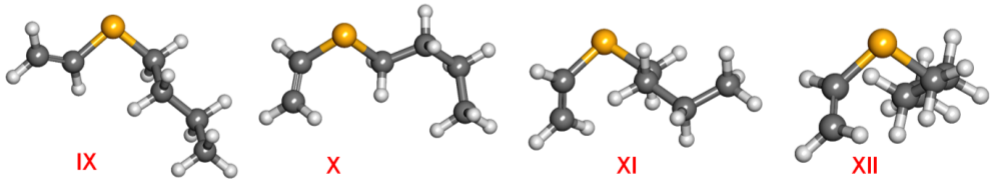

IX
λ = 155.3
Φ = -70.8
Θ = -179.5
δ = -180.0

X
λ = -0.5
Φ = -178.9
Θ = -176.7
δ = -64.5

XI
λ = -2.8
Φ = -77.0
Θ = 174.0
δ = 64.0

XII
λ = -2.0
Φ = 97.0
Θ = -67.1
δ = 177.4

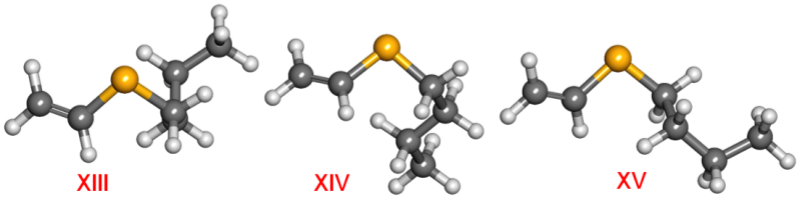

XIII
λ = -154.0
Φ = 67.2
Θ = 59.0
δ = 60.1

XIV
λ = -160.3
Φ = 86.4
Θ = -67.0
δ = -178.0

XV
λ = 155.2
Φ = -70.0
Θ = 178.1
δ = 65.1

Figure 6.3 Most stable conformers of 1) BVE and 2) BVS within a relative energy window of 5 kJ mol^{-1} obtained at B3LYP-D3(BJ)/aug-cc-pVTZ level of theory which arises due to the rotation around λ, ϕ, θ and δ.

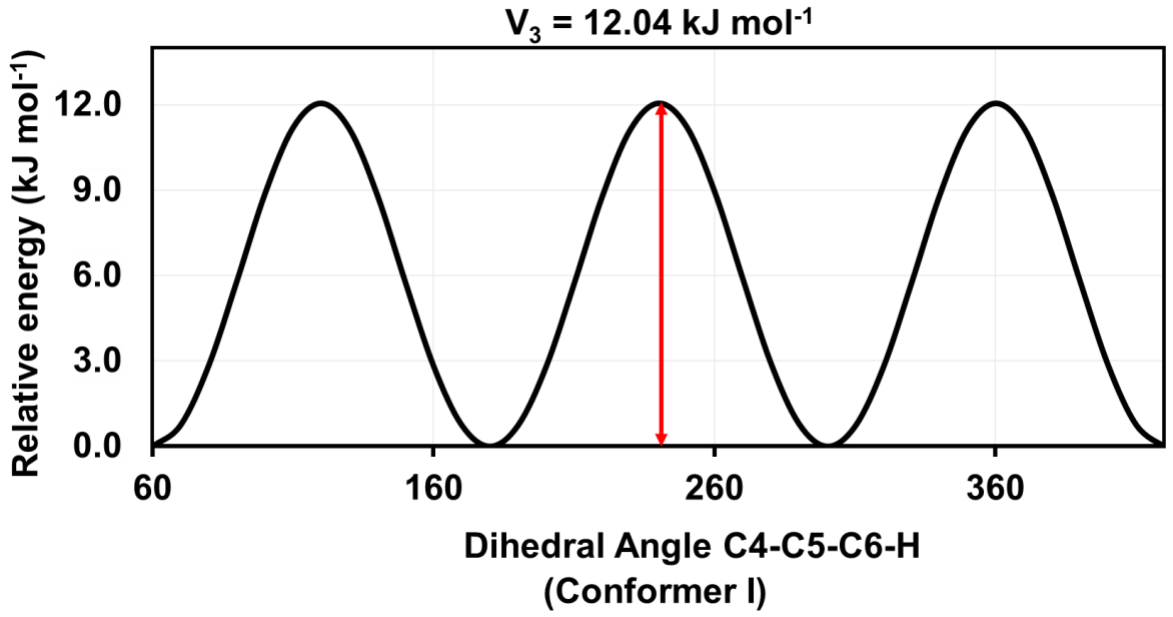

Figure 6.4 Energy scan of methyl internal rotations of BVE conformer I at B3LYP_D3(BJ)/aug-cc-pVTZ level of theory. The V_3 barrier for conformers II-IV was determined to be 12.01 kJ mol^{-1}, 11.32 kJ mol^{-1} and 10.84 kJ mol^{-1}, respectively. For PVE conformer I, V_3 was 11.1 kJ mol^{-1} and 11.0 kJ mol^{-1} for conformer II.

6.3 Results

6.3.1 Conformational space

The quantum chemical calculations predicted a diverse conformational landscape for both ether and sulfide compounds. Geometry optimization calculations resulted in 4 conformers for both EVE and EVS within 7.9 kJ mol^{-1} and 5.3 kJ mol^{-1}, respectively (Table 6.1), 10 unique geometries for PVE within 10.4 kJ mol^{-1} and 11 for PVS within 6.6 kJ mol^{-1} (Table 6.2) and 27 and 30 for BVE and BVS within 16.6 kJ mol^{-1} and 13.6 kJ mol^{-1}, respectively (Table 6.3). Also, moving from the saturated ethyl side chain to propyl to butyl leads to a significant increase in the

number of conformers due to the presence of an additional dihedral for each methylene group added, namely θ in the case of PVE and PVS (Figure 6.2), and δ in BVE and BVS (Figure 6.3), to the two dihedral angles, λ and ϕ, needed to describe the orientation of sidechains within the ethyl vinyl compounds (Figure 6.1).The spectroscopic parameters and the relative energies obtained using the B3LYP-D3(BJ)/aug-cc-pVTZ methods for EVE and EVS, PVE and PVS, and BVE and BVS conformers are provided in Tables 6.1, 6.2 and 6.3, respectively. In addition, the Cartesian coordinates for these compounds are given in the electronic supplementary information (ESI) in Tables S1-86. At room temperature, the concentrations of the higher energy conformers are not expected to be sufficient for spectroscopic detection, and consequently, conformers with relative energies below 5 kJ mol^{-1} were considered for further observation. For EVE, EVS, PVE, PVS, BVE and BVS, the theoretical calculations revealed that the sulfide compounds have a more competitive conformational landscape compared to the ethers. This is seen from the occurrence of 1 low energy conformer for EVE (within 5 kJ mol^{-1} energy window), as compared to 3 conformers for EVS (Table 6.1), 2 conformers for PVE and 8 for PVS, and 4 conformers for BVE and 15 for BVS, as shown in Tables 6.2 and 6.3, respectively. Figures 6.1-6.3 shows pictorial representations of the ether and sulfur compounds within this relative energy range. Roman numerals were used to label the conformers based on their B3LYP-D3(BJ)/aug-cc-pVTZ order of stability, with conformer I as the most stable conformer among others.

Table 6.1 Calculated energetic and spectroscopic parameters for the conformers of EVS and EVE at the B3LYP-D3(BJ)/aug-cc-pVTZ level of theory.

EVE	ΔE_0[a]	P[b]	A/B/C[c]	$\lvert\mu_a\rvert$/ $\lvert\mu_b\rvert$/ $\lvert\mu_c\rvert$[d]
I	0.0	82.2	16586/2802/2470	0.7/0.8/0.0
II	5.8	7.9	9278/3682/3032	0.9/0.6/0.4

III	6.3	6.4	24240/2361/2211	1.3/1.3/0.0
IV	7.9	3.4	13962/2771/2571	1.5/0.4/1.0

EVS	ΔE_0[a]	P[b]	A/B/C[c]	$\lvert\mu_a\rvert$/ $\lvert\mu_b\rvert$/ $\lvert\mu_c\rvert$[d]
I	0.0	44.9	8824/2346/1897	0.6/1.1/0.0
II	0.7	34.5	5413/3164/2237	0.8/1.0/0.4
III	2.7	15.2	7421/2393/2007	1.1/1.0/0.7
IV	5.3	5.3	15922/1847/1706	0.9/1.4/0.0

[a]Zero-point energy (ZPE) corrected relative energies in kJ mol^{-1}, [b]Boltzmann population at 298K in %,), [c]Rotational constants in MHz, [d]Magnitude of the electric dipole moment components in Debye.

Table 6.2 Calculated energetic and spectroscopic parameters for the conformers of PVE and PVS at the B3LYP-D3(BJ)/aug-cc-pVTZ level of theory.

PVE	ΔE_0[a]	P[b]	A/B/C[c]	$\lvert\mu_a\rvert$/ $\lvert\mu_b\rvert$/ $\lvert\mu_c\rvert$[d]
I	0.0	42.3	9988/1737/1627	0.6/0.8/0.2
II	0.3	36.7	11299/1581/1423	0.9/0.6/0.0
III	5.5	4.6	6664/2103/2009	0.7/0.7/0.5
IV	5.7	4.2	7418/1952/1697	1.1/0.4/0.2
V	6.3	3.3	9862/1643/1510	1.1/1.1/0.7
VI	6.8	2.8	19862/1327/1273	1.4/1.1/0.0
VII	7.1	2.4	6904/1977/1774	1.3/0.7/1.1
VIII	7.8	1.8	11571/1522/1448	1.7/0.4/0.8
IX	8.8	1.2	6575/2112/1756	1.6/0.0/1.0
X	10.4	0.6	5525/2519/2021	0.9/0.1/0.6

PVS	ΔE_0[a]	P[b]	A/B/C[c]	$\lvert\mu_a\rvert$/ $\lvert\mu_b\rvert$/ $\lvert\mu_c\rvert$[d]
I	0.0	20.2	4562/1684/1328	1.2/0.6/0.2

II	0.1	19.3	6456/1350/1140	1.0/0.9/0.0
III	0.2	18.4	4482/1789/1519	0.7/1.0/0.5
IV	1.1	12.8	6747/1441/1294	0.6/1.1/0.0
V	2.1	8.8	4787/1588/1453	1.0/0.5/1.2
VI	2.3	7.9	5922/1355/1183	1.4/0.9/0.5
VII	4.0	3.9	3747/2131/1591	1.0/0.5/0.7
VIII	4.2	3.7	4312/1847/1423	1.3/0.6/0.8
IX	5.6	2.1	11874/1088/1022	1.2/1.2/0.0
X	6.5	1.5	9208/1250/1169	0.8/1.3/0.5
XI	6.6	1.4	9390/1233/1179	0.9/1.3/0.5

[a]Zero-point energy (ZPE) corrected relative energies in kJ mol^{-1}, [b]Boltzmann population at 298K in %,), [c]Rotational constants in MHz, [d]Magnitude of the electric dipole moment components in Debye.

Table 6.3 Calculated energetic and spectroscopic parameters for the conformers of BVE and BVS at the B3LYP-D3(BJ)/aug-cc-pVTZ level of theory.

BVE	ΔE_0 [a]	P [b]	A/B/C [c]	$\lvert\mu_a\rvert$/ $\lvert\mu_b\rvert$/ $\lvert\mu_c\rvert$ [d]
I	0.0	30.4	8946/1026/981	0.5 /0.7/0.2
II	0.7	23.2	10581/926/869	1.0/0.7/0.0
III	2.0	13.7	5437/1269/1207	0.6/0.2/0.7
IV	3.6	7.2	6392/1111/1001	1.1/0.4/0.3
V	5.4	3.4	5453/1348/1182	0.5/0.8/0.3
VI	5.5	3.4	5095/1274/1210	0.7/0.0/0.8
VII	6.0	2.7	5861/1151/1047	1.1/0.2/0.4
VIII	6.4	2.3	7269/1025/945	0.8/1.3/0.6
IX	7.1	1.8	4680/1280/1114	1.1/0.8/1.0
X	7.1	1.7	15166/826/799	1.4/1.3/0.0

XI	7.6	1.4	5598/1365/1305	0.6/0.7/0.4
XII	8.2	1.1	7603/971/909	1.8/0.0/0.9
XIII	8.4	1.0	5333/1222/1130	1.1/0.6/1.1
XIV	8.7	0.9	4814/1386/1190	1.3/0.2/0.0
XV	8.7	0.9	4441/1348/1111	1.4/0.5/1.1
XVI	9.1	0.8	4995/1330/1251	1.0/1.1/0.9
XVII	9.2	0.7	6361/1206/1100	1.1/0.5/0.2
XVIII	10.0	0.5	4333/1467/1235	0.8/0.1/0.7
XIX	10.1	0.5	4347/1570/1442	0.5/0.9/0.3
XX	10.2	0.5	9761/935/889	1.6/0.8/0.6
XXI	10.7	0.4	3885/1599/1308	1.7/0.0/0.7
XXII	11.2	0.3	6970/1048/1015	1.9/0.6/0.1
XXIII	11.3	0.3	9219/997/953	1.7/0.7/0.8
XXIV	11.5	0.3	4831/1377/1138	0.8/1.3/0.6
XXV	11.6	0.3	3908/1693/1341	1.1/1.1/0.9
XXVI	12.2	0.2	3633/1838/1410	1.0/1.0/0.4
XXVII	16.6	0.0	3450/1927/1535	0.7/0.4/0.7

BVS	ΔE_0[a]	P[b]	A/B/C[c]	$\lvert\mu_a\rvert/\lvert\mu_b\rvert/\lvert\mu_c\rvert$[d]
I	0.0	12.6	3919/986/852	1.3 /0.4/0.4
II	0.0	12.4	6240/793/716	1.0/1.0/0.0
III	0.1	12.0	3625/1073/975	0.8/0.6/0.7
IV	0.9	8.9	6409/862/806	0.6/1.1/0.1
V	2.1	5.3	4216/1037/1014	0.7/0.7/0.7
VI	2.1	5.3	3425/1061/931	1.0/0.0/1.2

VII	2.2	5.3	4080/1147/1024	0.6/1.0/0.4
VIII	2.4	4.8	3460/1175/954	1.4/0.3/0.0
IX	2.5	4.6	4378/865/767	1.6/0.5/0.8
X	2.5	4.5	4345/943/815	1.2/0.7/0.3
XI	2.6	4.4	4157/1032/885	1.2/0.8/0.2
XII	3.5	3.0	3103/1246/1027	0.9/0.2/0.8
XIII	3.7	2.8	3881/1084/1042	0.8/0.5/1.3
XIV	3.9	2.6	3075/1199/936	1.3/0.0/1.0
XV	4.9	1.7	5447/870/790	1.4/1.0/0.6
XVI	5.2	1.5	4170/938/847	1.7/0.7/0.1
XVII	5.6	1.3	10848/680/653	1.2/1.3/0.0
XVIII	5.8	1.2	2784/1452/1079	1.5/0.3/0.5
XIX	6.2	1.0	7804/789/747	0.7/1.3/0.5
XX	6.4	0.9	7933/783/751	0.8/1.3/0.5
XXI	7.2	0.7	2831/1508/1112	1.2/0.1/0.4
XXII	7.6	0.6	4950/952/899	0.8/0.7/1.2
XXIII	7.8	0.5	3550/1233/1092	0.7/1.1/0.2
XXIV	7.9	0.5	4502/1064/954	0.6/1.1/0.3
XXV	8.1	0.5	6679/780/726	1.4/1.0/0.4
XXVI	8.2	0.5	6524/778/729	1.4/1.0/0.6
XXVII	10.6	0.2	2828/1423/1149	1.0/0.3/1.3
XXVIII	12.7	0.1	2631/1593/1152	1.2/0.0/1.1
XXIX	12.9	0.1	5152/980/867	0.7/1.4/0.5
XXX	13.6	0.1	5281/967/865	0.8/1.4/0.6

[a]Zero-point energy (ZPE) corrected relative energies in kJ mol^{-1}, [b]Boltzmann population at 298K in %,), [c]Rotational constants in MHz, [d]Magnitude of the electric dipole moment components in Debye.

6.3.2 Spectral analysis

With no prior accounts of the microwave spectra of PVE and BVE to guide us, we turned to the information presented in Tables 6.2 and 6.3 to search for species in our experimental spectra. Knowing that the rotational transition intensity in molecules intrinsically depends on the dipole moment components along the principal inertial axes, as well as the population of rotational energy levels, we focused our spectral assignment on identifying rotational transitions of the most stable geometries of each molecule first. By comparing the experimental cp-FTMW spectra with the simulated spectra that were generated using the PGOPHER program,[18] we successfully assigned the first two conformers of PVE and first four conformers of BVE. Figure 6.5 shows a portion of the broadband cp-FTMW spectrum in a region with transitions from the four conformers of BVE. The spectral intensities were sufficient for the lowest energy conformer I to also observe transitions from naturally occurring singly-substituted ^{13}C isotopologues of both PVE and BVE. For PVE, this included assigning features to all five ^{13}C isotopologues while for BVE, patterns were identified for all six minor species with spectral intensities of ~1% those of the corresponding parent lines.

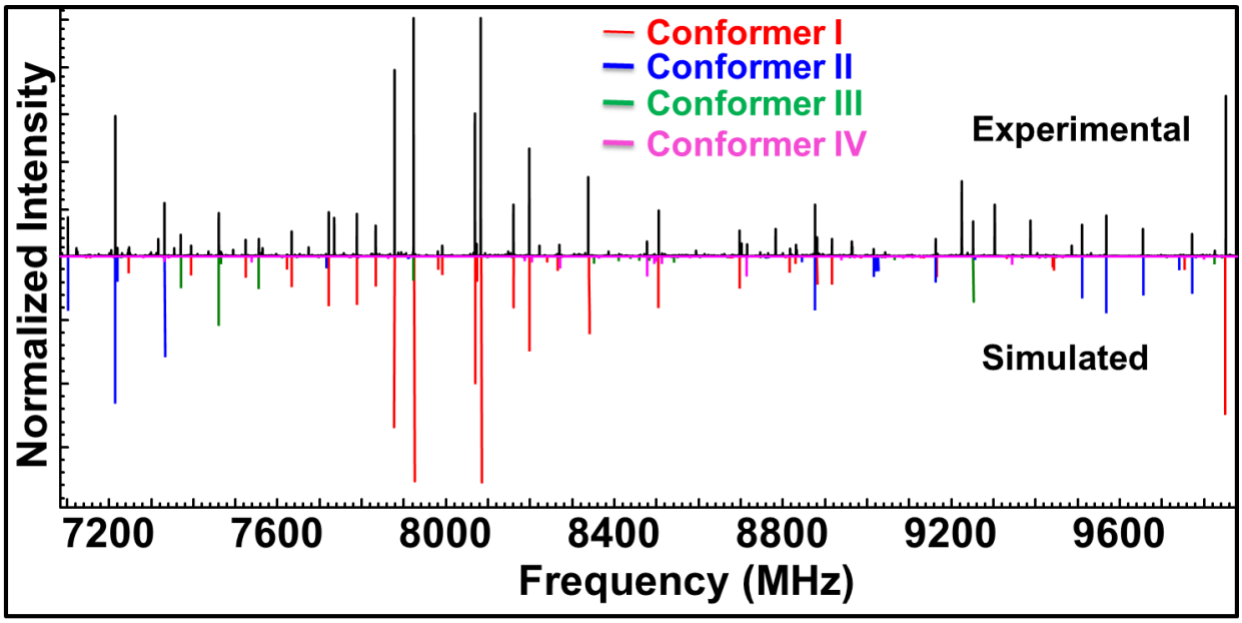

Figure 6.5 Portion of the broadband cp-FTMW spectrum (1.5 million free induction decays) of BVE for observed conformers I-IV. The top portion is the experimental spectrum and the lower is the simulated spectrum using the fitted parameters.

The rotational transitions for all conformers of the ether were then re-measured using the higher resolution and higher sensitivity BF-FTMW spectrometer. These measurements confirmed the preliminary assignments done by cp-FTMW spectrometer and additional lower intensity transitions were also recorded to expand the frequency coverage. No experimental transitions were measured for PVS and BVS, as they are not commercially available, nor for EVE and EVS, as these compounds have already been investigated through microwave spectroscopy in previous studies.[3,4] While collecting transitions in the high-resolution spectra, a splitting pattern was observed in certain transitions of conformers I and II of PVE and BVE. For these splitting patterns, we considered the internal rotation of the methyl group and successfully fit these individual components to the A/E states of the methyl internal rotor. This is consistent with the splitting patterns observed in the conformers of AEE,[19] corresponding to transitions involving energy levels

with similar K_a' values. Figure 6.6 displays a sample splitting pattern observed in the spectrum. It is noteworthy that no splitting was observed for conformers III and IV of BVE even though they have similar V_3 barrier and this might be attributed to the orientation of the methyl rotor within these specific conformers.[20]

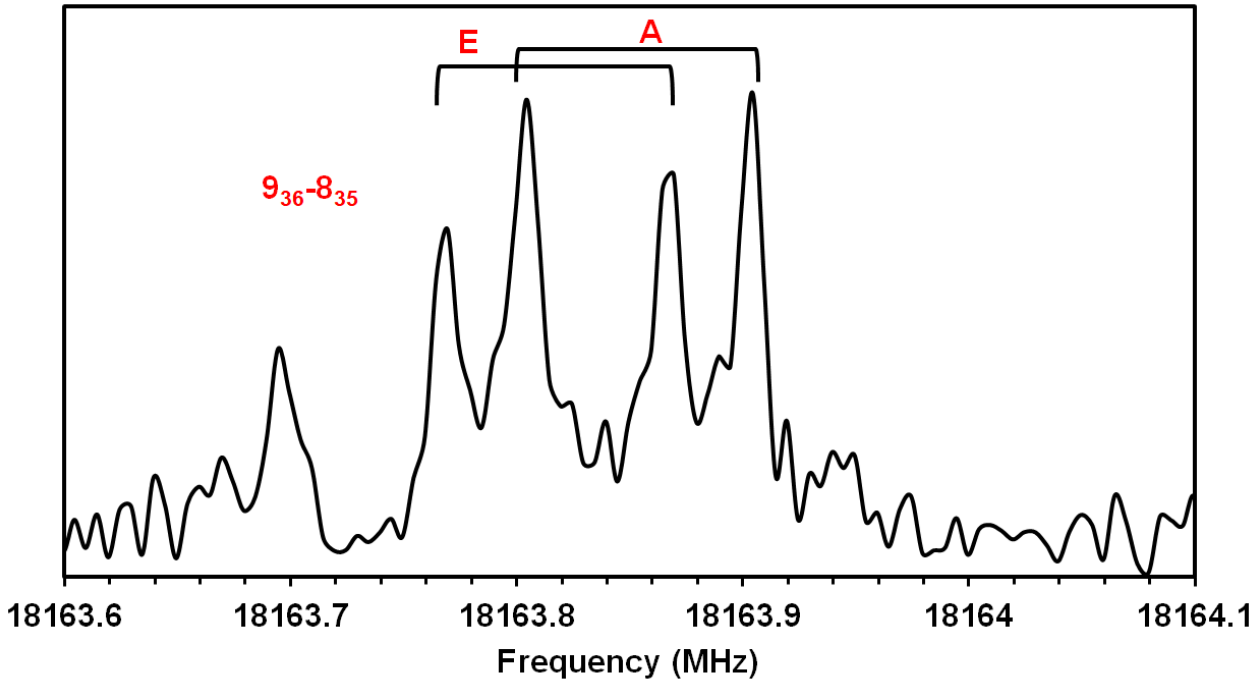

Figure 6.6 A sample of BF-FTMW spectrum showing A/E splitting pattern due to the methyl internal rotation in BVE conformer I in addition to the Doppler splitting of the instrument.

For conformers I and II of PVE and BVE, the spectrum showed splitting patterns due to methyl internal rotation, therefore the transitions were analyzed using the XIAM program,[21] which incorporates the combined axis method (CAM) to effectively handle this type of motion. This software is well-suited for cases with relatively high barriers, such as those encountered in this study, and facilitates the determination of crucial parameters for both molecules. To achieve this,

the theoretical geometry obtained from the B3LYP-D3(BJ)/aug-cc-pVTZ level of theory was used to derive values for the angle between the rotor's a-axis and the principal inertial a-axis of the molecule (α) and the rotational constant of the methyl top (F_0). For conformers and isotopologues, where no splitting was seen, the rotational transitions were fitted with Watson's A-reduced Hamiltonian in the I^r representation[22] using Pickett's SPFIT program[23] to yield experimental rotational and quartic centrifugal distortion constants. The obtained experimental parameters are presented in Tables 6.4, 6.5 and 6.6. The complete line lists of the observed transitions are given in the electronic supplementary information in Tables S89-105. The experimental results exhibit a strong agreement with the corresponding theoretical parameters provided in Tables S87 and S88. including, for example, the barriers for methyl internal rotation in conformers I (V_3 = 12.004(87) kJ mol^{-1} and II (V_3 = 11.308(25) kJ mol^{-1}) of PVE, as well as conformers I (V_3 = 12.232(61) kJ mol^{-1} and II (V_3 =12.443(32) kJ mol^{-1}) of BVE, as mentioned in Figure 6.4. These findings provide further evidence to support the claim that the observed splitting patterns are due to the methyl internal rotation, a phenomenon also observed in related molecules like methyl vinyl ether (V_3 = 16.03(42) kJ mol^{-1})[1] and ethyl vinyl ether (V_3 = 12.85(10) kJ mol^{-1})[3] and allyl ethyl ether (conformer I, V_3 =12.172(55) kJ mol^{-1} and conformer II, V_3 = 12.373(32) kJ mol^{-1}).[19]

Table 6.4 Experimental spectroscopic parameters of PVE for conformer I including its ^{13}C isotopologues and conformer II.

Parameter	XIAM	SPFIT					XIAM
	Conformer I	$^{13}C1$	$^{13}C2$	$^{13}C3$	$^{13}C4$	$^{13}C5$	Conformer II
A/MHz[a]	9871.13004(42)	9817.24635(81)	9806.10324(54)	9777.20340(76)	9790.91544(46)	9776.66648(37)	11085.03336(84)
B/MHz	1748.4260(13)	1710.58626(19)	1730.70591(13)	1748.10447(18)	1729.81739(10)	1712.631360(81)	1591.64463(16)
C/MHz	1636.8422(13)	1603.69458(14)	1619.72001(10)	1633.96106(14)	1619.595420(78)	1605.152180(64)	1429.76108(14)
Δ_J/kHz[b]	0.4089(23)	0.3932(30)	0.4001(21)	0.4046(28)	0.3903(16)	0.4041(12)	0.1671(13)
Δ_{JK}/kHz	-3.758(15)	-3.759(25)	-3.660(18)	-3.713(24)	-3.474(14)	-3.952(11)	--2.3657(55)
Δ_K/kHz	[62.552]	[62.551839]	[62.552]	[62.551839]	[62.551839]	[62.551839]	[41.297]
δ_J/kHz	0.00949(26)	[0.009491]	[0.00949]	[0.009491]	[0.009491]	[0.009491]	0.02961(69)
δ_K/kHz	5.86(62)	[5.856433]	[5.86]	[5.856433]	[5.856433]	[5.856433]	[0.356]
V_3 (kJ/mol)	12.004(87)						11.308(25)
F0 (GHz)	[161.262]						[161.625]
Δ (rad)	[2.038]						[2.425]
$\mu_a/\mu_b/\mu_c$[c]	y/y/y	y/y/n	y/y/y	y/y/n	y/y/n	y/y/y	y/y/n
N_d	126	30	33	30	29	31	102

σ/kHz[e]	2.7	1.9	1.4	1.8	1.0	0.9	3.7

[a]Rotational constants; [b]quartic centrifugal distortion constants; [c]electric dipole moment components ("y" if observed and "n" if not observed); [d]total number of lines (*N*) in the fit; [e]root-mean-square deviation of the fit (σ). For conformer I and II the values in the brackets were fixed to the values derived from theoretical molecular geometry obtained at the B3LYP-D3(BJ)/aug-cc-pVTZ level of theory and to the predicted values obtained at the same level of theory. The value in brackets for the isotopes were fixed to the conformer I values. A complete list of the calculated rotational parameters at the B3LYP-D3(BJ)/aug-cc-pVTZ is given in Table S87.

Table 6.5 Experimental spectroscopic parameters of BVE for conformer I including its ^{13}C isotopologues.

Parameter	XIAM	SPFIT					
	Conformer I	$^{13}C1$	$^{13}C2$	$^{13}C3$	$^{13}C4$	$^{13}C5$	$^{13}C6$
A/MHz[a]	8864.62082(44)	8830.5018(34)	8798.7386(13)	8774.47865(84)	8762.6366(23)	8821.8926(29)	8849.5490(36)
B/MHz	1031.392373(42)	1011.3861(28)	1020.8789(10)	1031.16867(69)	1028.5521(19)	1023.4979(24)	1007.9611(30)
C/MHz	986.414698(42)	968.32340(99)	976.05382(37)	985.08337(25)	983.06047(68)	979.38782(86)	964.7984(11)
Δ_J/kHz[b]	0.12865(19)	[0.12865]	[0.12865]	[0.12865]	[0.12865]	[0.12865]	[0.12865]
Δ_{JK}/kHz	-3.7590(23)	[-3.7590]	[-3.7590]	[-3.7590]	[-3.7590]	[-3.7590]	[-3.7590]
Δ_K/kHz	71.02(10)	[71.02]	[71.02]	[71.02]	[71.02]	[71.02]	[71.02]
δ_J/kHz	0.006476(48)	[0.006476]	[0.006476]	[0.006476]	[0.006476]	[0.006476]	[0.006476]
δ_K/kHz	[1.366]	[1.366]	[1.366]	[1.366]	[1.366]	[1.366]	[1.366]
V_3 (kJ/mol)	12.232(61)						

Fo (GHz)	[161.625]						
α (rad)	[2.425]						
$\mu_a/\mu_b/\mu_c$[c]	y/y/y	n/y/n	n/y/n	n/y/n	n/y/n	n/y/n	n/y/n
N_d	212	7	7	7	7	7	7
σ/kHz[e]	2.9	2.1	0 .8	0.5	1.5	1.9	2.3

[a]Rotational constants; [b]quartic centrifugal distortion constants; [c]electric dipole moment components ("y" if observed and "n" if not observed); [d]total number of lines (*N*) in the fit; [e]root-mean-square deviation of the fit (σ). For conformer I the values in the brackets were fixed to the values derived from theoretical molecular geometry obtained at the B3LYP-D3(BJ)/aug-cc-pVTZ level of theory and to the predicted values obtained at the same level of theory. The value in brackets for the isotopes were fixed to the conformer I values. A complete list of the calculated rotational parameters at the B3LYP-D3(BJ)/aug-cc-pVTZ is given in Table S88.

Table 6.6 Experimental spectroscopic parameters of BVE for conformer II-III.

Parameter	XIAM	SPFIT	
	Conformer II	Conformer III	Conformer IV
A/MHz[a]	10384.43650(44)	5427.63217(67)	6325.180(35)
B/MHz	930.786018(66)	1274.790850(85)	1117.53640(48)
C/MHz	873.350040(50)	1212.845821(69)	1006.40431(47)
Δ_J/kHz[b]	0.03942(24)	0.84204(72)	0.1899(11)

Δ_{JK}/kHz	-0.6042(14)	-4.4278(32)	-1.9850(78)
Δ_K/kHz	[24.584]	31.74(14)	[19.864]
δ_J/kHz	0.00503(24)	0.15498(47)	0.04881(60)
δ_K/kHz	[-0.002]	[0.835]	1.45(23)
V_3 (kJ/mol)	12.443(32)		
Fo (GHz)	[161.450]		
α (rad)	[2.691]		
$\mu_a/\mu_b/\mu_c$[c]	y/y/n	y/y/y	y/y/n
N_d	162	52	29
σ/kHz[e]	2.3	1.2	0.9

[a]Rotational constants; [b]quartic centrifugal distortion constants; [c]electric dipole moment components ("y" if observed and "n" if not observed); [d]total number of lines (*N*) in the fit; [e]root-mean-square deviation of the fit (σ). For conformer II the values in the brackets were fixed to the values derived from theoretical molecular geometry obtained at the B3LYP-D3(BJ)/aug-cc-pVTZ level of theory and to the predicted values obtained at the same level of theory. For conformer III and IV to the predicted values obtained at the same level of theory. A complete list of the calculated rotational parameters at the B3LYP-D3(BJ)/aug-cc-pVTZ is given in Table S88.

6.3.3 Structure determination

The internal coordinates involving the heavy atoms of PVE and BVE were determined using experimental rotational constants obtained from the rotational spectra of five and six ^{13}C isotopic species of their ground state conformer I, respectively. These rotational constants are given in Tables 6.4 and 6.5. Initially, the substitution structures (r_s) were obtained by applying Kraitchman's equations[24] through Kisiel's KRA program.[25] The absolute values of the Kraitchman coordinates of the isotopically substituted atoms were determined, and their signs were then inferred by comparing them with the equilibrium geometry (r_e) parameters obtained at the B3LYP-D3(BJ)/aug-cc-pVTZ level of theory. The resulting values are provided in the ESI in Table S106. Subsequently, the atomic coordinates and their corresponding Costain errors[26] were used to calculate the r_s geometry parameters using the EVAL routine.[25] The calculated results for both molecules are summarized in Tables 6.7 and 6.8. A limited number of parameters were derived for PVE and BVE due to the insufficient signal intensity to observe ^{18}O transitions, however, it is noteworthy that all the derived structural values for PVE and BVE, except for the r(C3-C4) parameter of PVE, fall within two standard deviations of the r_e values. The discrepancy in the r(C3-C4) parameter of PVE can be attributed to the imprecise determination of the c-coordinate value -0.01741 ± 0.08627 Å of C3, shown in Table S106.

Next, for PVE and BVE, the effective ground state geometries (r_0) were obtain using Kisiel's STRFIT program.[25] This program performs a least-squares fit of the selected geometric parameters to the moments of inertia of all observed isotopologues. In the fitting process, all 18 rotational constants for the six isotoplogoues were used for PVE, while 21 rotational constants were available for BVE due to the additional ^{13}C species observed in the larger species. For both molecules, the internal coordinates involving the hydrogen atoms were fixed to the values obtained

at the B3LYP-D3(BJ)/aug-cc-pVTZ level of theory. The resulting r_0 parameters matched well with the theoretical r_e values and are given in Tables 6.7 and 6.8.

Upon further analysis of Tables 6.7 and 6.8, it becomes apparent that the derived geometric parameters for conformers I of PVE and BVE are quite analogous. The same result is predicted for conformers I of PVS and BVS based on the equilibrium r_e parameters obtained at the same theoretical level of theory as outlined in Table S107. By comparing the theoretical geometric parameters of the sulfide molecules with the ethers, it is clear that the C-O-C angle in PVE and BVE is nearly 14^o greater than the C-S-C angle in PVS and BVS, which aligns with theoretical geometry obtained at the same level of theory for EVE and EVS (Table S107), and also with the observations from DAE[27] and DAS[27] (chapter 4), as well as AEE[19] and AES[19] (chapter 5). This is in agreement with the hybridizations of the bridging atom (O or S) determined from the NBO analysis, where C-S bonding orbitals demonstrate a higher p-character on sulfur (81.19%-83.75% for EVS, 81.19%-83.29% for PVS and 81.19%-83.35% for BVS) compared to oxygen (67.70%-71.66 % for EVE, 67.68%-71.44% for PVE and 67.71%-71.46% for BVE).

Table 6.7 Equilibrium (r_e) (B3LYP/aug-cc-pVTZ), substitution (r_s), ground state effective (r_0) structural parameters (bond lengths in Å, angles in deg) determined for PVE.

	r_e	r_s	r_0
C1-C2	1.332	1.337(6)	1.341(6)
C1-O	1.351	-	1.358(8)
O-C3	1.428	-	1.427(7)
C3-C4	1.515	1.549(20)	1.516(8)
C4-C5	1.526	1.527(4)	1.532(3)

∠C3-C4-C5	113.4	112.8(2.2)	112.8(1)
∠ C1-O-C3	117.4	-	116.4(9)
∠O-C1-C2	128.2	-	128.0(6)
∠O-C3-C4	108.5	-	108.0(6)

Table 6.8 Equilibrium (r_e) (B3LYP/aug-cc-pVTZ), substitution (r_s), ground state effective (r_0) structural parameters (bond lengths in Å, angles in deg) determined for BVE.

	r_e	r_s	r_0
C1-C2	1.332	1.335(7)	1.344(5)
C2-O	1.351	-	1.337(8)
O-C3	1.428	-	1.445(8)
C3-C4	1.515	1.482(26)	1.489(9)
C4-C5	1.527	1.529(5)	1.534(4)
C5-C6	1.526	1.531(6)	1.529(3)
∠C3-C4-C5	113.8	112.7(27)	113.4(1)
∠C4-C5-C6	112.6	112.4(7)	112.1(4)
∠C3-C4-C5-C6	179.9	178.9(30)	179.6(6)
∠ C2-O-C3	117.4	-	117.9(9)
∠O-C2-C1	128.2	-	127.9(6)
∠O-C4-C5	108.5	-	109.4(6)

6.4 Discussion

The quantum chemical calculations for the ether (EVE, PVE and BVE) and sulfide (EVS, PVS and BVS) vinyl compounds reveal unique features in their conformational landscapes. Notably, the sulfide vinyl compounds exhibit a more competitive (as the conformers are more closely spaced in terms of relative energy) and rich conformational equilibrium compared to the ethers, as shown in Tables 6.1-6.3. These observation highlight striking differences from the recent microwave studies involving the diallyl compounds[27] (chapter 4), as well as the AEE[19] and AES[19] allyl compounds (chapter 5). These previous studies revealed that the lighter congener (O-bridged) demonstrates a more competitive equilibrium compared to the heavier counterpart (S-bridged). Furthermore, the key finding upon moving from DAS and AES was that the inclusion of a saturated ethyl group enabled the S-bridged compound to exist as a mixture of three conformers, contrasting with the detection of only one conformer in the case of DAS. This trend remains consistent with the inclusion of saturated ethyl, propyl and butyl side chains in the S-bridged vinyl compound such as EVS, PVS and BVS, respectively. These compounds demonstrated a notable increase in the number of conformers as the length of the saturated fragment increases. As a result, the incorporation of the unsaturated vinyl fragment along with diverse saturated side chains provides us with an opportunity to understand the impact they exert on the conformational space.

The predicted geometries of the most stable conformers of ethers highlight a consistent downward orientation of the vinyl fragment (λ) for all conformers lying within a 5 kJ mol^{-1} energy window of the global minimum. Moreover, there are similarities in the arrangements of the saturated ethyl (ϕ) or propyl (ϕ and θ) or butyl (ϕ, θ and δ) side chains, as seen in conformer I of EVE, PVE, and BVE, as well as for conformer II of PVE and BVE with the only difference arising from the extra dihedral angle, as shown in Figures 6.1-6.3. It is worth noting that the higher energy

conformers have an upward direction of the vinyl fragment (λ) to form a V-shape in the case of EVE and for the majority of the higher energy conformers in PVE and BVE. In contrast, for the sulfur compounds EVS, PVS and BVS, a combination of downward (for conformers I and II of EVS, I-IV and VII of PVS, and I-V, VII, VIII and X-XII of BVS) and V-shape (for conformer III of EVS, V, VI and VIII of PVS, and VI, IX, XIII-XV of BVS) orientations of the vinyl fragment are observed within a 5 kJ mol^{-1} energy window of the global minimum, with variations in the ethyl and propyl and butyl side chains, respectively, as depicted in Figures 6.1-6.3. Additionally, the geometry of conformer I of EVS is analogous to EVE conformer I while for the longer side chains, the most stable conformers of the sulfide do not resemble those of their ether analogs. This suggests that stabilizing interactions differ sufficiently to re-order the relative energies of the stable conformers when there is more flexibility as in these longer chain species. The global minimum geometries of PVS and BVS are similar, having a gauche arrangement of ϕ (rather than anti in EVS), as illustrated in Figures 6.2 and 6.3 and table S107. Overall, the conformer geometries moving from EVS to PVS to BVS display more differences when compared with the ethers. This underscores the importance of understanding the influence of unique interactions involving the different side chains and chalcogens that contribute to molecular stability and structural arrangement.

To investigate the underlying non-covalent interactions contributing to the distinctive conformers of ether and sulfide compounds, and energy ordering, NCI and NBO analyses were performed. The NCI analysis (Figure 6.7) illustrates the presence of attractive forces represented by blue-green isosurfaces in the most stables conformers of EVE, PVE and BVE between the π bond of the vinyl fragment (C-H--- π) and a C-H bond of the first methylene group in the ethyl or propyl or butyl fragment closest to oxygen. Notably, these C-H--- π interactions resemble those

reported in the lowest energy conformations of DAA,[28] DADS,[29] and DAE[27] and may be the origin of the stability of these conformers. It is important to note that alongside these attractive interactions, however, there are also repulsive interactions (red regions) of similar magnitudes due to the formation of five-membered ring during the establishment of intramolecular contacts. Visually, the stability of conformer I of PVE and BVE can be further rationalized by the presence of an additional weak interaction (green isosurface) between the lone pair of oxygen, LP(O) and the third methylene group of the propyl or butyl side chains, which is consistent with the interactions observed up to three dihedral angles away in the theoretical studies of n-alkane-substituted alcohols.[5] For EVS, PVS and BVS (Figures S1), one must be cautious in interpreting the NCI isosurfaces due to the predominance of green-colored isosurfaces indicating weak interaction that can be due to the net attractive or repulsive interactions between different atoms or bonds. Therefore, NBO analysis, which involves the calculations of second-order perturbation energies related to orbital interactions, can offer valuable molecular-level insights. This analysis can help identify the interactions between occupied and empty orbitals, shedding light on the underlying factors influencing the stability of different conformers.

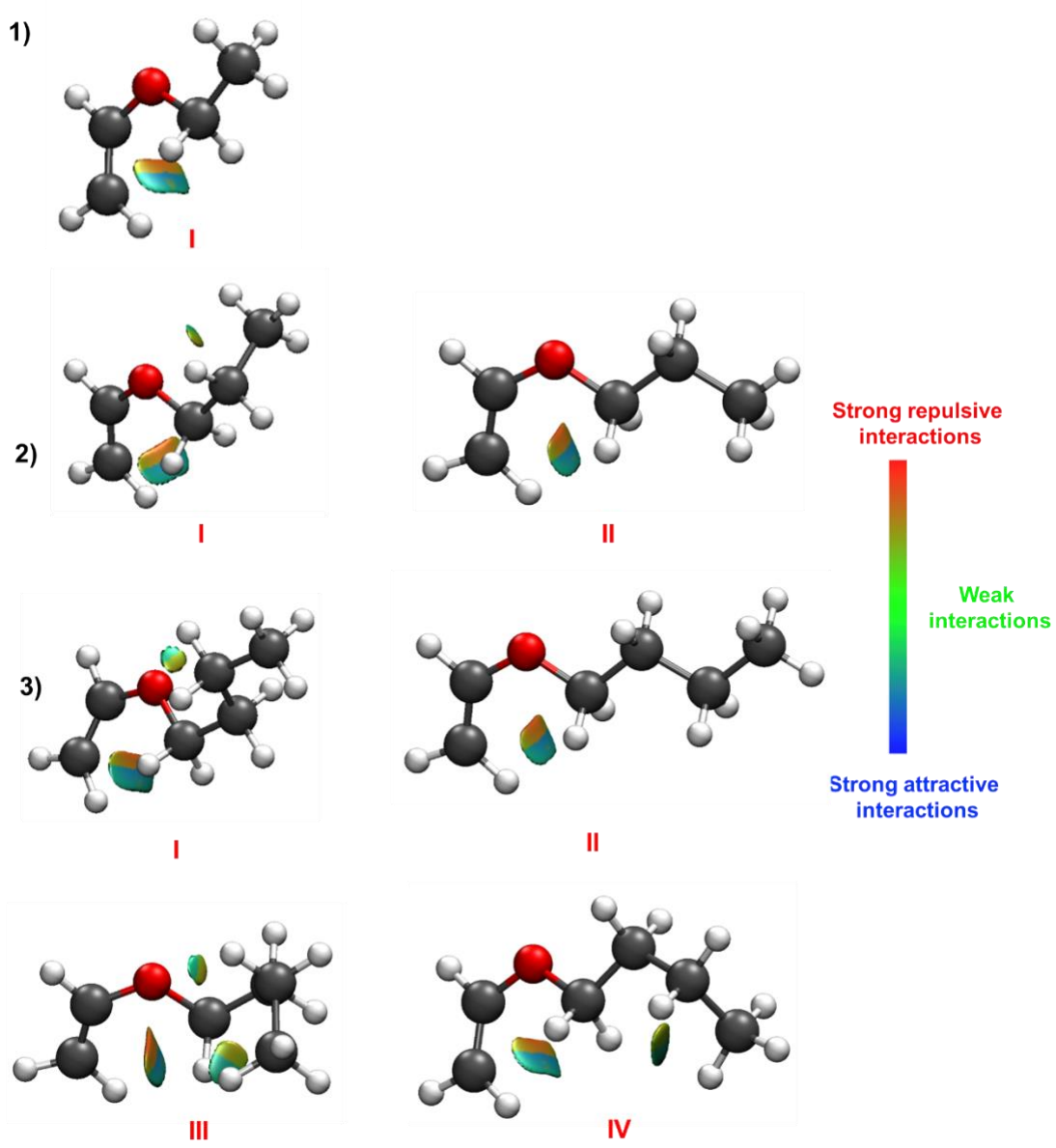

Figure 6.7 NCI isosurfaces (s = 0.05, color scale for -0.02 < ρ < + 0.02 au) for A) PVE conformers I and II and B) for conformers I-IV of BVE.

Surprisingly, the NBO calculations did not reveal any evidence of C-H---π and the LP(O)---methylene (LP(O)---CH_5) interactions and instead highlighted the significant role of charge transfer interactions between the LP of the chalcogen atom and the antibonding π* orbitals of the downward-pointing vinyl fragment, which plays a notable role in in stabilizing the observed low

energy conformers of EVE, PVE, BVE, EVS, PVS, and BVS. This analysis revealed that the downward orientation of the vinyl fragment (Figures 6.1-6.3) in the lowest energy conformers of ether and sulfur compounds is influenced by charge transfer interactions between the lone pair (LP) of the chalcogen bridged atom and the π* orbital of the vinyl fragment as compiled in Table 6.9 (EVE, PVE, BVE) and in Tables S108 and S109 for the sulfides. This is consistent with the explanation provided in the earlier microwave spectroscopy study of conformer I of EVE[3] that the coplanar arrangement of heavy atoms with vinyl group oriented downward not only minimizes steric hindrance but also the sp^2 hybridization of the oxygen atom facilitates better overlap of its lone pair electron density with the neighboring carbon-carbon double bond. Similarly, in the case of EVS[4], the most stable geometry also features analogous orientations of the side chains which matches the results of our NBO analysis. Therefore, this interaction seems to be responsible for the most stable geometries in the ether and sulfide compounds. However, for the sulfide compounds, in some conformers such as conformer III of EVS, V, VI and VIII of PVS, and VI, IX, XIII-XV of BVS, the vinyl fragment adopts a V-shaped orientation which is less stable as the LP(S) → $\pi^*C_1–C_2$ interaction is about half the magnitude compared to the downward orientation. This is counteracted to some extent as the LP on sulfur is shared with the σ* orbital of C_1-C_2 and C_2–H interactions for the V-shaped vinyl orientation which provide some additional stability to make these conformers more energetically competitive than in the case of the ethers. However, it is important to note that the interactions that involve the LP of the central chalcogen atom (O or S) and the saturated side chains (ethyl or propyl or butyl) include many competitive and subtle effects, therefore it becomes challenging to single out a specific interaction accountable for the observed stability, as demonstrated in Tables 6.9 and S105 and S106.

Table 6.9 Select second-order perturbation energy for conformers of EVE, PVE and BVE within 5 kJ mol^{-1} energy window, highlighting charge transfer interactions that involve the lone pair (LP) on oxygen, as well as interactions between bonds in the case of BVE. Figures 6.1-6.3 displays the labels for the atomic numbers.

EVE	Conformer I
Interaction	E (kJ/mol)
LP1(O) → σ*C1–C2	27.36
LP2(O) → σ*C1–C2	-
LP1(O) → σ*C2–H	11.17
LP2(O) → σ*C2–H	-
LP2(O) → π*C1–C2	148.99
LP1(O) → π*C1–C2	-
LP1(O) → σ*C3–H	2.93
LP1(O) → σ*C3–H'	2.93
LP1(O) → σ*C3–C4	5.40
LP2(O) → σ*C3–C4	-
LP2(O) → σ*C3–H	24.35
LP2(O) → σ*C3–H'	24.35
LP2(O) → σ*C4–H	2.72

PVE	Conformer I	Conformer II
Interaction	E (kJ/mol)	E (kJ/mol)
LP1(O) → σ*C1–C2	27.24	27.41

LP2(O) → π*C1–C2	148.78	149.16
LP1(O) → σ*C2–H	11.38	11.25
LP1(O) → σ*C3–C4	5.61	5.90
LP1(O) → σ*C3–H	2.64	3.05
LP1(O) → σ*C3–H'	3.18	3.05
LP2(O) → σ*C3–H	24.56	24.89
LP2(O) → σ*C3–H'	24.23	24.89
LP1(O) → σ*C4–C5	-	2.72
LP1(O) → σ*C4–H'	2.43	-

BVE	Conformer I	Conformer II	Conformer III	Conformer IV
Interaction	E (kJ/mol)	E (kJ/mol)	E (kJ/mol)	E (kJ/mol)
LP1(O) → σ*C1–C2	27.15	27.32	27.28	27.36
LP2(O) → π*C1–C2	148.95	149.33	148.99	149.49
LP1(O) → σ*C2–H	11.38	11.30	11.38	11.30
LP1(O) → σ*C3–C4	5.27	5.56	5.44	5.44
LP1(O) → σ*C4–H	2.59	-	2.64	-
LP1(O) → σ*C3–H	3.10	2.97	3.26	2.89
LP1(O) → σ*C3–H'	2.59	2.97	2.55	3.05
LP2(O) → σ*C3–H	24.18	24.81	23.68	25.27
LP2(O) → σ*C3–H'	24.56	24.81	25.02	23.93

LP1(O) → σ*C4–C5	-	2.55	-	2.51
σC5–C6 → σ*C3–C4	9.1	8.2	-	-
σC5–C6 → σ*C4–H’	-	-	6.7	6.7

Upon closer examination of BVE, it becomes apparent that conformers I and II (having the heavy atoms of the butyl fragment arranged in a plane) exhibit very similar energies, while conformers III and IV have slightly higher relative energy (a few kJ mol^{-1} difference shown in Table 6.3). This could be due to the presence of an interaction involving the hydrocarbon tail as shown in Table 6.9, where the bonding orbital of the C_5-C_6 bond interacts with the antibonding orbital of C_3-C_4 bond ($\sigma C_5–C_6 \rightarrow \sigma^* C_3–C_4$) in conformers I and II, which is absent in the case of conformers III and IV. The presence of a smaller interaction involving the $\sigma C_5–C_6 \rightarrow \sigma^* C_4–H$’ in conformers III and IV (not found in conformers I and II) contributes to their stability and may explain why these arrangements are only a few kJ mol^{-1} higher than the others. For BVS, the stable conformers also display small energy differences making it hard to give a specific reason as these discrepancies can be due to several factors, such as the presence of V-shape or downward orientation of vinyl fragment as well as the other interactions involving the saturated groups as shown in Table S109.

A recent microwave study of AEE[19] and AES[19] indicated that it is the interactions involving the LP on oxygen and the allyl fragment that influence the relative energies of the conformers while in the sulfide, the LP donation to the saturated ethyl chain govern the relative stabilities of conformers. However, for the EVE, EVS, PVE, PVS, BVE and BVS, the orientation of the vinyl fragment is most important in defining the overall energy ordering and the stabilities are then

further influenced by various subtle interactions present within the saturated side chains or between these groups and the chalcogen LP.

The observed differences in the conformational landscape of ethers and sulfides compounds can be further rationalized by considering steric repulsion, which is evaluated through NBO analysis using the STERIC keyword and is presented in Table S110. This analysis provides the steric exchange energy (E_{SE}), approximated as the energy difference between ‘‘preorthogonal’’ and final natural bond orbitals (NBOs), similar to the well-established concept of steric repulsion.[30] This reveals that conformers containing oxygen generally experience higher steric effects, leading to greater destabilization of conformers compared to the sulfur analogs. For example, conformer II of EVE (relative energy 5.8 kJ mol^{-1}) has a steric effect of 692.8 kJ mol^{-1} compared to 667.4 kJ mol^{-1} of conformer II of EVS (relative energy 0.7 kJ mol^{-1}), as indicated in ESI in Table S110. The reduced steric effect in sulfur compounds is likely due to the smaller C-S-C angle (~14º) compared to the C-O-C angle which is a result of the greater p-character on sulfur (for example, 81.19%-83.75% for EVS and 67.70%-71.66 % for EVE). These steric considerations could be responsible for the competitive conformational landscape for the S-bridged compounds with saturated side chains compared to their ether counterparts.

6.5 Conclusions

The rotational spectra of PVE and BVE were obtained using Fourier transform microwave spectroscopy and transitions corresponding to the two most stable conformers of PVE and four for BVE were assigned. In the high-resolution spectra, splitting patterns for conformers I and II of PVE and BVE were observed due to the internal rotation of the methyl group. By fitting these patterns, the V_3 barriers were determined, and their values were found to be in good agreement

with the theoretical estimates. Comparing the experimentally derived structural parameters for the ground state conformer of PVE and BVE with the theoretical parameters of PVS and BVS revealed that the C-S-C angle is approximately 14^{o} smaller and has a greater p-orbital character than the C-O-C angle. Quantum chemical calculations were also conducted to investigate the conformational equilibria of EVE, EVS, PVS, and BVS, aiming to compare the changes in the conformational space, and these results showed that increasing the length of the saturated side chain increases the richness and competitiveness of conformational equilibria of S-bridged compounds compared to ethers. Based on NBO analysis, we identified the role of the vinyl fragment position in governing the energy ordering and highlighted the intricate interplay of interactions involving the saturated side chain that give rise to competitive equilibria for the conformers of ether and sulfide compounds. Moreover, NBO steric analysis indicated that the difference in conformational landscapes arises from more pronounced steric repulsion in the ether molecules compared to the sulfur-containing analogs, potentially leading to greater constraint on the rotation of the saturated side chain in the ethers. These findings underscore the complexity of the conformational landscape, dynamics, and geometries of organochalcogen compounds. This study provides valuable insights contributing to the better development of the organometallic and main group compounds.

6.6 References

1 P. Cahill, L. Peter Gold and N. L. Owen, Microwave spectrum, conformation, dipole moment, and barrier to internal rotation in methyl vinyl ether, *J. Chem. Phys.*, 1968, **48**, 1620–1626.

2 R. E. Penn and R. F. Curl, Microwave spectrum of methyl vinyl sulfide, *J. Mol. Spectrosc.*, 1967, **24**, 235–243.

3 N. L. Owen and G. O. Sorensen, Microwave Spectrum, Conformation, Internal and Barrier to Rotation of Ethyl Vinyl Ether, *J. Phys. Chem.*, 1979, **83**, 1483–1488.

4 K. M. Marstokk and H. Mollendal, A microwave and Ab initio study of the conformational propertis of ethyl vinyl sulfide, *Acta Chem. Scand.*, 1990, **44**, 692–697.

5 P. Vansteenkiste, E. Pauwels, V. Van Speybroeck and M. Waroquier, Rules for generating conformers and their relative energies in n-alkanes with a heteroelement O or S: Ethers and alcohols, or sulfides and thiols, *J. Phys. Chem. A*, 2005, **109**, 9617–9626.

6 L. Evangelisti, G. Sedo and J. van Wijngaarden, Rotational Spectrum of 1,1,1-Trifluoro-2-butanone Using Chirped-Pulse Fourier Transform Microwave Spectroscopy, *J. Phys. Chem. A*, 2011, **115**, 685–690.

7 G. Sedo and J. van Wijngaarden, Fourier transform microwave spectra of a “new” isomer of OCS-CO_2, *J. Chem. Phys.*, 2009, **131**, 044303.

8 C. Bannwarth, S. Ehlert and S. Grimme, GFN2-xTB - An Accurate and Broadly Parametrized Self-Consistent Tight-Binding Quantum Chemical Method with Multipole Electrostatics and Density-Dependent Dispersion Contributions, *J. Chem. Theory Comput.*, 2019, **15**, 1652–1671.

9 S. Grimme, Exploration of Chemical Compound, Conformer, and Reaction Space with Meta-Dynamics Simulations Based on Tight-Binding Quantum Chemical Calculations, *J. Chem. Theory Comput.*, 2019, **15**, 2847–2862.

10 P. Pracht, F. Bohle and S. Grimme, Automated exploration of the low-energy chemical space with fast quantum chemical methods, *Phys. Chem. Chem. Phys.*, 2020, **22**, 7169–7192.

11 A. D. Becke, A new inhomogeneity parameter in density-functional theory, *J. Chem. Phys.*,

1998, **109**, 2092–2098.

12 S. Grimme, S. Ehrlich and L. Goerigk, Effect of the damping function in dispersion corrected density functional theory, *J. Comput. Chem.*, 2011, **32**, 1456–1465.

13 S. Grimme, J. Antony, S. Ehrlich and H. Krieg, A consistent and accurate *ab initio* parametrization of density functional dispersion correction (DFT-D) for the 94 elements H-Pu, *J. Chem. Phys.*, 2010, **132**, 1–19.

14 T. H. Dunning, Gaussian basis sets for use in correlated molecular calculations. I. The atoms boron through neon and hydrogen, *J. Chem. Phys.*, 1989, **90**, 1007–1023.

15 M. J. Frisch, G. W. Trucks, H. B. Schlegel, G. E. Scuseria, M. A. Robb, J. R. Cheeseman, G. Scalmani, V. Barone, B. Mennucci, G. A. Petersson, H. Nakatsuji, M. Caricato, X. Li, H. P. Hratchian, A. F. Izmaylov, J. Bloino, G. Zheng, J. L. Sonnenberg, M. Hada, M. Ehara, Fukuda, K. T. R., J. Hasegawa, M. Ishida, T. Nakajima, Y. Honda, O. Kitao, H. Nakai, T. Vreven, J. A. Montgomery, J. E. Peralta, F. Ogliaro, M. Bearpark, J. J. Heyd, E. Brothers, K. N. Kudin, V. N. Staroverov, R. Kobayashi, J. Normand, K. Raghavachari, A. Rendell, J. C. Burant, S. S. Iyengar, J. Tomasi, M. Cossi, N. Rega, J. M. Millam, M. Klene, J. E. Knox, J. B. Cross, V. Bakken, C. Adamo, J. Jaramillo, R. Gomperts, R. E. Stratmann, O. Yazyev, A. J. Austin, R. Cammi, C. Pomelli, J. W. Ochterski, R. L. Martin, K. Morokuma, V. G. Zakrzewski, G. A. Voth, P. Salvador, J. J. Dannenberg, S. Dapprich, A. D. Daniels, Farkas, J. B. Foresman, J. V Ortiz, J. Cioslowski and D. J. Fox, Gaussian 16 (Revision C.01), Gaussian, Inc., Wallingford CT, 2016.

16 E. D. Glendening, J. K. Badenhoop, A. E. Reed, J. E. Carpenter, J. A. Bohmann, C. M. Morales, P. Karafiloglou, C. R. Landis and F. Weinhold, *NBO 7.0*, Theoretical Chemistry Institute, University of Wisconsin, Madison, 2018.

17 J. Contreras-García, E. R. Johnson, S. Keinan, R. Chaudret, J. P. Piquemal, D. N. Beratan and W. Yang, NCIPLOT: A program for plotting noncovalent interaction regions, *J. Chem. Theory Comput.*, 2011, **7**, 625–632.

18 C. M. Western, PGOPHER: A program for simulating rotational, vibrational and electronic spectra, *J. Quant. Spectrosc. Radiat. Transf.*, 2017, **186**, 221–242.

19 T. Poonia and J. Van Wijngaarden, Exploring the distinct conformational preferences of allyl ethyl ether and allyl ethyl sulfide using rotational spectroscopy and computational chemistry, 2023, **158**, 224301.

20 L. H. Spangler, Structural information from methyl internal rotation spectroscopy, *Annu. Rev. Phys. Chem.*, 1997, **48**, 481–510.

21 H. Hartwig and H. Dreizler, The microwave spectrum of trans-2,3-dimethyloxirane in torsional excited states, *Zeitschrift fur Naturforsch. - Sect. A J. Phys. Sci.*, 1996, **51**, 923–932.

22 J. K. G. Watson, Determination of centrifugal distortion coefficients of asymmetric-top molecules. III. Sextic coefficients, *J. Chem. Phys.*, 1968, **48**, 4517–4524.

23 H. M. Pickett, The fitting and prediction of vibration-rotation spectra with spin interactions, *J. Mol. Spectrosc.*, 1991, **148**, 371–377.

24 J. Kraitchman, Determination of Molecular Structure from Microwave Spectroscopic Data, *Am. J. Phys.*, 1953, **21**, 17–24.

25 Z. Kisiel, *Spectroscopy from Space*, Kluwer Academic Publishers, 2001, 91–106.

26 C. C. Costain, Further Comments on the Accuracy of R Substitution Structures, *Trans. Am. Crystallogr. Assoc.*, 1966, **2**, 157–164.

27 T. Poonia, W. G. D. P. Silva and J. van Wijngaarden, Dramatic differences in the

conformational equilibria of chalcogen-bridged compounds: The case of diallyl ether versus diallyl sulfide, *Phys. Chem. Chem. Phys.*, 2022, **24**, 240–248.

28 W. G. D. P. Silva, G. Daudet, S. Perez, S. Thorwirth and J. van Wijngaarden, Conformational preferences of diallylamine: A rotational spectroscopic and theoretical study, *J. Chem. Phys.*, 2021, **154**, 1–25.

29 J. Demaison, N. Vogt, R. T. Saragi, M. Juanes, H. D. Rudolph and A. Lesarri, How flexible is the disulfide linker? A combined rotational-computational investigation of diallyl disulfide, *Phys. Chem. Chem. Phys.*, 2019, **21**, 19732–19736.

30 P. A. Christiansen and W. E. Palke, Effects of exchange energy and orbital orthogonality on barriers to internal rotation, *J. Chem. Phys.*, 1977, **67**, 57–63.

Chapter 7. Exploring the conformational landscape, hydrogen bonding and internal dynamics in the monohydrates of diallyl ether and diallyl sulfide monohydrates

In continuation of the conformational study of DAE and DAS presented in Chapter 4, this chapter explores their monohydrated complexes, DAE-w and DAS-w. The main objective here is to investigate the influence of microsolvation on flexible compounds, considering their broader range of conformer distributions, as existing literature primarily focuses on cyclic monohydrates of oxygen and sulfur. The aim is to provide crucial insights into how the presence of a water molecule impacts the conformer distribution of the monomer systems through changes to non-covalent intramolecular interactions. The analysis showed that the DAE-w conformers displayed significant changes in their relative energies compared to the DAS-w. However, the ground state geometry for both conformers does not change upon binding with water. Theoretical calculations revealed that most stable monohydrate geometries are stabilized by the presence of two intermolecular hydrogen bonds (HBs) with water. Also, we observed spectral features consistent with sulfur's weaker HB acceptor character compared with the oxygen compound through observation of large amplitude motions in DAS-w resulting in a tunneling splitting in contrast to DAE-w.

7.1 Abstract

The conformational spaces of the diallyl ether (DAE) and diallyl sulfide (DAS) monohydrates were explored using rotational spectroscopy from 6-19 GHz. Although calculations at the B3LYP-D3(BJ)/aug-cc-pVTZ level suggested significant differences in their conformational behaviour, with DAE-w exhibiting 22 unique conformers and DAS-w featuring three stable

structures within 6 kJ mol^{-1}, only transitions from the lowest energy conformer of each were experimentally observed. Spectral analysis confirmed that binding with water does not alter the conformational preference for the lowest energy structure of the monomers, however, it does influence the relative stabilities of all other conformers, particularly in the case of DAE. Interestingly, we also detected tunneling splittings in the spectrum of DAS-w, which were absent in the spectrum of DAE-w. Non-covalent interaction (NCI) and quantum theory of atoms in molecules (QTAIM) analyses showed that the observed conformer for each complex is stabilized by two intermolecular hydrogen bonds (HBs), where water primarily interacts with the central oxygen or sulfur atom of the diallyl compounds, along with secondary interactions involving the allyl groups. The nature of these interactions was further elucidated using symmetry-adapted perturbation (SAPT) theory which suggests that the primary HB interaction with S in DAS is weaker and more dispersive in nature compared to the primary HB in DAE. This supports the observation of a tunneling splitting exclusively in DAS-w as the weaker contact allows water to undergo internal motions within the complex as shown based on calculated transition state structures for possible tunneling pathways.

7.2 Introduction

The omnipresence of water in nature and its ability to influence the structure and reactivity of molecules in chemistry and biology has long been of great interest to researchers.[1–5] The ability of water to stabilize the different geometries of highly flexible molecules through formation of intermolecular contacts is central to understanding solvation processes at the molecular level and can be probed experimentally using high resolution spectroscopic techniques. This is particularly true within the Fourier transform microwave spectroscopy community, given the power of this

technique to precisely differentiate the unique conformations of molecules and their complexes with partner molecules (e.g., water) in a step-wise fashion in a cold molecular beam.[6–10] From a fundamental perspective, investigating microsolvated complexes as prototypes of solvation allows us to explore the correlation between the nature of non-covalent interactions and molecular dynamics (e.g., quantum tunneling, large amplitude motions) on the microscopic scale.[11–17] Hydrogen bonding (HB) emerges as the most dominant and indispensable non-covalent interaction responsible for stabilizing molecules and their complexes.[18–26]

HBs involving oxygen and sulfur have garnered considerable interest due to their influence on the structure and function of proteins, including protein hydration, self-assembly, and overall folding.[27–30] Despite their importance, however, sulfur HBs are still not well-characterized at the molecular level compared with their oxygen analogues.[31,32] A few exceptions include, for example, recent studies on monohydrated complexes of furfuryl mercaptan and furfuryl alcohol,[33] thenyl mercaptan (TM) and thenyl alcohol (TA),[34] trimethylene oxide and trimethylene sulfide,[14] and thiophene[13] by rotational spectroscopy which have helped to fill this gap. These studies showed that the electronic properties of the chalcogen atom (O or S) play a major role both in the conformational stabilities of the organic compound, and in the preferred binding sites for water and internal dynamics of the complex. The thiophene-water dimer, for instance, is formed by the water molecule binding primarily to the π-electrons of the ring, while in the furan-analogue[35] water interacts preferentially with the oxygen atom of the ring. Furthermore, tunneling splittings were observed in the rotational spectrum of the ground state structures of both complexes due to internal motions of water within the clusters. In thiophene-water, where the sulfur HB is weaker, a highly averaged structure was observed with water situated over the ring nearly in the thiophene σ_v plane rather than off-center closer to one π-bond of the ring as in the equilibrium structure.[13] This was

likely due to smaller energy barriers for the internal motions of water when bound to the π-system, although a comprehensive analysis on furan-water has not been reported to date for comparison.[36] For the TA and TM monohydrates, fundamental differences were observed in their binding topologies as water primarily acts as a HB acceptor in TA via a O–H···O_w HB and as a HB acceptor in TM through a O_w–H···S HB (where O_w refers to the oxygen from water). Both monohydrates are further stabilized from secondary O_w–H···π interactions between the water and the ring π-electrons.

While previous reports on O and S-containing dimers have focused on cyclic monomers rather than more flexible molecules,[13,14,33,34,37–42] it is valuable to explore the conformational landscape of larger hydrated compounds with more diverse conformer distributions. Such studies would provide key information on how binding with water impacts the conformer distribution of the monomer systems. This has been demonstrated previously in the case of allylmethylamine-water,[8] for example, where the interaction with water was sufficient to re-order the relative stabilities of conformers relative to the ordering of the isolated monomers. To build on this, diallyl ether (DAE)[43] and diallyl sulfide (DAS)[43] (chapter 4), are chosen as model systems in the present work as we recently reported surprising differences in the competitive nature of their conformational landscapes using rotational spectroscopy. Although both species have similar arrangements of the allyl sidechains in their ground state structures, the rotational spectrum of DAE exhibited transitions from nine low-energy conformers while for DAS, features due to only the lowest energy conformer were observed. With addition of a single water molecule, we are interested in investigating how the conformational equilibrium of ethers and sulfides are modified in the presence of intermolecular interactions and how the nature of the chalcogen binding partner influences the strength and topology of the interactions.

In this chapter, we explore the conformational landscapes of the DAE and DAS monohydrates, DAE-w and DAS-w, using Fourier transform microwave (FTMW) spectroscopy and quantum chemistry calculations. Rotational transitions arising from the global minimum of each complex were observed and successfully assigned. Tunneling splittings associated with internal motions of water were observed for the DAS-w transitions which provides experimental evidence of a weaker HB interaction through its influence on the barrier to the water internal motions. Quantum theory of atoms in molecules (QTAIM), noncovalent interaction (NCI) analyses and symmetry-adapted perturbation theory (SAPT) calculations provide deeper understanding of the unique interactions responsible for the stability of the monohydrates of DAE and DAS.

7.3 Experimental methods

The rotational spectra of DAE-w and DAS-w were collected using a broadband chirped pulse (8–18 GHz) and a cavity based Balle-Flygare (6–19 GHz) Fourier transform microwave (FTMW) spectrometer. The technical details and operating principles of each instrument have been described in detail elsewhere.[44,45] To produce the monohydrated complexes, a gas mixture containing ~1% of DAE or DAS vapour from a room temperature liquid sample was seeded in Ne and bubbled through a reservoir containing water. The resultant mixture was inserted into the high vacuum chamber of the instruments via a pulsed solenoid valve (1 mm diameter orifice) creating a supersonic jet.

Initially, survey spectra from 8–18 GHz were recorded in segments of 2 GHz each using the chirped pulse FTMW instrument. For each measurement, a total of one million free induction decays (FIDs) were collected and averaged. In the broadband spectra, the most intense transitions of the monohydrates were readily identified leading to preliminary assignments. Next, the

assignments were confirmed by additional measurements using the cavity-based spectrometer which features higher resolution and sensitivity allowing less intense lines to be recorded and small splittings to be resolved. Spectral lines recorded using the cavity-based instrument appear as Doppler doublets due to the instrument setup in which the molecular beam and resonator axis are collinear. Observed line widths for transitions measured with the BF-FTMW instrument are usually ~7 kHz (FWHM) and the uncertainty in assigning the line positions is about ± 2 kHz.

7.4 Computational methods

In previous study of the DAE and DAS monomers, transitions from nine stable conformers of DAE were observed in the rotational spectrum while only spectral signatures for the global minimum of DAS were detected.[43] Since the inclusion of a water molecule to form the monohydrated complexes may disrupt intramolecular interactions occurring in the monomers and alter their relative energy orderings, a comprehensive conformational search for DAE-w and DAS-w was needed for all possible orientations of the monomer geometries and interaction sites for the water molecule. Initial conformational searches for the energy minima of DAE-w and DAS-w were carried out at the GFN2-xTB[46] level of theory using the iMTD-GC algorithm of the conformer-rotamer ensemble sampling tool (CREST) available in the extended tight binding (xTB)[47,48] program package. During the searches, the possible geometries of the DAE and DAS monomers and binding sites for the water molecule were automatically considered by CREST. The automated search yielded 137 and 25 possible geometries for DAE-w and DAS-w, respectively. These geometries were then fully optimized using density functional theory (DFT) B3LYP[49]-D3(BJ)[50,51] with Dunning's aug-cc-pVTZ[52] basis set. These calculations identified 78 and 15 distinct minima for DAE-w and DAS-w, respectively. It is noteworthy that certain initial

geometries from CREST exhibited unusual orientations (e.g. water subunit extremely distant from the monomers) and did not converge. Additionally, numerous geometries converged to the same minima after being optimized at the higher level of theory, which further reduced the number of conformers. To verify the nature of the stationary points and to calculate electronic energies with zero-point corrections (ZPE), as well as quartic centrifugal distortion constants, vibrational frequency calculations were carried out within the harmonic approximation at the same levels of theory. All optimization and harmonic frequency calculations were performed using the Gaussian 16[53] program with the inclusion of Boys and Bernardi's counterpoise method[54] in all calculations to address the basis set superposition (BSSE) error.

As conformers with relative energies larger than 6 kJ mol^{-1} are not expected to be sufficiently populated in the supersonic jet based on the performed calculations, we focused on the energy minima located within 6 kJ mol^{-1} of the global minimum for further consideration. In total, 22 and three stable conformers were found within this energy window for DAE-w and DAS-w, respectively, at the B3LYP-D3(BJ)/aug-cc-pVTZ level using this approach. Given that many conformers of DAE-w were close in energy, we also performed optimization calculations for the conformers of DAE-w and DAS-w from Table 7.1 using the double-hybrid B2PLYP-D3(BJ) method with the aug-cc-pVTZ basis set to confirm the conformer geometries and their relative electronic energies. The results for this second method are compiled as supplementary information.

To confirm the dramatic differences observed in the conformational landscapes of DAE-w and DAS-w, we performed additional optimization and frequency calculations at the B3LYP-D3(BJ)/aug-cc-pVTZ level in which the oxygen atom in the 22 low energy structures of DAE-w was replaced by sulfur. This identified 15 higher conformers of DAS-w with relative energies ranging from 6.4 to as high as 21.9 kJ mol^{-1} and one additional conformer that is 5.8 kJ

mol^{-1} higher than the global minimum. A complete list of the relative energies and rotational parameters of all conformers is given in the supplementary material while the relative energies and spectroscopic parameters for the most significant conformers of each complex, within 6 kJ mol^{-1} of the global minimum, are compiled in Table 7.1. Their geometries are depicted in Figure 7.1. The Cartesian coordinates corresponding to each of these minima are given in Tables S1-S26 of the Supplementary Material file.

To better understand the observed spectral patterns for DAE-w and DAS-w, additional optimization and vibrational frequency calculations were carried out at the B3LYP-D3(BJ)/aug-cc-pVTZ level to find possible transition state structures consistent with the internal motion of water within the complex to interconvert the two hydrogen atoms. Furthermore, post-optimization calculations were conducted to elucidate the intermolecular forces responsible for the most stable conformers of the monohydrates using non-covalent interaction (NCI)[55], quantum theory of atoms in molecules (QTAIM),[56] and symmetry-adapted perturbation theory (SAPT)[57] methods. These analyses were conducted using the NCIPLOT,[58] AIMALL[59] and Psi4[60] programs, respectively and were performed on the equilibrium structures obtained at the B3LYP-D3(BJ)/aug-cc-pVTZ level. For the energy decomposition SAPT analysis, we used the higher order SAPT2+(3)δMP2 method, also with the aug-cc-pVTZ basis set, which has been shown to provide more accurate interaction energies.[60]

Table 7.1 Calculated energies and spectroscopic parameters for the conformers of DAE-w and DAS-w within 6 kJ mol^{-1} at the B3LYP-D3(BJ)/aug-cc-pVTZ level of theory.

DAE-w	ΔE_0[a]	A/B/C[b]	$\lvert\mu_a\rvert$/ $\lvert\mu_b\rvert$/ $\lvert\mu_c\rvert$[c]
I	0.0	2071/1248/881	2.1/0.1/0.9
II	0.8	2501/1122/888	0.2/2.5/0.5
III	1.0	2279/1082/889	0.7/2.1/0.3

IV	1.4	2248/1070/825	0.1/1.8/1.0
V	2.3	2432/1060/812	1.3/2.5/0.6
VI	2.3	2585/1021/850	1.0/2.2/0.5
VII	2.6	1928/1263/885	1.7/1.1/0.3
VIII	2.6	2423/1010/762	0.9/2.6/0.1
IX	2.6	2015/1087/744	1.7/2.0/0.7
X	2.7	2995/920/750	1.0/2.1/0.1
XI	2.9	2664/924/737	0.0/2.4/0.6
XII	3.1	2121/1203/891	1.7/1.5/1.3
XIII	3.3	2755/1035/874	1.0/2.0/0.4
XIV	3.4	2080/1274/915	1.2/2.1/1.0
XV	3.5	2389/1148/997	0.9/2.7/0.3
XVI	3.6	3148/944/775	0.9/1.9/0.0
XVII	3.9	2804/1036/847	1.0/3.0/0.0
XVIII	4.4	1823/1263/838	1.6/1.9/0.0
XIX	4.8	2305/1147/919	0.5/2.4/0.9
XX	4.8	2148/1241/925	1.5/1.8/0.6
XXI	4.8	2196/1148/816	0.7/2.1/0.2
XXII	5.3	2341/1177/981	0.4/3.2/0.7
DAS-w	ΔE_0[a]	A/B/C[b]	|µa|/ |µb|/ |µc|[c]
I	0.0	1764/1042/814	1.4/0.4/0.5
II	5.8	1758/925/805	0.0/1.3/0.4
III	5.9	1824/911/738	0.6/0.4/0.4

[a]Zero-point energy (ZPE) corrected relative energies in kJ mol^{-1}, [b]rotational constants in MHz, [c]magnitude of the electric dipole moment components in Debye.

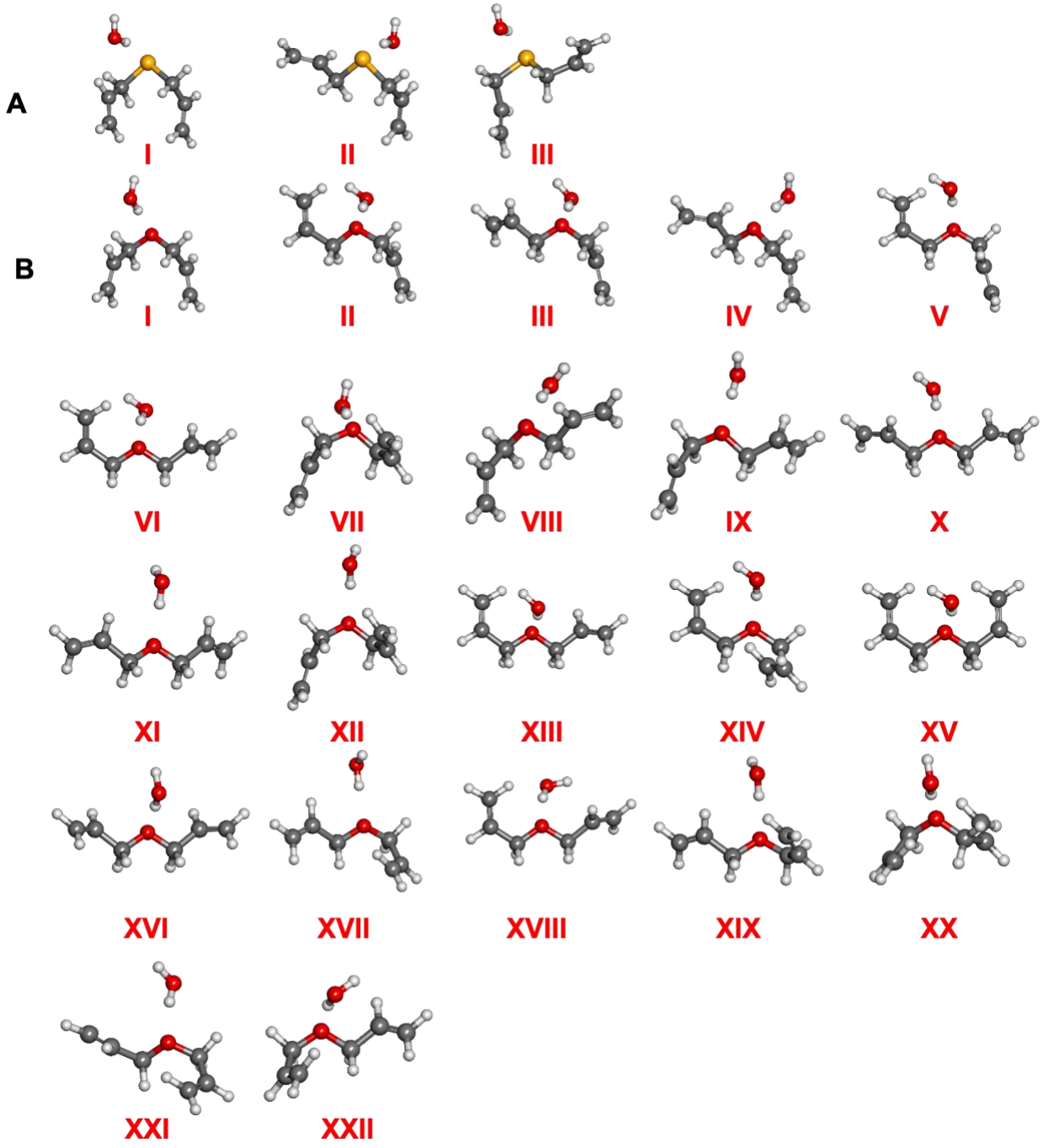

Figure 7.1 Minima energy conformers within 6 kJ mol^{-1} of A) DAS-w B) DAE-w complex at the B3LYP-D3(BJ)/aug-cc-pVTZ level of theory.

7.5 Results

The calculated spectroscopic and energy parameters for stable complexes within 6 kJ mol^{-1} (B3LYP-D3(BJ)/aug-cc-pVTZ) of the global minimum of DAE-w and DAS-w are provided in Table 7.1 and the geometries are displayed in Figure 7.1. Roman numerals were used to label the stability ordering of conformers from B3LYP-D3(BJ), with conformer I being the most stable geometry. Comparison with the results from the B2PLYP-D3(BJ) method, given as supplementary material using the same conformer labels, reveal that the same conformational equilibrium is captured by both methods although in some cases, the relative energy orderings change for DAE-w conformers. This is not surprising given the highly competitive conformational landscape of this complex.

Experimentally, after subtracting transitions from the parent and singly-substituted isotopologues of the DAE and DAS monomers as well as known lines due to the water dimer, an additional set of transitions were observed in the broadband spectrum of each gas mixture. The observed patterns were consistent with those predicted for the most stable conformers of DAE-w-I and DAS-w-I in Table 7.1. With the high-resolution of the BF-FTMW instrument, a tunnelling splitting was detected in the spectrum of DAS-w-I, an example of which is shown in Figure 7.2. The splitting components present a typical 3:1 ratio of intensities related to the ortho-para nuclear spin statistics for exchange of two hydrogen atoms. No resolvable splittings were observed in the transitions of DAE-w-I. In total, 48 *a*-type and 21 *c*-type rotational transitions were observed for DAE-w-I. The observed types of transitions align well with the calculated dipole moment components (Table 7.1). No *b*-type transitions were detected for DAE-w as the predicted value of μ_b is small. For DAS-w, 49 *a*-type and two *b*-type transitions were observed. Although the absolute values predicted for μ_b= 0.4 D and μ_c= 0.5 D are similar, no *c*-type transitions could be observed

for DAS-w-I. The absence of *c*-type transitions in the spectrum of DAS-w-I may provide clues to identify the tunneling motion associated with the water dynamics that averages out along the c-axis.

All rotational transitions observed for conformer I of DAE-w and DAS-w were fit using Pickett's SPFIT program[61] (Watson's S-reduced Hamiltonian, I^r representation) to derive experimental rotational and quartic centrifugal distortion constants. The resulting parameters are given in Table 7.2, while the transition frequencies are listed in Tables S28-S30. The two tunneling states observed for DAS-w-I were analyzed independently and are labeled in Table 7.2 as I+ and I-. It is worth noting that, although DAE-w is predicted to have a more competitive equilibrium with many other low energy conformers (Table 7.1), only lines due to the global minimum conformer I could be assigned. After removing lines from all detected species, many low intensity features remain in the DAE-w spectra which may arise from other conformers of DAE-w or from higher-order hydrates, however, no convincing assignment was achieved.

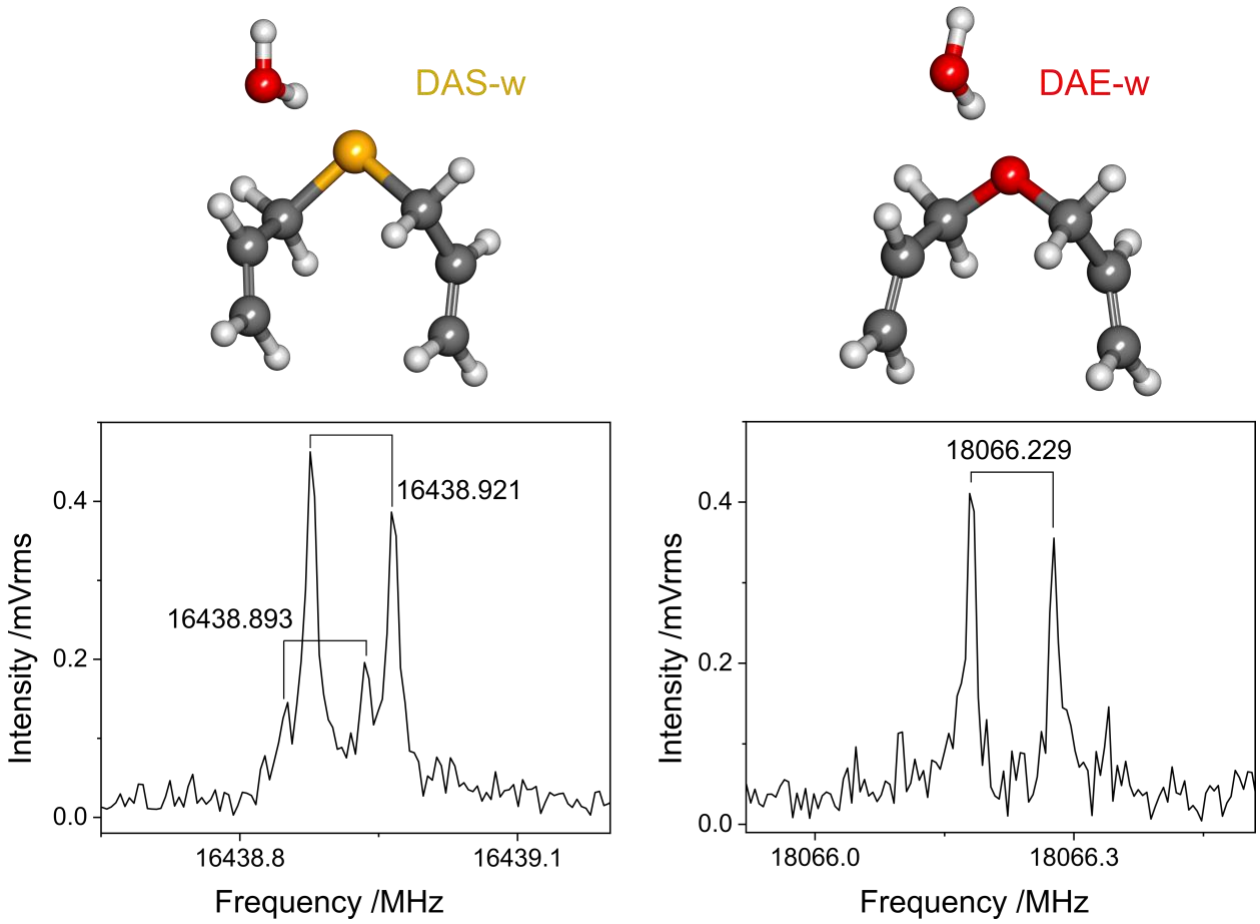

Figure 7.2 Equilibrium structures (B3LYP-D3(BJ)/aug-cc-pVTZ) and BF-FTMW spectra of the $10_{1,10}$–$9_{1,9}$ rotational transitions of conformer I of DAS-w (left) and DAE-w (right).

Table 7.2 Ground state spectroscopic parameters for the observed conformers of DAE-w and DAS-w including the two tunnelling states for DAS-w.

Parameter	DAE-w	DAS-w	
	I	I+	I-
A/MHz[a]	2109.51322(23)	1774.0279(24)	1774.0327(28)
B/MHz	1223.563388(88)	1021.31707(20)	1021.31552(24)
C/MHz	870.307757(72)	799.01585(13)	799.01393(13)
D_J/kHz[b]	0.64402(59)	1.7555(11)	1.7525(20)
D_{JK}/kHz	2.1011(40)	-11.264(15)	-11.265(18)
D_K/kHz	5.814(12)	26.25(17)	26.42(24)
d_1/kHz	-0.12870(37)	0.06985(57)	0.0702(11)
d_2/kHz	-0.07005(20)	-0.02091(47)	-0.02136(46)
$\mu_a/\mu_b/\mu_c$	y/n/y	y/y/n	y/y/n
N[d]	69	51	41
σ/kHz[e]	1.5	2.2	1.9

[a]Rotational constants; [b]quartic centrifugal distortion constants; [c]electric dipole moment components ("y" if observed and "n" if not observed); [d]total number of lines (N) in the fit; [e]root-mean-square deviation of the fit. A complete list of calculated parameters at the B3LYP-D3(BJ)/aug-cc pVTZ level of theory is provided in Table S27 for comparison.

7.6 Discussion

In the presence of a single water molecule, the overall conformational landscapes of the DAE and DAS monomers remain surprisingly different as DAE-w is predicted to form many low-lying energy conformers whereas DAS-w adopts only one particularly stable geometry (Table 7.1). For the lowest energy of forms of each monohydrate (Conformer I), the ether and sulfide geometries closely match those previously reported for the isolated DAE[43] and DAS[43] monomers (Appendix 8 of supplementary material) with dihedral angles describing the heavy atom backbone maintained to within two degrees. Although the geometries themselves are not significantly altered, the relative stabilities of conformers beyond the global minimum change following complexation with water, particularly for DAE (Table 1). This is exemplified, for example, by the destabilization of conformer II of DAE,[43] which becomes only the fifteenth most stable dimer,

conformer XV of DAE-w (Table 7.1), indicating that interactions with water disrupt the conformational equilibrium of DAE. Specifically, conformer II of DAE adopts a "W-shaped" structure, stabilized by orbital LP(O) → $\sigma^*_{C\text{-}C}$ interactions involving the lone-pairs on oxygen and the allyl side chains.[43] Upon binding to water in DAE-w, these intramolecular interactions in the monomer are diminished as now the central oxygen atom of DAE also binds to the water subunit leading to the higher energy of DAE-w conformer XV (Figure 7.1). A similar effect is also observed for DAE conformer IV, that exhibits a V-shaped structure (only one allyl side chain pointing up) and is destabilized upon binding with water to form the DAE-w conformer XIII (Figure 7.1). This does not extend to every V- or W-shaped structure of the monomers, however, as the second most stable dimer, DAE-w-II, has a V-shaped arrangement within the organic framework and corresponds to conformer III of the DAE monomer. This indicates that there are more effects at play and that the stabilization of the dimers also depends on the orientation of the other allyl group on the opposite side and how it interacts with water. From these examples of the effect of water on the relative stabilities of the monomer structures, it is evident that the orbital interactions involving the lone-pairs on the chalcogen are central to stabilizing the monomer geometries that give rise to its highly competitive conformational equilibria.[43] These intramolecular contacts appear even more important than in the case of the allylmethylamine monohydrate (AMA-w) dimer,[8] in which binding to water only disrupted the relative energy ordering of the higher energy forms of AMA while in DAE-w and DAS-w, the conformational stabilities are altered for most conformers beyond the global minimum geometries.

As shown in Figure 7.1, in all other geometries of DAE-w and DAS-w (except for conformer XIV of DAE-w), water binds preferentially to the central chalcogen atom through a OH···X (X= O, S) HB. Additionally, secondary HBs between the oxygen of water and the allyl

substituents become possible due to the favourable orientation of these groups within most isomers. To gain a deeper understanding of the topology of the interactions present in the observed conformers of DAE-w and DAS-w, we carried out NCI analyses and the outcomes are illustrated in Figure 7.3. The NCI isosurfaces of both clusters are similarly placed and confirm the presence of both primary and secondary HBs with the strongest contact being the intermolecular OH···X (X= O, S) interaction (blue isosurface). For a quantitative comparison of the HB strengths, we analyzed in detail NCI plots of reduced density gradient (RDG) values against the sign of the second eigenvalue of the electron density Hessian matrix sign(λ_2)ρ, which can also distinguish between attractive ($\lambda_2 < 0$) and repulsive ($\lambda_2 > 0$) interactions.[55,58] In these plots, the primary HB is identified by the most negative peak, and it is evident from the figure that the sulfur contact (sign(λ_2)ρ ~ -0.02) is weaker than the oxygen one (sign(λ_2)ρ ~ -0.03). The secondary CH···O HB, represented by the negative peak around sign(λ_2)ρ ~ -0.01 for both clusters, is slightly stronger in DAS-w. Additional support of the NCI findings is obtained from QTAIM molecular graphs (Figure S1 and Table S31) which show the presence of a bond critical point (BCP) between the atoms involved in the HB interactions. The QTAIM results confirm the nature of the primary and secondary HBs with the primary contact being considerably smaller in DAS-w (-16.7 kJ mol^{-1}) than in DAE-w (-36.7 kJ mol^{-1}) but the secondary interaction showing the reverse trend (-5.0 kJ mol^{-1} versus -3.5 kJ mol^{-1} for DAS-w and DAE-w, respectively). The magnitude of the interactions is consistent with the bond lengths between the participating atoms from the equilibrium structures at the B3LYP-D3(BJ)/aug-cc-pVTZ level (OH···O= 1.86 Å and CH···O= 2.79 Å in DAE-w, and OH···S= 2.39 Å and CH···O= 2.59 Å in DAS-w). Apart from the HBs with water, the NCI graphs also exhibit weak intramolecular contacts (either attractive or repulsive) between the allyl moieties in DAE and DAS shown as green isosurfaces in Figure 3. These interactions were also observed

in the NCI graphs of the corresponding monomers in the absence of water indicating that binding with water does not significantly alter the intramolecular contacts in these geometries.

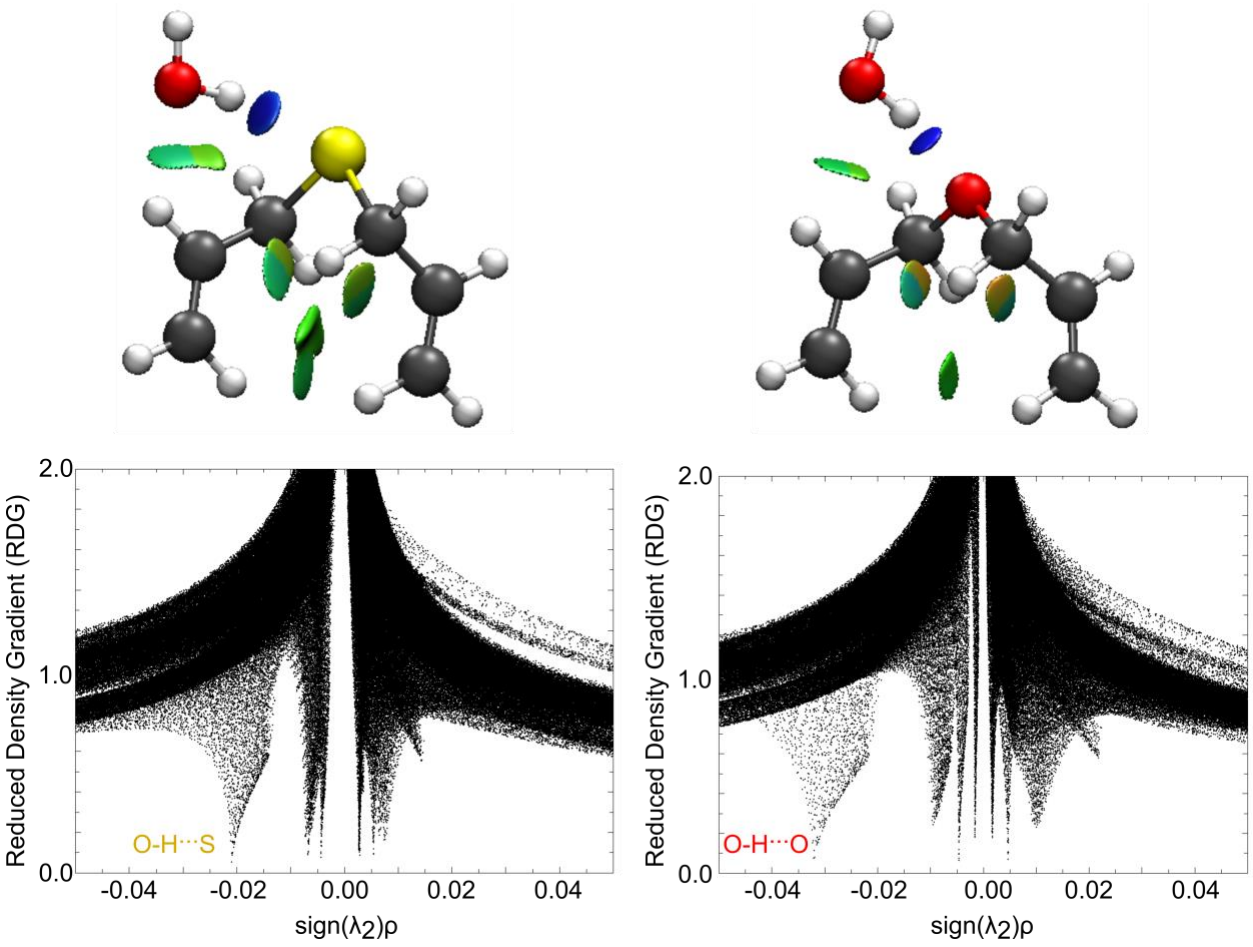

Figure 7.3 NCI isosurface (top) and graphs of reduced density gradient (RDG) versus sign(λ_2)ρ for conformer I of DAS-w (left) and DAE-w (right).

The nature of the intermolecular HBs was further investigated using symmetry-adapted perturbation theory (SAPT) calculations at the SAPT2+(3)δMP2/aug-cc-pVTZ level of theory, shown in Figure 7.4. The total SAPT energy for DAE-w and DAS-w are -27.9 kJ mol^{-1} and -21.2 kJ mol^{-1}, respectively, in agreement with the DFT interaction energies (-28.7 kJ mol^{-1} for DAE-w and -23.5 kJ mol^{-1} for DAS-w), which are the energy difference between the product complex and

its monomer components taking accounting also for the BSSE error and ZPE corrections. Decomposing the overall SAPT energy into the three stabilizing components (electrostatics, induction, and dispersion) and the one destabilizing exchange-repulsion component reveals that the electrostatic portion is the most significant contributor to the stabilization of both DAE-w and DAS-w, followed by dispersion and induction effects. Upon chalcogen substitution from DAE-w to DAS-w, there is an increase of approximately 7% in the contribution from dispersion, which aligns well with the knowledge that sulfur HBs are more dispersive in nature than oxygen HBs due to the weaker HB acceptor character of sulfur.

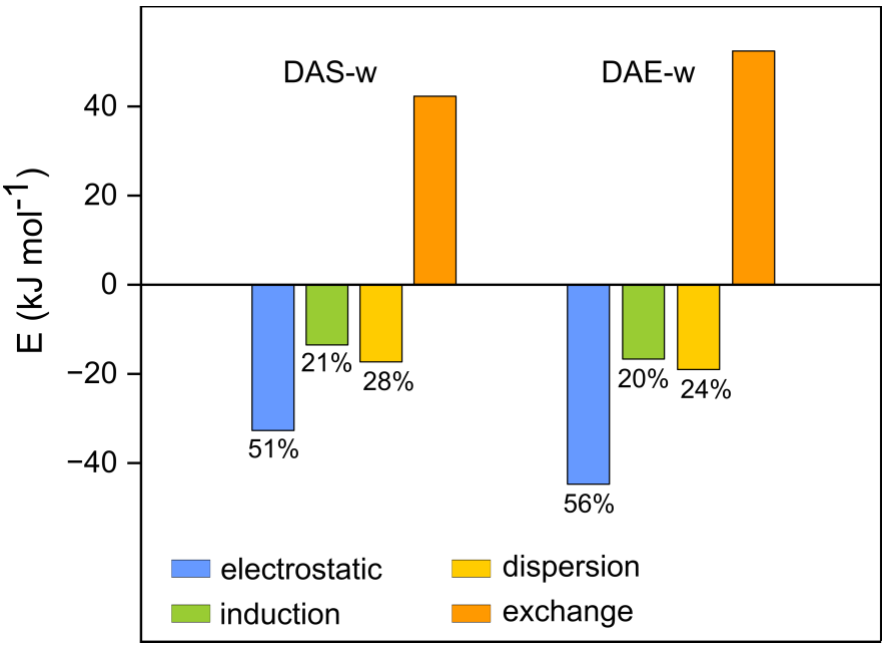

Figure 7.4 Histogram of the stabilizing (electrostatic, induction, dispersion) and destabilizing exchange-repulsion components of the total SAPT interaction energy of DAS-w (-21.2 kJ mol^{-1}) and DAE-w (-27.9 kJ mol^{-1}). The percentages represent the contribution of that specific term to the total stabilizing energy (electrostatic + induction + dispersion). The values of each term are provided in Table S32.

Finally, to further explore how the HB strengths contribute to the distinct energy barriers associated with the internal motions of water, we identified and optimized transition state (TS) structures for potential tunneling pathways for each complex. During the TS search, we focused on pathways that would lead to exchange of the protons of water as the observed tunneling for DAS-w shows a typical 3:1 ratio (Figure 7.2) of intensities as one would expect based on ortho-para nuclear spin statistics for exchange of two hydrogen atoms. The possible TS structures identified for DAS-w and DAE-w are given in Figure 7.5 and their Cartesian coordinates are provided in Tables S33 and S34, respectively. For each, we found a vibrational imaginary frequency linked to a motion which interconverts the hydrogen atom of water that binds to the central chalcogen atom. Notably, the position of water in the TS structures for DAE-w and DAS-w are significantly different. In the DAE-w TS, the water molecule is positioned near the lone pairs of the ether oxygen with both hydrogen atoms approximately 2.4 Å from the bridge atom and its C_{2V} axis slightly tilted toward one of the allyl groups. This is likely a consequence of the disruption to the primary HB making the water molecule adopt a slightly more favourable location. In contrast, in the DAS-w TS, the water subunit remains on one side of the molecule closer to one allyl fragment but now positions one hydrogen atom facing the sulfur, while the other hydrogen is oriented towards the allyl side chain. The difference in the TS geometries likely reflects the dominance of the primary HB interaction in DAE-w and its greater electrostatic nature in comparison to DAS-w whereas in the latter, the secondary interaction between water and the allyl group is sufficiently strong to maintain the interaction between these groups in the TS. The tunneling motion in DAS-w occurs through a TS barrier of 6.0 kJ mol^{-1} accounting for zero-point corrections, while the analogous barrier in DAE-w is 9.4 kJ mol^{-1} which are consistent with the strength of the S and O HBs that are disrupted during the water internal motion. This barrier

difference of 3.4 kJ mol^{-1} is sufficient to prevent the observation of tunneling splittings for DAE-w in our frequency range given that the tunneling components were barely-resolved for DAS-w (Figure 7.2).

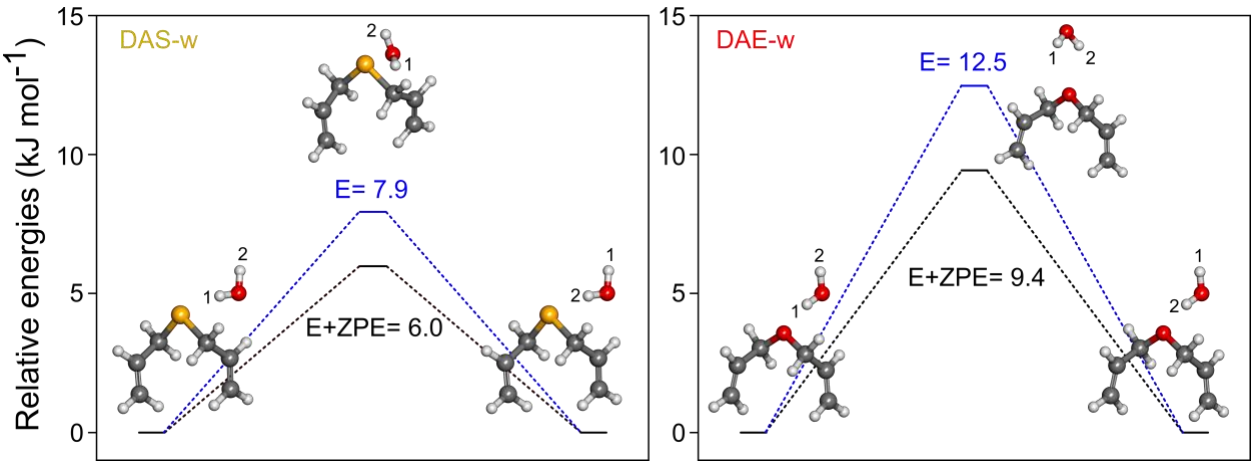

Figure 7.5 Possible transition states for the water internal motion within the DAE-w (left) and DAS-w (right) that have a vibrational imaginary frequency consistent with a motion of water that leads to the exchange of the water protons.

7.7 Conclusions

The powerful combination of rotational spectroscopy and quantum chemistry calculations has provided insights into the impact of a single water molecule on the conformational landscape of DAE and DAS at the molecular level. Compared to the ring monohydrate analogues like thiophene-water[13] and furan-water,[35,36] as well as thenyl alcohol-water[34] and thenyl mercaptan-water,[34] where the binding sites are different for the O and S congeners, the investigation of the DAE-w and DAS-w conformational landscapes shows that the overall topology of the intermolecular interaction with water is more similar for the two species. On closer inspection, however, the binding to water disrupts the stability ordering of the flexible monomer backbones in both DAE and DAS which speaks to the importance of the intramolecular orbital interactions

involving the LP(O) and LP(S) in stabilizing the associated monomer systems. Differences in the HB acceptor character of O and S also lead to unique features in the spectra of these complexes with the weaker binding between water and DAS giving rise to a more dynamic complex. In summary, our study demonstrates how the nature of the chalcogen atom in large and flexible monomers affects their interactions with binding partner molecules and impacts their conformational equilibria. Characterizing these features at the molecular level fosters novel insights into solvation processes and internal dynamics of organic ethers and sulfides.

7.8 References

1 E. Brini, C. J. Fennell, M. Fernandez-Serra, B. Hribar-Lee, M. Lukšič and K. A. Dill, How Water's Properties Are Encoded in Its Molecular Structure and Energies, *Chem. Rev.*, 2017, **117**, 12385–12414.

2 G. Hummer and A. Tokmakoff, Preface: Special topic on biological water, *J. Chem. Phys.*, 2014, **141**, 1–3.

3 C. J. Li and L. Chen, Organic chemistry in water, *Chem. Soc. Rev.*, 2006, **35**, 68–82.

4 N. Nandi, K. Bhattacharyya and B. Bagchi, Dielectric relaxation and solvation dynamics of water in complex chemical and biological systems, *Chem. Rev.*, 2000, **100**, 2013–2045.

5 B. Bagchi, *Water in biological and chemical processes: from structure and dynamics to function*, Cambridge University Press, 2013.

6 W. Sun and M. Schnell, Microhydrated 3-Methyl-3-oxetanemethanol: Evolution of the Hydrogen-Bonding Network from Chains to Cubes, *Angew. Chemie - Int. Ed.*, 2022, **61**, e202210819.

7 W. Li, M. M. Quesada-Moreno, P. Pinacho and M. Schnell, Unlocking the Water Trimer

Loop: Isotopic Study of Benzophenone-(H_2O) 1–3 Clusters with Rotational Spectroscopy , *Angew. Chemie*, 2021, **133**, 5383–5390.

8 W. G. D. P. Silva, T. Poonia and J. van Wijngaarden, Exploring the non-covalent interactions behind the formation of amine-water complexes: The case of N-allylmethylamine monohydrate, *Phys. Chem. Chem. Phys.*, 2021, **23**, 7368–7375.

9 P. Pinacho, J. C. López, Z. Kisiel and S. Blanco, Microsolvation of ethyl carbamate conformers: Effect of carrier gas on the formation of complexes, *Phys. Chem. Chem. Phys.*, 2020, **22**, 18351–18360.

10 G. Salvitti, F. Baroncelli, C. Nicotri, L. Evangelisti, S. Melandri and A. Maris, How Water Interacts with the NOH Group: The Rotational Spectrum of the 1:1 N,N-diethylhydroxylamine·Water Complex, *Molecules*, 2022, **27**, 1–14.

11 B. Wu, N. A. Seifert, S. Oswald, W. Jäger and Y. Xu, Rotational Spectroscopy of the 2,2,3,3,3-Pentafluoropropanol···Water Complex: Conformations and Large Amplitude Motions, *ChemPhysChem*, 2022, **23**, e202200348.

12 B. Wu, A. S. Hazrah, N. A. Seifert, S. Oswald, W. Jäger and Y. Xu, Higher-Energy Hexafluoroisopropanol···Water Isomer and Its Large Amplitude Motions: Rotational Spectra and DFT Calculations, *J. Phys. Chem. A*, 2021, **125**, 10401–10409.

13 W. G. D. P. Silva and J. Van Wijngaarden, Characterization of Large-Amplitude Motions and Hydrogen Bonding Interactions in the Thiophene-Water Complex by Rotational Spectroscopy, *J. Phys. Chem. A*, 2021, **125**, 3425–3431.

14 W. G. D. P. Silva and J. van Wijngaarden, Hydrogen bonding networks and cooperativity effects in the aqueous solvation of trimethylene oxide and sulfide rings by microwave spectroscopy and computational chemistry, *J. Chem. Phys.*, 2021, **155**, 034305.

15 L. Ferres, L. Evangelisti, A. Maris, S. Melandri, W. Caminati, W. Stahl and H. V. L. Nguyen, Skeletal Torsion Tunneling and Methyl Internal Rotation: The Coupled Large Amplitude Motions in Phenyl Acetate, *Molecules*, 2022, **27**, 2730.

16 H. V. L. Nguyen, W. Caminati and J. U. Grabow, The LAM of the Rings: Large Amplitude Motions in Aromatic Molecules Studied by Microwave Spectroscopy, *Molecules*, 2022, **27**, 3948.

17 W. Cheng, Y. Zheng, G. Feng, J. U. Grabow and Q. Gou, Conformation and bonding of 2-methoxypyridine and its monohydrate from rotational spectra, *Spectrochim. Acta - Part A Mol. Biomol. Spectrosc.*, 2020, **239**, 118434.

18 E. Arunan, G. R. Desiraju, R. A. Klein, J. Sadlej, S. Scheiner, I. Alkorta, D. C. Clary, R. H. Crabtree, J. J. Dannenber, P. Hobza, H. G. Kjaergaard, A. C. Legon, B. Mennucci and D. J. Nesbitt, Definition of the hydrogen bond (IUPAC Recommendations 2011), *Pure Appl. Chem.*, 2011, **83**, 1637–1641.

19 A. Chand, D. K. Sahoo, A. Rana, S. Jena and H. S. Biswal, The Prodigious Hydrogen Bonds with Sulfur and Selenium in Molecular Assemblies, Structural Biology, and Functional Materials, *Acc. Chem. Res.*, 2020, **53**, 1580–1592.

20 N. T. Bui, H. Kang, S. J. Teat, G. M. Su, C. W. Pao, Y. S. Liu, E. W. Zaia, J. Guo, J. L. Chen, K. R. Meihaus, C. Dun, T. M. Mattox, J. R. Long, P. Fiske, R. Kostecki and J. J. Urban, A nature-inspired hydrogen-bonded supramolecular complex for selective copper ion removal from water, *Nat. Commun.*, 2020, **11**, 1–12.

21 S. Dai, L. M. Funk, F. R. von Pappenheim, V. Sautner, M. Paulikat, B. Schröder, J. Uranga, R. A. Mata and K. Tittmann, Low-barrier hydrogen bonds in enzyme cooperativity, *Nature*, 2019, **573**, 609–613.

22 R. Zhang, A. Khalizov, L. Wang, M. Hu and W. Xu, Nucleation and growth of nanoparticles in the atmosphere, *Chem. Rev.*, 2012, **112**, 1957–2011.

23 J. U. Bowie, Membrane protein folding: How important are hydrogen bonds?, *Curr. Opin. Struct. Biol.*, 2011, **21**, 42–49.

24 T. Lu, J. Zhang, Y. Xu, Z. Wang, G. Feng and Z. Zeng, Hydrogen bond interactions between thioethers and amides: A joint rotational spectroscopic and theoretical study of the formamide···dimethyl sulfide adduct, *Spectrochim. Acta - Part A Mol. Biomol. Spectrosc.*, 2023, **288**, 122199.

25 Y. Zheng, J. Chen, C. Duan, X. Zhang, X. Xu and Q. Gou, Accurate Geometry and Non-Covalent Interactions in 1-Phenylethanol and its Monohydrate: A Rotational Study, *ChemPhysChem*, 2023, **24**, 1–7.

26 W. Li, M. Li, Y. Jin, Q. Gou, J. U. Grabow and G. Feng, Molecular structure and non-covalent interaction of 2-thiophenecarboxaldehyde and its monohydrated complex, *J. Chem. Phys.*, 2019, **151**, 164307.

27 E. N. Baker and R. E. Hubbard, Hydrogen bonding in globular proteins, *Prog. Biophys. Mol. Biol.*, 1984, **44**, 97–179.

28 T. Steiner and G. Koellner, Hydrogen bonds with π-acceptors in proteins: Frequencies and role in stabilizing local 3D structures, *J. Mol. Biol.*, 2001, **305**, 535–557.

29 L. Jiang and L. Lai, CH···O hydrogen bonds at protein-protein interfaces, *J. Biol. Chem.*, 2002, **277**, 37732–37740.

30 P. Zhou, F. Tian, F. Lv and Z. Shang, Geometric characteristics of hydrogen bonds involving sulfur atoms in proteins, *Proteins Struct. Funct. Bioinforma.*, 2009, **76**, 151–163.

31 H. S. Biswal, *Hydrogen Bonding Involving Sulfur: New Insights from Ab Initio Calculations*

and Gas Phase Laser Spectroscopy, in Noncovalent Forces, ed. S. Scheiner, Springer Int. Pub., Switzerland, 2015.

32 H. S. Biswal, S. Bhattacharyya, A. Bhattacherjee and S. Wategaonkar, Nature and strength of sulfur-centred hydrogen bonds: Laser spectroscopic investigations in the gas phase and quantum-chemical calculations, *Int. Rev. Phys. Chem.*, 2015, **34**, 99–160.

33 M. Juanes, A. Lesarri, R. Pinacho, E. Charro, J. E. Rubio, L. Enríquez and M. Jaraíz, Sulfur Hydrogen Bonding in Isolated Monohydrates: Furfuryl Mercaptan versus Furfuryl Alcohol, *Chem. - A Eur. J.*, 2018, **24**, 6564–6571.

34 M. Juanes, R. T. Saragi, R. Pinacho, J. E. Rubio and A. Lesarri, Sulfur hydrogen bonding and internal dynamics in the monohydrates of thenyl mercaptan and thenyl alcohol, *Phys. Chem. Chem. Phys.*, 2020, **22**, 12412–12421.

35 S. P. Lockwood, T. G. Fuller and J. J. Newby, Structure and Spectroscopy of Furan:H_2O Complexes, *J. Phys. Chem. A*, 2018, **122**, 7160–7170.

36 F. L. Bettens, R. P. A. Bettens and A. Bauder, The Microwave Spectrum and r_0 Structure of the Furan···H_2O Complex, A Case of Large Amplitude Motion, *Int. Symp. Mol. Spectrosc.*

37 J. L. Alonso, S. Antolínez, S. Blanco, A. Lesarri, J. C. López and W. Caminati, Weak C-H···O and C-H···F-C Hydrogen Bonds in the Oxirane-Trifluoromethane Dimer, *Acta Crystallogr. Sect. C Struct. Chem.*, 2018, **74**, 1610–1621.

38 E. J. Cocinero, R. Sánchez, S. Blanco, A. Lesarri, J. C. López and J. L. Alonso, Weak hydrogen bonds C-H···S and C-H···F-C in the thiirane-trifluoromethane dimer, *Chem. Phys. Lett.*, 2005, **402**, 4–10.

39 S. Antolínez, J. C. López and J. L. Alonso, Rotational spectra and structure of the hydrogen-

bonded complex oxetane HCl, *Chem. Phys. Lett.*, 2001, **334**, 250–256.

40 M. E. Sanz, J. C. López and J. L. Alonso, Axial and equatorial hydrogen-bond conformers and ring-puckering motion in the trimethylene sulfide-hydrogen fluoride complex, *Chem. - A Eur. J.*, 2002, **8**, 4265–4271.

41 M. E. Sanz, V. M. Sanz, J. C. López and J. L. Alonso, Oxetane-hydrogen fluoride complex: A rotational study, *Chem. Phys. Lett.*, 2001, **342**, 31–38.

42 M. E. Sanz, A. Lesarri, J. C. L. Pez and J. L. Alonso, Hydrogen bond in molecules with large-amplitude motions: A rotational study of trimethylene sulfide···HCl, *Angew. Chemie - Int. Ed.*, 2001, **40**, 935–938.

43 T. Poonia, W. G. D. P. Silva and J. van Wijngaarden, Dramatic differences in the conformational equilibria of chalcogen-bridged compounds: The case of diallyl ether versus diallyl sulfide, *Phys. Chem. Chem. Phys.*, 2022, **24**, 240–248.

44 L. Evangelisti, G. Sedo and J. van Wijngaarden, Rotational Spectrum of 1,1,1-Trifluoro-2-butanone Using Chirped-Pulse Fourier Transform Microwave Spectroscopy, *J. Phys. Chem. A*, 2011, **115**, 685–690.

45 G. Sedo and J. van Wijngaarden, Fourier transform microwave spectra of a “new” isomer of OCS-CO_2, *J. Chem. Phys.*, 2009, **131**, 044303.

46 C. Bannwarth, S. Ehlert and S. Grimme, GFN2-xTB - An Accurate and Broadly Parametrized Self-Consistent Tight-Binding Quantum Chemical Method with Multipole Electrostatics and Density-Dependent Dispersion Contributions, *J. Chem. Theory Comput.*, 2019, **15**, 1652–1671.

47 S. Grimme, Exploration of Chemical Compound, Conformer, and Reaction Space with Meta-Dynamics Simulations Based on Tight-Binding Quantum Chemical Calculations, *J.*

Chem. Theory Comput., 2019, **15**, 2847–2862.

48 P. Pracht, F. Bohle and S. Grimme, Automated exploration of the low-energy chemical space with fast quantum chemical methods, *Phys. Chem. Chem. Phys.*, 2020, **22**, 7169–7192.

49 A. D. Becke, A new inhomogeneity parameter in density-functional theory, *J. Chem. Phys.*, 1998, **109**, 2092–2098.

50 S. Grimme, S. Ehrlich and L. Goerigk, Effect of the damping function in dispersion corrected density functional theory, *J. Comput. Chem.*, 2011, **32**, 1456–1465.

51 S. Grimme, J. Antony, S. Ehrlich and H. Krieg, A consistent and accurate ab initio parametrization of density functional dispersion correction (DFT-D) for the 94 elements H-Pu, *J. Chem. Phys.*, 2010, **132**, 1–19.

52 T. H. Dunning, Gaussian basis sets for use in correlated molecular calculations. I. The atoms boron through neon and hydrogen, *J. Chem. Phys.*, 1989, **90**, 1007–1023.

53 M. J. Frisch, G. W. Trucks, H. B. Schlegel, G. E. Scuseria, M. A. Robb, J. R. Cheeseman, G. Scalmani, V. Barone, B. Mennucci, G. A. Petersson, H. Nakatsuji, M. Caricato, X. Li, H. P. Hratchian, A. F. Izmaylov, J. Bloino, G. Zheng, J. L. Sonnenberg, M. Hada, M. E. Fukuda, K. T. R., J. Hasegawa, M. Ishida, T. Nakajima, Y. Honda, O. Kitao, H. Nakai, T. Vreven, J. A. Montgomery, J. E. Peralta, F. Ogliaro, M. Bearpark, J. J. Heyd, E. Brothers, K. N. Kudin, V. N. Staroverov, R. Kobayashi, J. Normand, K. Raghavachari, A. Rendell, J. C. Burant, S. S. Iyengar, J. Tomasi, M. Cossi, N. Rega, J. M. Millam, M. Klene, J. E. Knox, J. B. Cross, V. Bakken, C. Adamo, J. Jaramillo, R. Gomperts, R. E. Stratmann, O. Yazyev, A. J. Austin, R. Cammi, C. Pomelli, J. W. Ochterski, R. L. Martin, K. Morokuma, V. G. Zakrzewski, G. A. Voth, P. Salvador, J. J. Dannenberg, S. Dapprich, A. D. Daniels, Farkas,

J. B. Foresman, J. V Ortiz, J. Cioslowski and D. J. Fox, Gaussian 16 (Revision C.01), Gaussian, Inc., Wallingford CT, 2016.

54 S. F. Boys and F. Bernardi, The calculation of small molecular interactions by the differences of separate total energies. Some procedures with reduced errors, *Mol. Phys.*, 1970, **19**, 553–566.

55 E. R. Johnson, S. Keinan, P. Mori-Sánchez, J. Contreras-García, A. J. Cohen and W. Yang, Revealing noncovalent interactions, *J. Am. Chem. Soc.*, 2010, **132**, 6498–6506.

56 R. F. W. Bader, Atoms in Molecules, *Acc. Chem. Res.*, 1985, **18**, 9–15.

57 B. Jeziorski, R. Moszynski and K. Szalewicz, Perturbation Theory Approach to Intermolecular Potential Energy Surfaces of van der Waals Complexes, *Chem. Rev.*, 1994, **94**, 1887–1930.

58 J. Contreras-García, E. R. Johnson, S. Keinan, R. Chaudret, J. P. Piquemal, D. N. Beratan and W. Yang, NCIPLOT: A program for plotting noncovalent interaction regions, *J. Chem. Theory Comput.*, 2011, **7**, 625–632.

59 T. A. Keith, AIMALL, Version 17.11.14, TK Gristmill Software: Overland Park, KS, USA, 2016.

60 R. M. Parrish, L. A. Burns, D. G. A. Smith, A. C. Simmonett, A. E. DePrince, E. G. Hohenstein, U. Bozkaya, A. Y. Sokolov, R. Di Remigio, R. M. Richard, J. F. Gonthier, A. M. James, H. R. McAlexander, A. Kumar, M. Saitow, X. Wang, B. P. Pritchard, P. Verma, H. F. Schaefer, K. Patkowski, R. A. King, E. F. Valeev, F. A. Evangelista, J. M. Turney, T. D. Crawford and C. D. Sherrill, Psi4 1.1: An Open-Source Electronic Structure Program Emphasizing Automation, Advanced Libraries, and Interoperability, *J. Chem. Theory Comput.*, 2017, **13**, 3185–3197.

61 H. M. Pickett, The fitting and prediction of vibration-rotation spectra with spin interactions, *J. Mol. Spectrosc.*, 1991, **148**, 371–377.

Chapter 8. Summary and future outlook

8.1 Summary

This thesis successfully investigated the impact of various organic substituents on the conformational landscape of chalcogen-bridged (O *vs* S) compounds by using high-level quantum chemical calculations and Fourier transform microwave spectroscopy. The prediction of crucial spectroscopic parameters (such as rotational constants, dipole moments and distortion constants), through theoretical calculations was employed to assign the spectra obtained via FTMW spectrometers. The use of two custom-built FTMW spectrometers highlighted the advantages of combining a broadband chirped-pulse spectrometer for conducting an initial spectrum survey, followed by the utilization of the narrowband Balle-Flygare instrument with enhanced resolution and sensitivity. This combination proved to be vital for effective conformational analysis studies as well as providing valuable insights into the molecular geometries of the studied compounds. The quantum chemical calculations further contributed to understanding the underlying factors governing conformational preferences by identifying the non-covalent interactions responsible for their stability.

At first, by investigating the conformers of diallyl compounds, DAE and DAS, in chapter 4 we learned that that conformational landscape is drastically different when the central bridging atom was changed from the lighter congener (O) to the heavier one (S). This difference was attributed to the presence of hyperconjugative (or charge transfer) interactions involving the lone pair (LP) of the oxygen atom with the adjacent allyl side chains, which was absent in the case of DAS. We also learned that the ground state geometries of DAE and DAS showed some similarities, with both allyl groups facing downward. However, some distinction was unveiled through the

experimentally derived geometry of conformer I for both compounds. Notably, the C-S-C angle was found to be approximately 14^{o} smaller than the C-O-C angle, which is consistent with the hybridization of the central atom, indicating that sulfur possesses a larger p-orbital character compared to oxygen. These surprising differences in DAE and DAS highlight that the LP electrons on the central chalcogen atom have a significant impact on the arrangement of the allyl side chains.

To ascertain whether this phenomenon is universally applicable to organic ethers (that is that they adopt a rich conformational mixture of many more stable conformers than their heavy congeners), in Chapter 5 we studied AEE and AES. This revealed that the inclusion of the saturated ethyl chain instead of two allyl fragment (removing bilateral symmetry present in chapter 4) led to the S-bridged compound displaying a more diverse conformational landscape, featuring a mixture of three distinct conformers compared to one in DAS. However, it remains true that the lighter congener (O-bridged) still exhibits a rich conformational landscape with more energetically similar conformers compared to the S-bridged compound. Interestingly, the presence of the saturated ethyl chain resulted in complex A/E splitting patterns due to the internal rotation of the methyl group in first two conformers of AEE. Experimentally derived structural parameters for conformer I of AEE and AES resulted in a smaller C-S-C angle than the C-O-C, along with larger p-orbital character on the sulfur bonding orbitals, which is consistent with the previous study. However, what adds an intriguing layer is the distinct variations in the orientations of the organic side chains between the AEE and AES conformers as none of the conformers exhibited any resemblance, compared to the similarities seen in conformer I of DAE and DAS. We found that this is due to the presence of unique non-covalent interactions involving the bridging chalcogen atoms (O *vs* S) with saturated and partially unsaturated side chains. For AEE, the LP donation to the allyl side chain governs the energy ordering, while it is the LP interaction with the ethyl fragment that determines the

conformer stability for AES. These findings once again underscore the substantial impact of the non-covalent forces involving the O or S atom in determining the arrangement of side chains as well as in governing conformational preferences of ethers and sulfides.

To further extend our understanding of the impact of various side chains on the conformational equilibria of chalcogen-containing molecules, Chapter 6 delved into the study of EVE, EVS, PVE, PVS, BVE, and BVS. Experimental analysis identified rotational transitions belonging to two conformers of PVE and four conformers of BVE. Also, a splitting pattern resembling that of AEE (chapter 5) was detected in the rotational spectrum of the initial two conformers of PVE and BVE and was attributed to methyl internal rotation. Structural parameters obtained from experimental measurements for the ground state geometry of PVE and BVE, along with the theoretically derived parameters of PVS and BVS, showed analogous behavior to what was observed in the previous chapters and in the theoretical calculations of EVS and EVE. This included the consistent observation of the C-S-C angle being smaller and having a greater p-orbital character than the C-O-C angle.

Interestingly, quantum chemical calculation showed that introducing the vinyl fragment and extending the saturated side chain produced a more diverse and competitive conformational equilibrium in S-bridged compounds compared to O-bridged ones. This observation is drastically different from those in previous chapters where ethers, not sulfides, exhibited rich conformational landscapes. The key factor driving this difference was the substantial steric repulsion within oxygen-containing molecules, restricting the free rotation of the side chains and destabilizing conformers. Also, moving from EVE and EVS to PVE and PVS to BVE and BVS led to a noticeable increase in the number of conformers due to the increase in the length of the saturated fragments. From theoretical calculations, we also learned the significance of the vinyl fragment

position in determining the energy ordering and highlighted the complex interplay of interactions involving the saturated side chain that result in competitive equilibria for the conformers of ether and sulfide compounds. These findings emphasize the intricate nature of the conformational landscape, dynamics, and geometries when employing various organic fragments in chalcogen bridged (O *vs* S) compounds.

In the last part of the thesis, we probed the impact of microsolvation on the conformational landscape of DAE and DAS monomers (Chapter 4) by examining their monohydrated complexes, DAE-w and DAS-w. The presence of a water molecule led to notable changes in the relative energies of DAE conformers, while the effect on DAS was comparatively less pronounced. However, the geometry of the lowest energy conformer does not change with the formation of a complex with water for both DAS and DAE. Theoretical calculations revealed that the most stable conformer I of DAE-w and DAS-w is stabilized by the presence of strong primary intermolecular OH···X (X= O, S) HB and secondary HBs between the oxygen of water and the allyl substituents. Also, we observed that sulfur exhibits weaker HB acceptor character compared to the oxygen compound allowing water molecule in DAS-w to undergo larger amplitude motions, with the barrier estimated to be ~4 kJ mol^{-1} smaller than that of DAE-w. As a result, tunneling splittings were detected in the spectrum of the sulfide complex, which were not resolvable in the spectrum of the ether complex. This study provides valuable insights into the effect of water binding as a function of the chalcogen atom substitution. In particular, the strength of the contacts formed during complexation significantly affects their conformational equilibria in unique ways and thus contributes to our understanding of solvation effects and internal dynamics in similar organic ether and sulfide molecules.

8.2 Future Outlook

There are several potential extensions to the work presented in this thesis, which include the following:

I. The expansion of these studies by varying organic side chains in chalcogen-bridged compounds offers an opportunity to uncover more trends in the conformational landscape of organochalcogens. For instance, building upon the results reported in this thesis, which have highlighted striking differences, competitiveness, and rich conformational equilibria, projects within the van Wijngaarden group have already commenced to investigate the impact of oxygen *vs* sulfur on various organic arrangements such as phenyl vinyl ether and phenyl vinyl sulfide compounds. As phenyl is an unsaturated compound akin to vinyl, it prompts questions about the applicability of our vinyl findings to phenyl, with its more extensive conjugated system. While the vinyl moiety could be orientated in down or side positions, its orientation formed a plane with the chalcogen. The difference in size between vinyl and phenyl introduces an intriguing element, particularly when considering spatial constraints. Furthermore, we can extend our insights to the propargyl side chain, investigating whether the results obtained from allyl compounds can carry forward to the case where there is now a triple bond, such as methyl propargyl ether and methyl propargyl sulfide, among many other possibilities.

II. The studies of monomers in Chapters 5 and 6 can be further extended to investigate their monohydrated complexes. The objective of such studies is to gain a deeper understanding of how the presence of a water molecule affects competitiveness of conformational equilibria as the binding of water can have a more pronounced impact when numerous conformers are closely spaced, potentially leading to unexpected energy orderings. The S-containing species with saturated side chains such as AES, PVS and BVS do have more energetically similar

geometries than in the case of DAS which would allow more detailed look at the differences between solvation of the O- and S-containing species. Also, the investigation of these compounds would delve into the internal dynamics when a methyl group is present. An intriguing avenue for exploration could also involve investigating other solvents that form weaker contacts with these molecules. This could lead to a comparison of how the binding behaviors of oxygen and sulfur compounds change in response to solvents with different interaction strengths. These analyses have the potential to elucidate general principles or trends pertaining to monosolvated complexes involving oxygen and sulfur compounds.

III. Another promising direction for expanding these studies is to investigate complexes featuring more than one water molecule. Exploring larger clusters provides an opportunity to discern how the presence of multiple solvent molecules impacts the systems' geometries. Moreover, understanding solvation effect at the molecular level within such clusters is essential for comprehending the chemical properties of condensed phases.[1] It would be useful to investigate how interactions with numerous solvent molecules govern their conformational preferences and the results might inspire theoreticians who develop solvation models to include better treatment of intermolecular effects in their models.

IV. The insights regarding conformational equilibria of ethers and sulfides could also be substantially improved by pursuing spectroscopic studies in higher electromagnetic frequency regions and in a static gas sample such as those used in microwave waveguides or in multipass gas cells in the millimeter or infrared regions. These experimental approaches would allow for more accurate determination of the characteristic spectral fingerprints by including transitions with higher quantum numbers that depend on higher-order centrifugal distortion constants and by populating higher energy forms. Such studies would also facilitate the

observation of transitions associated with vibrationally excited states which sample larger regions of the potential energy surfaces that govern the conformational equilibria.

The examples mentioned above serve as potential extensions of the research presented in this thesis, but it is essential to note that the possibilities for further research are not confined solely to these examples. The groundwork laid in this thesis lays a solid foundation for further advancements in our understanding, using high-level quantum calculations and rotational spectroscopy, to enhance models related to chemical bonding, reactivity and dynamics of organochalogens.

8.3 References

1 J. Tang, Y. Xu, A. R. W. McKellar and W. Jäger, Quantum solvation of carbonyl sulfide with helium atoms, *Science (80-.).*, 2002, **297**, 2030–2033.